A publication of
ECOLE NATIONALE POLYTECHNIQUE (ENP)

Engineering Science
Journal

ISSN: 2716-912X
E-ISSN: 2773-4293

DECEMBER 2025
VOLUME 5
NUMBER 2

Stochastic Analysis to Predict Reliability Index of a Tall Building Structure

Badreddine Chemali and Boualem Tiliouine

Abstract− This article presents a stochastic analysis to assess the probability of failure and reliability of tall building structures with random variables under stochastic seismic excitation, using the conventional Monte Carlo Simulation (MCS) method. Uncertainties in seismic loading, structural geometry, and material characteristics are incorporated t in the study. Furthermore, the sensitivity of structural reliability is examined in relation to different performance variable limit states. The numerical results demonstrate that structural reliability is significantly influenced by the variability of all random variables but more importantly by seismic loading randomness. It's shown that, when the variability of the random parameters is higher, the effects on structural reliability are more noticeable. In addition, preliminary sensitivity analysis based on the First Order Reliability Method (FORM) that gives information on the sensitivity of the randomness of the inputs parameters, shows that the 11 stochastic input parameters seismic probabilistic problem can be effectively reduced utilizing only 4 random variables, namely: the Peak Ground Acceleration, concrete elastic modulus, core inertia and reinforced concrete density.

***Keywords*− First Order Reliability Method, MCS, Peak Ground Acceleration, sensitivity, tall building structures.**

NOMENCLATURE

PGA	Peak Ground Acceleration
MCS	Monte Carlo Simulation.
FORM	First Order Reliability Method.
$\overline{\mathrm{X}}$	Mean value of random variable
P_f	Probability of failure
R	Reliability.
$g(\mathrm{X},\overline{\mathrm{X}})$	Performance function.
Φ	Cumulative Standard Normal Distribution Function.
β_{HL}	Hasofer-Lind Reliability index
A	sensitivity factor
RPA 2024	Algerian Earthquake Regulation
A	Zone acceleration coefficient
η	correction factor of damping
ξ	percentage of critical damping
$\bar{y}$	allowable maximum displacement
ρ	Density
I	Inertia
E	elastic modulus

I. INTRODUCTION

Uncertainties in the construction process may be categorized into two primary types: natural variability and human-induced factors (e.g. [1]). Natural uncertainties stem from unpredictable environmental loads (wind, seismic, snow, live loads) and material behavior variations, while human-induced uncertainties arise from design approximations, computational errors, etc.

The evolution of computational power has enabled the explicit incorporation of uncertainty quantification in structural analysis, facilitating deeper understanding of the behavior of probabilistic structures. (e.g. [2-5])

This study investigates the effectiveness of conventional Monte Carlo Simulation (MCS) in assessing structural performance and system reliability for high-rise buildings. Failure is defined as the exceedance of the building's lateral top displacement beyond code-specified limits (e.g., H/500 as per IBC design code [6]). Stochastic analyses are conducted on a representative high-rise buildings under seismic loading, with the following probabilistic modeling:

- Geometrical parameters as independent normal random variables
- Structural materials and loads modeled as lognormally distributed

The sensitivity of structural reliability to performance criteria is evaluated by varying the limit-state thresholds. Furthermore, the capabilities and limitations of the MCS approach are critically examined. In addition, preliminary sensitivity analysis based on FORM is conducted to identify critical input parameters, followed by interpretation of practical engineering consequences.

The paper is organized as follows: Reliability analysis methods are briefly described in Section 2. A description of Tall Building Structure Example is provided Section 3. The overall results of stochastic analyses to predict reliability index of a tall building structure with uncertain parameters under random seismic loading are presented in Section 4. Finally, the study concludes with a synthesis of key findings and their implications for structural reliability analysis.

II. SOME BACKGROUND ON RELIABILITY ANALYSIS METHODS

In the conventional probabilistic framework, the uncertainties are modeled as random parameters with certain distribution characteristics. Let denote X the vector of uncertain input parameters and $\overline{\mathbf{X}}=[\overline{X}_1,\ldots,\overline{X}_m]^T$ the vector of deterministic

Manuscript received October 3, 2023; revised February 22, 2024; revised July 7, 2025.

Badreddine Chemali and Boualem Tiliouine are with the Civil Engineering Department, Ecole Nationale Polytechnique, Algiers, ALGERIA (e-mail: badar093@yahoo.fr; boualem.tiliouine@g.enp.edu.dz).

Digital Object Identifier (DOI): 10.53907/enpesj.v5i2.244

input parameter (mean values of uncertain variables); the probability of failure Pf can be given as:

$$P_f = P\left[g(\mathbf{X},\overline{\mathbf{X}}) \le 0\right] = \int \dots \int_{g(\mathbf{X},\overline{\mathbf{X}})\le 0} p_{\overline{X}}(\mathbf{x},\overline{\mathbf{x}})d\overline{\mathbf{x}}_1 .. d\overline{\mathbf{x}}_m \qquad (1)$$

where $g(\mathbf{X},\overline{\mathbf{X}}) = \bar{y} - y(\mathbf{X},\overline{\mathbf{X}})$ is the limit state function and $g(\mathbf{X},\overline{\mathbf{X}}) \le 0$ expresses the failure event, hence the reliability can be defined as $g(\mathbf{X},\overline{\mathbf{X}}) > 0$; $\overline{\mathbf{x}} = [\overline{\mathbf{x}}_1,\dots,\overline{\mathbf{x}}_m]^T$ represents the realization of $\overline{\mathbf{X}}$, $\mathbf{p}_{\overline{\mathbf{x}}}(\mathbf{x},\overline{\mathbf{x}})$ represents the joint probability density function of the system parameters, typically estimated from empirical measurement data. The variable y denotes the performance metric, while $\bar{y}$ corresponds to its critical threshold (limit state).

For evaluating the probability of failure described in equation 1, various numerical methods are available for this purpose, including Monte Carlo Simulation (e.g. [3,7]), First- and Second-Order Reliability Methods (FORM/SORM) (e.g.[1]), Point Estimate Methods (e.g. [8]) and Response Surface Method (e.g. [9]).

A measure of the system reliability can be given by the Reliability Index

$$\beta = \Phi^{-1}(1 - P_f) \qquad (2)$$

where Φ^{-1} denotes the inverse standard normal cumulative distribution function. The reliability R is computed by:

$$R=\Phi(\beta) \qquad (3)$$

where Φ represents the standard normal cumulative distribution function

II.1 Monte Carlo Simulation technique

In stochastic assessment, the MCS method is habitually utilized when the analytical solution is not possible and the failure domain cannot be described by an analytical form. The Monte Carlo Simulation (MCS) method is particularly indispensable for complex problems involving numerous stochastic input parameters, where conventional reliability analysis techniques (e.g., FORM/SORM) prove inadequate. While MCS boasts a straightforward mathematical formulation and unparalleled versatility in handling problems of arbitrary complexity, its principal drawback lies in the prohibitive computational cost associated with traditional implementations—especially for high-dimensional or low-probability failure events. One basic advantage of the Monte Carlo Simulation over the other reliability analysis methods for the particular type of problems investigated in the present study is that its efficiency is not affected by the additional complexities due to non-linear analysis and the dynamic loads.

The computational cost of MCS grows proportionally when the number of input parameters is large or/and the magnitude of P_f is small, since both cases require a huge sample size. For this reason, various sampling techniques, also called variance reduction techniques, have been developed in order to improve the computational efficiency of the method in order to minimize the sample size and minimize the statistical inaccuracy that is intrinsic to MCS approaches.

Expressing the limit state function as $g(\mathbf{X},\overline{\mathbf{X}}) \le 0$, where $\overline{\mathbf{X}} = [\overline{X}_1,\dots,\overline{X}_m]^T$ is the vector of the random variables and since MCS is based on the theory of large numbers (N∞), an unbiased estimator of the probability of failure is given by

$$P_f = \frac{1}{N_\infty}\sum_{j=1}^{N_\infty} I(\mathbf{x}_j) \qquad (4)$$

in which, $I(x_j)$ is an indicator for successful and unsuccessful simulations defined as

$$I(\mathbf{x}_j) = \begin{cases} 1 \quad \text{if} \quad g(\mathbf{X},\overline{\mathbf{X}}) \ge 0 \\ 0 \quad \text{if} \quad g(\mathbf{X},\overline{\mathbf{X}}) < 0 \end{cases} \qquad (5)$$

To estimate the failure probability P_f, the Monte Carlo method generates N independent random realizations of the input vector **x**, typically sampled from a uniform probability distribution. For each realization x_j, the limit-state function $g(\mathbf{x}_j)$ is evaluated. The failure probability is then estimated as:

$$P_f = \frac{n}{N} \qquad (6)$$

where N represents the total number of Monte Carlo trials and n denotes the count of simulations where the response exceeds the deterministic case (evaluated at mean input values). Traditional MCS is that in order to acquire an accurate prediction of output first and second moments, the analysis may require thousands of simulation runs, resulting in computationally intensive and resource-demanding calculations.

To enhance computational efficiency while preserving the accuracy of Monte Carlo Simulation, several variance reduction techniques have been developed (e.g. [1, 5, 10-11]).

III. DESCRIPTION OF TALL BUILDING STRUCTURE EXAMPLE

The case study examines a 35-story wall-frame structure (height: 122.5 m) as shown in Figure 1 [12]. The lateral load-resisting system for seismic actions along the long facade consists of:

- Six moment-resisting frames
- A central core ($I = 313$ m^4)

With a concrete elastic modulus (E) of 2×10^7 kN/m^2, this analysis aims to quantify the structural reliability under seismic loading conditions compatible with the design spectra derived from Algerian Earthquake Regulations [13] based on five parameters: soil types S1 (rocky site), category 1A with an Importance coefficient I =1.2. The structure is assumed to be located in a moderate seismicity zone (zone II a) characterized by an acceleration coefficient A = 0.25g (see Fig. 2). Table I presents the moment of inertia values for frame columns and girders, along with their statistical distributions, for the 35-story case study building.

The seismic action is represented by the following Design Response Spectrum as per the Algerian Earthquake Regulations (RPA2024)

A: Zone acceleration coefficient
η: damping correction factor

$$\eta = \sqrt{\frac{7}{2+\xi}} \quad \text{(used when } \xi \text{ is not equal to 5\%)}$$

ξ: damping ratio

I: Importance coefficient

T1, T2: characteristic site periods corresponding to the designated soil category

S: Site coefficient

$$\frac{S_a}{g} = \begin{cases} A.I.S\left(1+\frac{T}{T_1}(2.5\eta-1)\right)\ldots\ldots\ldots\ldots\ldots\ldots 0 \le T \le T_1 \\ A.I.S(2.5\eta)\ldots\ldots\ldots\ldots\ldots\ldots\ldots\ldots\ldots\ldots\ldots T \le T \le T_2 \\ A.I.S(2.5\eta)\left(\frac{T_2}{T}\right)\ldots\ldots\ldots\ldots\ldots\ldots\ldots\ldots T_2 \le T \le T_3 \\ A.I.S(2.5\eta)\left(\frac{T_2 T_3}{T^2}\right)\ldots\ldots\ldots\ldots\ldots\ldots T_3 \le T \le 4s \end{cases} \qquad (7)$$

The top displacement is selected as the governing parameter for the performance function evaluation.

As quantified in Table I, the stochastic input variables comprise:

- Geometric parameters (e.g., member dimensions),
- Material properties (e.g., concrete strength), and
- Seismic loading, characterized through Peak Ground Acceleration (PGA) variability

It should be noted that there is Additional stochastic parameters significantly influence structural reliability assessments, particularly live load uncertainties (e.g. [14]), spatially correlated soil variations (e.g. [15]), and soil-structure interaction complexities (e.g. [16]) etc...For the sake of clarity we will focus on the variables mentioned above.
The corresponding limit state function takes the form:

$$g(I_{ci}, I_{bi}, \ldots, PGA) = \bar{y} - y(\mathbf{z} = \mathbf{H}) \qquad (8)$$

The limit state compares the allowable top displacement ($\bar{y}$) against the response spectrum-derived demand. A parametric reliability analysis was conducted by progressively increasing $\bar{y}$ and computing the failure probability via MCS at each step. The study employed 80,000 stochastic samples of PGA and first-mode frequency, with their distributions shown in Figures 3–4.

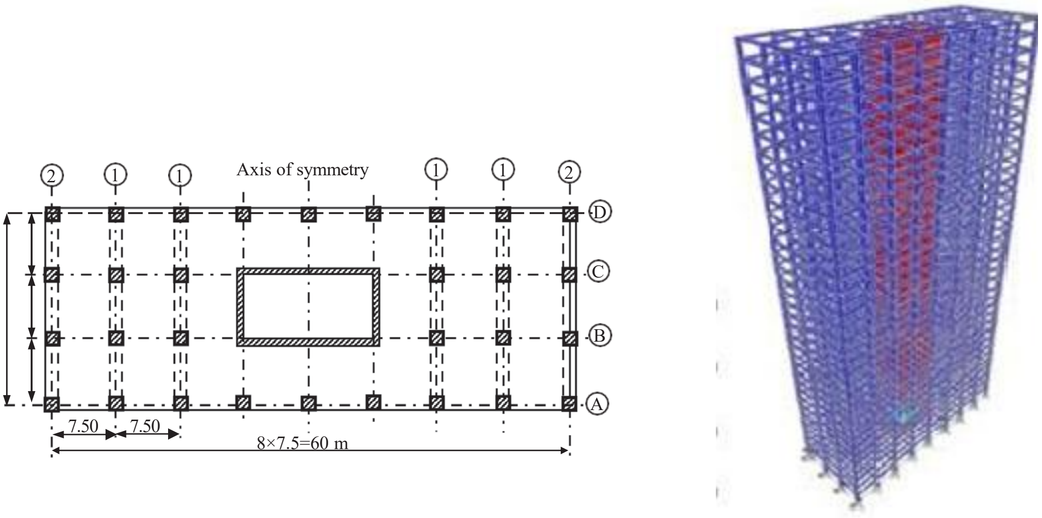

(a) (b)

Fig. 1. Plan (a) and 3-D view (b) of 35-story wall-frame

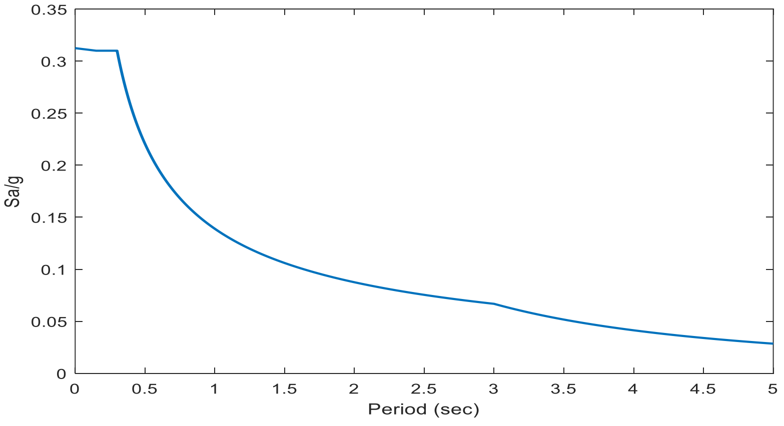

Fig. 2. Elastic design response spectrum

TABLE I
STRUCTURAL PARAMETERS AND STATISTICAL DATA FOR 35-STORY HIGH-RISE BUILDING

Parameters	**Stochastic variable**	**Symbol**	**Mean**	**Coefficient of variation**	**Distribution**
geometrical	Core	I_{cor}	313 m^4	0.05	Normal
	Frame 1	I_{ic1}	0.083 m^4		
		I_{ec1}	0.050 m^4		
		I_{g1}	0.011 m^4		
	Frame 2	I_{ic2}	0.050 m^4		
		I_{ec2}	0.034 m^4		
		I_{g2}	0.005 m^4		
material	Elastic modulus	E	2 x 10^7 KN/m^2	0.15	Lognormal
	Damping Ratio	ξ	7%	0.25	
	Density	P	2500 Kg/m^3	0.20	
Loading	Peak Ground Acceleration	PGA	0.25g	0.30	Lognormal

Where i: Interior, E: exterior, c: column and g: girder.

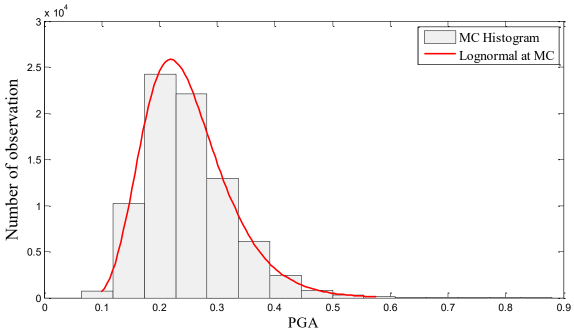

Fig. 3. Histogram for PGA generated with MCS technique.

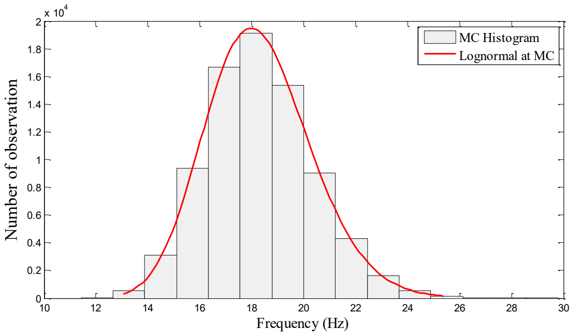

Fig. 4. Histogram for frequency of first vibration mode of 35 story building, generated with MCS

IV. RESULTS AND DISCUSSION

A comprehensive evaluation of the proposed structural reliability methodology's practical utility and performance characteristics is presented in this section. The case study structure enables an efficient numerical solution through modal superposition techniques (e.g. [17]), significantly enhancing the computational feasibility of Monte Carlo Simulation (MCS) implementation.

Through combined seismic response spectrum analysis and conventional Monte Carlo Simulation (MCS), the structural reliability assessment yields:

- Probability of failure (P_f) = 4.94 × 10^{-2} (95.06% reliability)
- Reliability index (β) = 1.651

These MCS-derived results are comprehensively summarized in Table II.

TABLE II.

RELIABILITY RESULTS of Tall Building Structures MCS

y **(mm)**	P_f	R (%)	**βMCS**
10	100	0,000	-8,112
50	99,931	0,069	-3,200
125	65,654	34,346	-0,403
143	49,698	50,302	0,008
145	48,008	51,992	0,050
175	26,634	73,366	0,624
245 (H/500)	4,938	95,062	**1,651**
300	1,163	98,837	2,269
350	0,308	99,692	2,739
400	0,082	99,918	3,147

For all the points $\sigma_y = 51.8\,mm$

The probability distributions of both seismic intensity (PGA) and structural reliability (performance variable CDF) are shown in Figures 5 and 6 respectively, with their theoretical PDF fits. These results were obtained through extensive Monte Carlo simulation (N = 80,000 realizations).

Figure 7 presents the computed failure probabilities for the case study structure as a function of the seismic load Coefficient of Variation (COV). The probabilities correspond to exceedance of the specified limit state for top displacement (the selected performance variable). The results demonstrate a clear positive correlation between failure probability and increasing seismic load variability.

The First-Order Reliability Method (FORM) offers an additional valuable feature through its directional cosines [1], which quantify the sensitivity of the reliability index to each random input variable. This sensitivity information is particularly important for robust design optimization. A preliminary FORM-based sensitivity analysis was performed, revealing that variables with sensitivity measures below a specified threshold α (Equation 9) could be treated as deterministic. For this case study, α was set at 3%, allowing identification of parameters with negligible influence on the structural reliability. It should be mentioned that although the First-Order Reliability Method (FORM) offers directional cosines for sensitivity ranking, other reliable methods, like the response surface method (e.g. [18]) or incomplete Monte Carlo simulation (e.g. [19]), provide complementary benefits for sensitivity analysis using reliability index.

$$\alpha_i = \frac{\left(\frac{\partial g}{\partial x'_i}\right)^{*} \sigma_{x'_i}}{\sqrt{\sum_{i=1}^{n}\left(\frac{\partial g}{\partial x'_i}\sigma_{x'_i}\right)^{2*}}} \qquad (9)$$

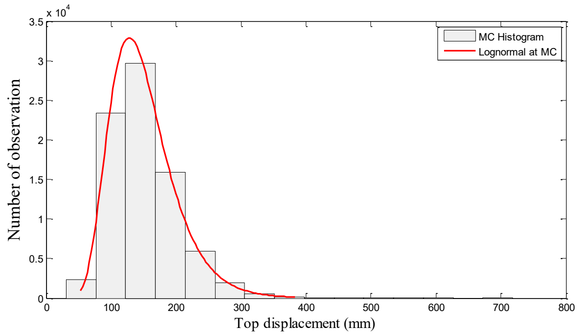

Fig. 5. Histograms for top displacement generated with MCS

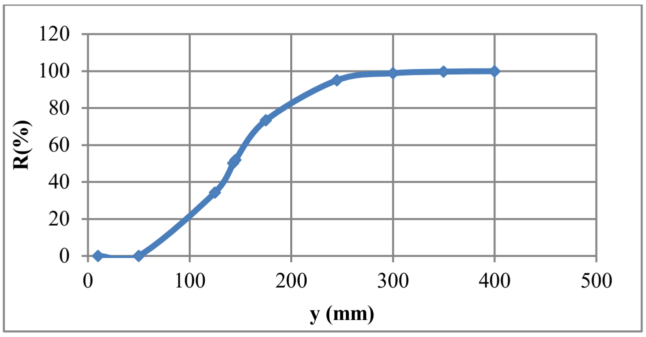

Fig. 6. Reliability of study tall building structure calculated by MCS

The reliability analysis was thus simplified from an 11-dimensional random variable problem to a 4-variable formulation, retaining only the most influential parameters:

1. Peak Ground Acceleration (PGA, α = 0.861)
2. Concrete elastic modulus (E, α = 0.291)
3. Core moment of inertia (I, α = 0.095)
4. Reinforced concrete density (ρ, α = 0.379)

Figure 8 demonstrates the characteristic convergence behavior of the failure probability estimate as sample size increases. While Monte Carlo Simulation (MCS) with N realizations provides robust reliability estimates, its computational demand becomes significant for systems with numerous degrees of freedom (DOFs). For this case study, the analysis employed $8\mathrm{x}10^4$ simulations, determined through progressive assessment of failure probability convergence versus sample size. More complex scenarios may require substantially larger sample sizes due to slower statistical convergence. In the current implementation (11 random input variables and one output performance function), the MCS required 9 minutes and 23 seconds of CPU time for $8\ \mathrm{x}10^4$ samples.

V. CONCLUSIONS

The design of tall building structures is inherently influenced by multiple uncertainty sources. However, through systematic reliability-based approaches, structural safety can be enhanced to meet or exceed codified reliability thresholds.

The analysis demonstrates that structural reliability is sensitive to variability in all uncertain parameters, with particularly strong dependence on loading randomness, density of concrete, core inertia and concrete elastic modulus uncertainty. Furthermore, the effects on structural reliability have been shown to be more pronounced for higher variability of the stochastic variables.

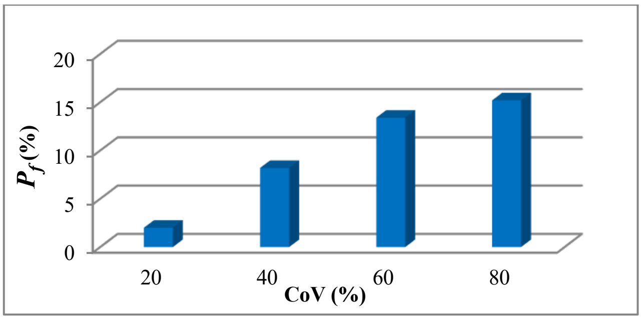

Fig. 7 Structural Failure Probability as Function of Seismic Load COV

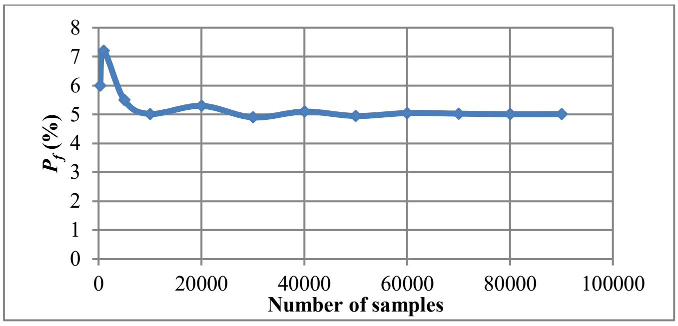

Figure 8 Convergence of probability of failure with increasing sample size

Monte Carlo Simulation (MCS) for stochastic analysis of tall buildings often requires substantial computational resources, particularly for structures with numerous degrees of freedom and multiple random variables. Implementing variance reduction techniques combined with sensitivity analysis via directional cosines can significantly improve computational efficiency while maintaining accuracy - a crucial consideration for robust design applications.

REFERENCES

[1] Farsangi, E. N., Noori, M., Gardoni, P., Takewaki, I., Varum, H., & Bogdanovic, A. (Eds.). “Reliability-based analysis and design of structures and infrastructure”. CRC Press. 2021.

[2] Y. Tsompanakis, V. Papadopoulos, N. D. Lagaros and M. Papadrakakis, “Reliability analysis of structures under seismic loading”. Fifth World Congress on Computational Mechanics. Vienna, Austria, July 7-12, 2002

[3] B. Chemali and B. Tiliouine,. “Uncertainty propagation in dynamics of structures with correlated damping using a nonlinear statistical model” Int. J. Struct. Eng , 7 (2), pp 145 – 159. 2016. https://doi.org/10.1504/IJSTRUCTE.2016.076692

[4] Aldosary, M., Wang, J., & Li, C. . “Structural reliability and stochastic finite element methods: State-of-the-art review and evidence-based comparison”. Engineering Computations, 35(6), 2165-2214. 2018 https://doi.org/10.1108/EC-04-2018-0157

[5] Teng, D., Feng, Y. W., Chen, J. Y., & Lu, C. “Structural dynamic reliability analysis: review and prospects. International Journal of Structural Integrity”, 13(5), 753-783. 2022 https://doi.org/10.1108/IJSI-04-2022-0050

[6] International Code Council, International Building Code. Whittier, California, USA. 2009

[7] M.H. Kalos and P.A. Whitlock, “Monte Carlo Methods”, 2nd ed New York: Wiley. 2002

[8] E. Rosenblueth, “Point estimates for probability moments”. Proc., Nat. Acad. of Sci., vol. 72 no. 10, pp. 3812–3814 , 1975. https://doi.org/10.1073/pnas.72.10.3812

[9] Chemali, B., & Tilioune, B. (2023). Probabilistic analysis of shallow foundations on c-φ soils using 2nd order response surface methods. Periodica Polytechnica Civil Engineering, 67(2), 485-494. https://doi.org/10.3311/PPci.17917

[10] Pulido, T.L. Jacobs, E.C. Prates De Lima, “Structural reliability using Monte-Carlo simulation with variance reduction techniques on elastic-plastic structures”, Comp. & Struct. vol. 43, pp. 419-430. 1992. https://doi.org/10.1016/0045-7949(92)90275-5

[11] Y. Cao, M.Y. Hussaini, and T.A. Zang, “Exploitation of sensitivity derivatives for improving sampling methods” , AIAA Journal. vol. 42, no. 4, pp. 815-822, 2004. https://doi.org/10.2514/1.2820

[12] Y Ohtori, RE Christenson, BF Spencer Jr, SJ Dyke, Benchmark Control Problems for Seismically Excited Nonlinear Buildings, J. Eng. Mech. 130, 366 (2004)

[13] Ministère de l’Habitat, Document Technique Réglementaire DTR B C 2 48, Règles Parasismiques Algériennes RPA 2024 Centre National de Recherche Appliquée en Génie-Parasismique, 2024.

[14] Costa, L. G., & Beck, A. T. (2024). A critical review of probabilistic live load models for buildings: Models, surveys, Eurocode statistics and reliability-based calibration. Structural Safety, 106. 2024.
https://doi.org/10.1016/j.strusafe.2023.102411

[15] Luo, Z., Kim, M., & Hwang, S. (2021). Effect of soil spatial variability on the structural reliability of a statically indeterminate frame. ASCE-ASME Journal of Risk and Uncertainty in Engineering Systems, Part A: Civil Engineering, 7(1), 04020048.2021
https://doi.org/10.1061/AJRUA6.0001098

[16] Bezih, K., Chateauneuf, A., Kalla, M., & Bacconnet, C. Effect of soil–structure interaction on the reliability of reinforced concrete bridges. Ain Shams Engineering Journal, 6(3), 755-766. 2015.
https://doi.org/10.1016/j.asej.2015.01.007

[17] Chopra, A. K. “Dynamics of structures”. 4th ed. Pearson, USA. 2022.

[18] Zhou, C., Li, C., Zhang, H., Zhao, H., & Zhou, C. (2021). Reliability and sensitivity analysis of composite structures by an adaptive Kriging based approach. Composite Structures, 278, 114682.
https://doi.org/10.1016/j.compstruct.2021.114682

[19] Tandjiria, V., Teh, C. I., & Low, B. K. (2000). Reliability analysis of laterally loaded piles using response surface methods. Structural safety, 22(4), 335-355.
https://doi.org/10.1016/S0167-4730(00)00019-9

Badreddine Chemali received his Msc (Magister) and Ph.D. in Civil Engineering from École Nationale Polytechnique (ENP), Algiers in 2024. He holds membership in the Earthquake Engineering and Structural Dynamics Laboratory (LGSD) within ENP's Civil Engineering Department. Currently, Dr. Chemali serves as a Reservoir Engineering Specialist in the Production Division of SONATRACH, Algeria's national oil and Gas Company.

Boualem Tiliouine received his Msc and PhD degrees in Civil Engineering from Stanford U., USA and is a former Research Fellow at the Blume’s Earthquake Engineering Center of Stanford University. He is currently working as a full time Professor at the “Ecole Nationale Polytechnique” (ENP), Algiers. He has published over 120 papers in reputed international journals and conferences. He has been chief investigator of several nationally and internationally funded research projects and has over 30 years of experience in teaching, research and consultancy. His previous positions and work experience include General Director of ENP, Structural Engineering Expert and Technical Adviser at CE Department of Dubai Municipality. His research interests include earthquake engineering, structural dynamics, soil structure interaction and optimization. He is Honorary Fellow of the National Academic Committee of the Ministry of Higher Education and Scientific Research (Algeria) and active member of the French Association of Earthquake Engineering.

Fractional-order PD control of a parallel Delta robot: Experimental results

Someya Amrane, Chems Eddine Boudjedir and Djamel Boukhetala

Abstract− In this paper, a fractional-order proportional–derivative (PD) controller is proposed as a means to enhance the trajectory tracking performance of a parallel Delta robot. The highly coupled and nonlinear dynamics of the Delta robot pose significant challenges for conventional integer-order PD controllers, often resulting in limited tracking accuracy. To address these limitations, the integer-order derivative term is replaced by a fractional-order derivative, thereby providing additional tuning flexibility and improved dynamic behavior. In experimental studies, a comparison is conducted between the fractional-order and integer-order PD approaches, as well as an evaluation of the influence that different fractional derivative orders have on robot tracking performance.

***Keywords*− Fractional-order, PD controller, Trajectory tracking, Delta robot.**

I. INTRODUCTION

Many theoretical contributions to fractional calculus have been proposed by Euler, Liouville, Riemann, and Grünwald [1]. These definitions have been successfully applied in multiple domains, such as electromagnetism and electrochemistry. For a historical introduction to fractional calculus, the reader can refer to [2].

The application of fractional calculus has experienced significant growth over the last decades, due to its robustness and improved tracking performance. Fractional calculus has been applied in many engineering fields, such as robotics [3], autonomous underwater vehicles [4], and wind turbine generators [5].

Parallel kinematic robots offer several advantages over serial robots, such as high rigidity, accuracy, and load capacity. Professor Raymond Clavel invented the parallel Delta robot as an efficient solution for repetitive pick-and-place operations. The original prototype features three translational degrees of freedom and one rotational degree of freedom [6]. The reader may refer to the survey [7] for further designs of the Delta robot.

The robot manipulator is commonly controlled using conventional PID controllers [8]. However, this control law is often inadequate for applications requiring high precision under fast dynamic motions, due to the fact that the PD control parameters are chosen without fully considering the coupling effects. To overcome this issue and improve trajectory tracking performance, many works have been proposed, such as nonlinear PD control [9], iterative learning control [10-12], time delay control [13], and sliding mode control [14].

In recent years, both fractional calculus and model-free control strategies have attracted considerable attention. Several control frameworks have incorporated fractional-order operators into the control loop, for instance, fractional adaptive control [15] and robust control design CRONE [16].

Fractional-order PID controllers have demonstrated superior robustness and performance compared to conventional PID controllers. Podlubny's proposal introduced a generalized fractional-order PID controller of the form $PI^{\lambda}D^{\mu}$, where λ and μ are non-integer orders. By appropriately tuning these parameters, the tracking accuracy can be significantly improved [1].

Fractional-order PID controllers have been further investigated in [17], where the robustness and performance were enhanced. In [18], the fractional-order PID controller was applied to a planar parallel robot to improve trajectory tracking accuracy. In [19], a fractional-order PID was designed to control a parallel robot, resulting in reduced tracking error and eliminated overshoot.

The main contribution of this paper is the design and experimental implementation of a fractional-order PD controller for trajectory tracking of a parallel Delta robot. Experimental studies are conducted to evaluate the effectiveness of the proposed approach. A comparative analysis between the fractional-order PD controller and the conventional integer-order PD controller is also conducted.

The remaining sections of this paper are organized as follows: section II introduces the dynamic model of the Delta robot. Section III presents the controller design. While in section IV, experimental results are presented. Finally, section V provides some conclusions.

II. DYNAMIC MODEL

The Delta robot shown in Fig. 1 is equipped with three kinematic chains, each consisting of a servo motor and a reducer connected to the upper arm. The forearm of the Delta robot is linked to both the upper arm and the travelling plate.

Manuscript received November 11, 2025; revised January 2, 2026.

S.Amrane and D.Boukhetala are affiliated with the laboratory of process control, Ecole nationale Polytechnique, Algiers, Algeria (someya.amrane@g.enp.edu.dz; djamel.boukhetala@g.enp.edu.dz)

C.Boudjedir is affiliated with LRPE laboratory, University of science and technology Houari Boumediene, Algiers, ALGERIA (chemseddine.boudjedir@usthb.edu.dz)

Digital Object Identifier (DOI): 10.53907/enpesj.v5i2.350

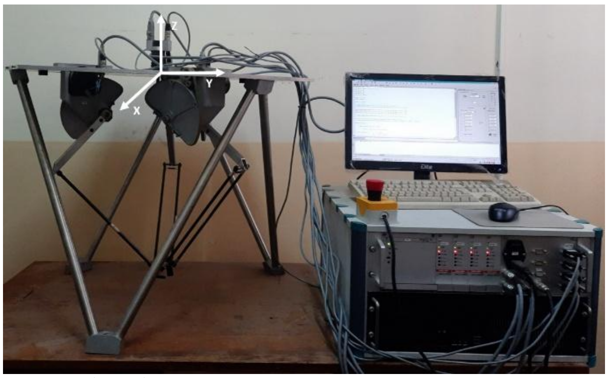

Fig. 1: Delta Robot

The robot dynamics is described as in [11]:

$$M(q)\ddot{q} + C(q,\dot{q})\dot{q} + G(q) = \tau \qquad (1)$$

Where:

$$M(q) = I_b + m_{nt}J^TJ$$
$$C(q,\dot{q}) = J^Tm_{nt}\dot{J}$$
$$G(q) = -\tau_{G_n} - \tau_{G_b}$$

The generalized joint vector is denoted as $q = [q_1, q_2, q_3]^T$, the inertia matrix is represented by M(q) $\in R^{3\times3}$, the vector resulting from centrifugal and Coriolis forces is denoted as $C(q,\dot{q})\dot{q} \in R^{3\times3}$. $G(q) \in R^{3\times1}$ refers to the gravitational vector. τ, τ_{G_b} and τ_{G_n}represent, respectively, the joint torque, the torque produced by the gravitational force of the arms and the torque produced by the inertial force. The Jacobian matrix is denoted as J, and its derivative respect to time is given as $\dot{J}$.
m_{nt} signifies the total mass, which includes the mass of the travelling plate, the playload mass and the combined masses of the three forearms.

The expression of the torques is given as follows:

$$\tau_{G_n} = J^Tm_{nt}[0 \quad 0 - g]^T \qquad (3)$$
$$\tau_{G_b} = m_br_{G_b}g[\cos q1 \quad \cos q2 \quad \cos q3]^T \qquad (4)$$

The detailed expressions of J, $\dot{J}$, m_{nt} and $r_{G_b}$are given in [11]. Table I describes the parameters of the robot.

Table. I
GEOMETRIC AND DYNAMIC PARAMETERS

Parameters	DESCRIPTION	Value
$\mathbf{L_a}$	Upper arm length	0.380 m
$\mathbf{L_b}$	Forearm length	0.205 m
$\boldsymbol{m}_{\mathbf{n}}$	Traveling plate mass	0.42 kg
$\mathbf{m_{br}}$	Upper arm mass	0.098 Kg
$\mathbf{m_{ab}}$	Forearms masses	0.028 Kg
$\mathbf{m_c}$	Elbow mass	0.016 Kg

III. CONTROLLER DESIGN

The PD controller is proposed in joint space as follows:

$$\tau = k_{p0}\tilde{q}(t) + k_{d0}\dot{\tilde{q}}(t) \qquad (5)$$

In which, k_{p0} and k_{d0} are constant diagonal matrices. $q(t)$ and $\dot{q}(t)$ are given as follows:

$$\tilde{q}(t) = q_d(t) - q_k(t)$$
$$\dot{\tilde{q}}(t) = \dot{q_d}(t) - \dot{q_k}(t)$$

Where $q_d(t)$ and $\dot{q_d}(t)$ represent the desired joint position and the desired joint velocity, respectively. The actual joint position and the actual joint velocity are denoted as $q_k(t)$ and $\dot{q_k}(t)$ respectively.

Since conventional PID controllers may not achieve satisfactory performance for tasks requiring high precision, many studies have applied fractional-order PID controllers to improve accuracy and trajectory tracking. In this paper, a fractional-order PD controller is implemented on the Delta robot. The control law includes three parameters: the proportional gain K_p, the derivative gain K_d, and the derivative fractional-order μ.

By introducing the fractional derivative order, the controller can achieve a satisfactory trade-off among the advantages and drawbacks of the conventional PD controller, such as enhanced stability provided by the derivative term, while mitigating its main disadvantage, i.e., high sensitivity to noise.

The continuous differential operator is given by :

$$_{a}D_t^{\mu} = \frac{d^{\mu}}{dt^{\mu}} \qquad \mu > 0$$

Where, $\mu \in R$ is the operation order.

Grunwald-Letnikov definition is given by :

$$_{a}D_t^{\mu}f(t) = \frac{_{a}d_t^{\mu}f(t)}{dt^{\mu}} = \lim_{h\to0}\left\{\frac{1}{h^{\mu}}\sum_{k=0}^{\frac{t-a}{h}}(-1)^k\binom{\mu}{k}f(t-kh)\right\}$$

The fractional-order derivative of the function f requires knowledge of $f(t)$ over the interval [a, t], in contrast to the integer order which only requires knowledge of f near t. This feature leads to the conclusion that fractional-order systems are long-memory systems.

The fractional-order PD controller is expressed as:

$$\tau = k_p\tilde{q}(t) + k_dD^{\mu}\tilde{q}(t) \qquad (8)$$

where the torque τ represents the control signal.

Fractional-order functions must approximated by integer-order expressions to be easily handled during software implementation. The numerical approximation for fractional calculus used in this paper is the Grünwald–Letnikov method, based on the Taylor expansion [1] :

$$_{\left(k-\frac{L}{h}\right)}D_{t_k}^{\mu}\ \tilde{q}(t) \approx h^{-\mu}\sum_{j=0}^{k}(-1)^j\binom{\mu}{j}\tilde{q}(t_{k-j})$$
$$= h^{-\mu}\sum_{j=0}^{k}c_j^{(\mu)}\ \tilde{q}(t_{k-j}) \qquad (9)$$

In which, $t_k = kh$, h is the sampling period, and L represents the memory length,

The binomial coefficients can be calculated as follows:

$$c_j^{(\mu)} = \left(1 - \frac{1+\mu}{j}\right)c_{j-1}^{(\mu)} \qquad (10)$$

and $c_0^{(\mu)} = 1$

The scheme of the fractional-order PD controller is shown in Fig. 2, where IGM illustrates the inverse geometric model and x_d denotes the desired trajectory in the operational space.

Remark 1*:* The fractional-order PD controller can be widely used in industrial applications due to its ease of implementation.
Remark 2: Unlike the control strategies which require an exact mathematical model, the fractional-order PD controller is model-free.

Remark 3: The parameters of the fractional-order PD controller allow achieving a better trade-off between the positive and negative effects of the derivative action.

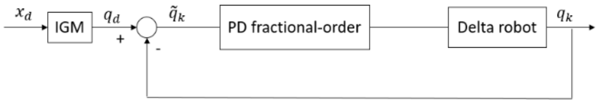

Fig. 2: Scheme of the proposed controller.

IV. Experimental Results

The experimental results obtained by applying the fractional-order PD control law (8) on the Delta robot of Fig. 1 are presented in this section.

The robot utilizes brushed DC motors with a belt-driven transmission having a ratio of r=12. The operational trajectory is executed with a maximum acceleration of 15 m/s^2 [23, 24]. The data were collected by sampling at 1 kHz, and the control algorithms were implemented in C language.

The tracking performance evaluation involves the utilization of the Maximum Absolute Error (MAE) and Root Mean Square Error (RMSE) as criteria. The expressions of these criteria are as follows:

$$RMSE_x = \sqrt{\frac{1}{n}\sum_{i=1}^{n}(x_i - x_{d_i})^2} \tag{11}$$

$$MAE_x = \max\left(|x_i - x_{d_i}|\right) \tag{12}$$

Where n represents the number of samples, x_d represents the desired trajectory in the operational space and x_i is the actual response in operational space.

The expression of the RMSE and MAE when considering all the three axes is given by:

$$RMSE = \sqrt{RMSE_x^2 + RMSE_y^2 + RMSE_z^2} \tag{13}$$

$$MAE = \max\left(MAE_x, MAE_y, MAE_z\right) \tag{14}$$

The controller gains and fractional-order are selected as $k_p = diag\{2.2, 2.2, 2.2\}$, $k_d = diag\{0.0145, 0.0145, 0.0145\}$ and $\mu = 1.12$. These parameters are obtained using an iterative tuning procedure, in which tracking performance is evaluated by varying one parameter at a time while holding the others constant. The parameter k_p is maintained at a moderate level to highlight the impact of the order μ. Increasing k_p results in a faster response; however, it may also amplify overshoot, particularly when combined with a high μ.

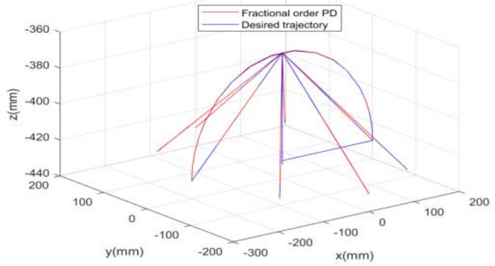

Fig. 3: The operational trajectory tracking under the fractional-order PD controller

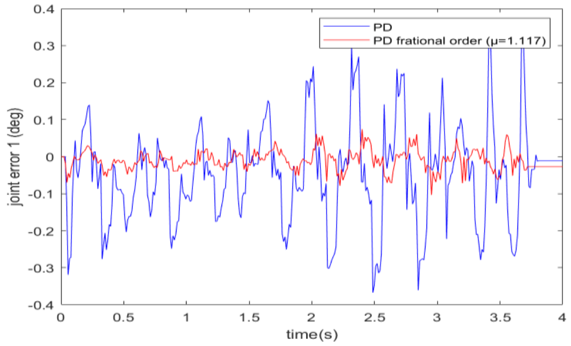

Fig. 4: Experimental tracking error of joint 1.

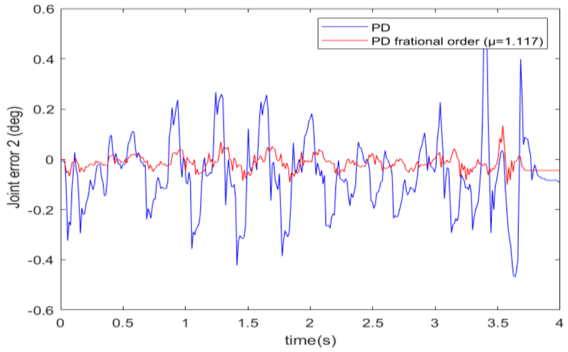

Fig. 5: Experimental tracking error of joint 2.

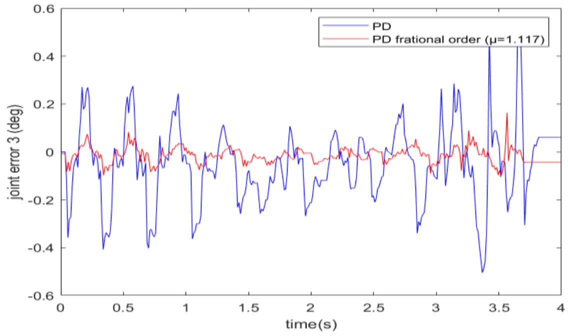

Fig. 6: Experimental tracking error of joint 3.

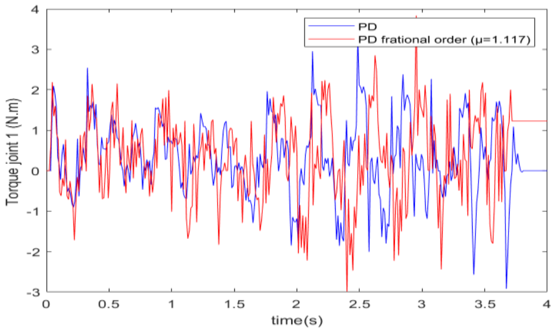

Fig. 7: Control torque of joint 1.

Fig 3 illustrates the trajectory tracking in the operational space under the proposed fractional-order PD controller. Figures 4, 5, and 6 depict the tracking error under the proposed fractional-order PD and PD controller of joints 1, 2, and 3, respectively. The figures point out that the tracking error under the fractional-order PD is inferior compared to the error under the PD controller. The proposed controller exhibits an RMS error equal to 0.17 mm, which is less than 80.4% of that provided by the PD controller. For MAE, the fractional PD controller can ensure 0.49 mm, which is less than 80.8% of that ensured by the PD controller.

Figures 7, 8, and 9 show the control torque signals under the PD and fractional-order PD controller for joints 1, 2, and 3, respectively. It is observed that the torque signals have nearly the same amplitude and variation. Table II presents the tracking performance of both controllers.

Figs. 10 to 15 represent the tracking errors and control torque signals under the fractional-order PD controller for different derivative fractional-orders of joints 1, 2, and 3, respectively. It can be observed that when $\mu=0.91$, the tracking error is much larger compared to the cases when $\mu=1.11$ or $\mu=1.21$. The RMSE decreases from 0.43 mm at $\mu=0.91$ to 0.17 mm at $\mu=1.11$, and to 0.11 mm for $\mu=1.21$.

Nevertheless, increasing the value of the fractional order μ leads to significant oscillations in the control signals, which may degrade the tracking performance of the proposed controller.

Table III outlines the RMSE and MAE of the fractional-order PD controller under different fraction orders.

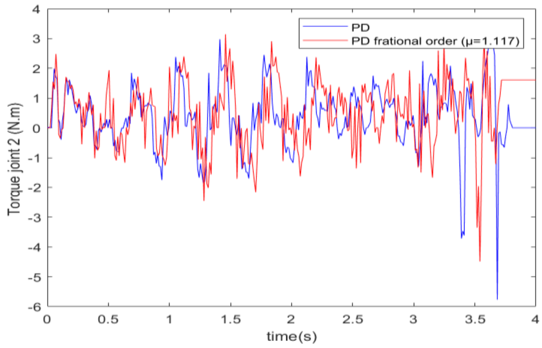

Fig. 8: Control torque of joint 2.

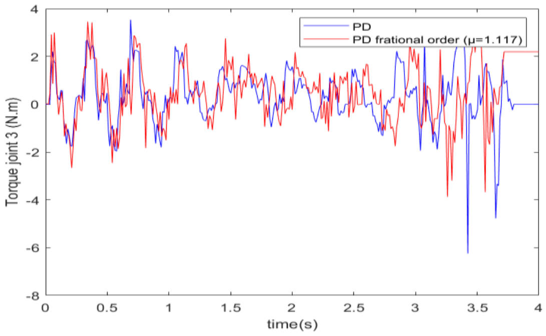

Fig. 9: Control torque of joint 3.

Table. II
TRACKING PERFORMANCE

Performance	PD	Fractional-order PD
RMSE (mm)	0.87	0.17
MAE (mm)	2.56	0.49

Table. III
TRACKING PERFORMANCE FOR DIFFERENT FRACTIONAL ORDERS

Performance	$\mu = 1.21$	$\mu = 0.91$	$\mu = 1.11$
RMSE (mm)	0.11	0.87	0.17
MAE (mm)	0.44	2.56	0.49

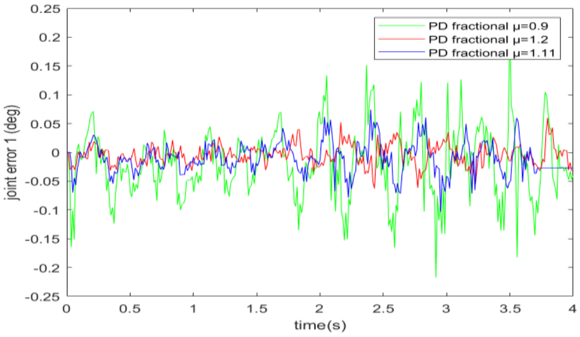

Fig. 10: Tracking error for different fractional derivative order of joint 1.

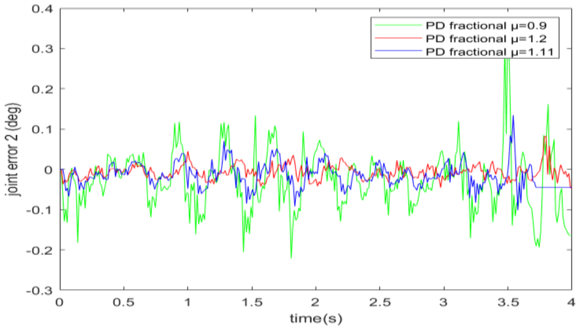

Fig. 11: Tracking error for different fractional derivative order of joint 2.

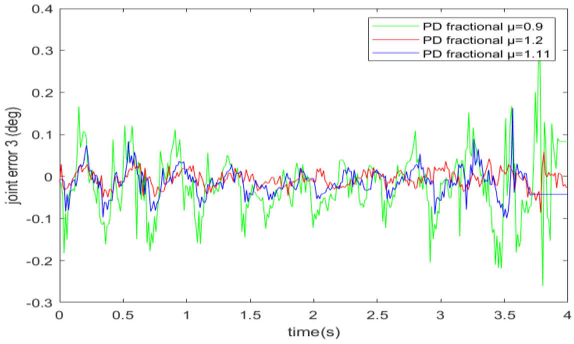

Fig. 12: Tracking error for different fractional derivative order of joint 3.

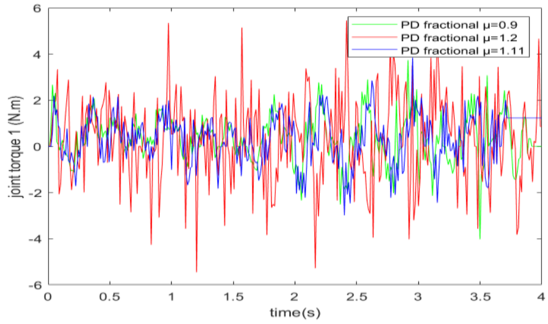

Fig. 13: Control torque for different fractional derivative order of joint 1.

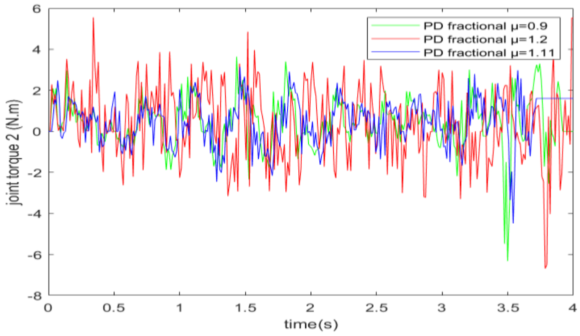

Fig. 14: Control torque for different fractional derivative order of joint 2.

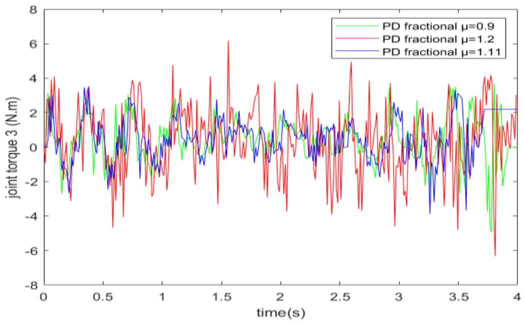

Fig. 15: Control torque for different fractional derivative order of joint 3.

V. CONCLUSION

In this paper, a model-free fractional-order PD controller is applied to a Delta robot to address the trajectory tracking problem. To improve the performance of the conventional PD controller, a fractional derivative order is introduced. Experimental studies on the Delta robot demonstrate the effectiveness of the proposed approach. The results show that the fractional-order PD controller achieves better tracking performance compared to the conventional PD controller, while both controllers exhibit similar control torques. It is also found that the fractional derivative order μ must be carefully chosen to balance tracking accuracy and smoothness of the control torque.

REFERENCES

[1] C. A. Monje, Y. Q. Chen, B. M. Vinagre, D. Xue, and V. Feliu-Batlle, “Fractional-order systems and controls: Fundamentals and applications,” London: Springer London, 2010. DOI: 10.1007/978-1-84996-335-0

[2] L. Debnath, “A brief historical introduction to fractional calculus,” International Journal of Mathematical Education in Science and Technology, vol. 35, no. 4, pp. 487–501, 2004. DOI: 10.1080/00207390410001686571

[3] Y. Wang, F. Yan, S. Jiang, and B. Chen, “Time delay control of cable driven manipulators with adaptive fractional-order nonsingular terminal sliding mode,” vol. 121, pp. 13–25, Jul. 2018. DOI: 10.1016/j.advengsoft.2018.03.004

[4] J. wan et al,, "Fractional order PID motion control based on seeker optimization algorithm for AUV," Oceans MTS/IEEE, pp. 1-4, 2018. DOI: 10.1109/OCEANS.2018.8604500

[5] S. Ghasemi, A. Tabesh and J. Askari-marnani, "Application of fractional calculs theory to robust controller design for wind turbine generators," IEEE transactions on energy conversion, vol. 29, no. 3, pp. 780-787, 2014.

[6] R. Clavel. “Conception d’un robot parallèle rapide à 4 degré de liberté,” [Doctoral thesis], Swiss Federal Institue of Technology Lausanne, 1991. DOI : 10.5075/epfl-thesis-925

[7] J. Brinker and B. Covers. “A survey on parallel robots with delta-like architecture,” The 14th IFToMM world Congress, 2015. DOI: 10.6567/IFToMM.14TH.WC.PS13.003

[8] A. Cadourey, “Dynamic modelling and mass matrix evaluation of the delta parallel robot for axes decoupling control,” Proceedings of IEEE/RSJ International Conference on Intelligent Robots and Systems IROS '96, vol. 3, pp. 1211–1218, 1996. DOI: 10.1109/IROS.1996.568973.

[9] C. E. Boudjedir, D. Boukhetala, and M. Bouri. "Nonlinear PD control of a Parallel Delta robot: Expermentals Results". International Conference on Electrical Sciences and Technologies in Maghreb (CISTEM), algeria, pp. 1-4, 2018. DOI: 10.1109/CISTEM.2018.8613618

[10] C. E. Boudjedir, D. Boukhetala, and M. Bouri, “Iterative learning control of multivariable uncertain nonlinear systems with nonrepetitive trajectory,” Nonlinear Dyn., vol. 95, pp. 2197–2208, 2019.

[11] C. E. Boudjedir, D. Boukhetala and M. Bouri. “Iterative Learning Control of a Parallel Delta Robot,” ICEECA, Lecture Notes in Electrical Engineering, vol. 522. Springer, Cham, doi: 10.1007/978-3-319-97816-1_6, 2017. DOI: 10.1007/978-3-319-97816-1_6

[12] C. E. Boudjedir, M. Bouri, and D. Boukhetala, “Model-free iterative learning control with nonrepetitive trajectories for second-order MIMO nonlinear systems—Application to a delta robot,” IEEE Trans. Ind. Electron., vol. 68, no. 8, pp. 7433–7443, Aug. 2021. DOI: 10.1109/TIE.2020.3007091.

[13] C. E. Boudjedir, M. Bouri and D. Boukhetala, "An Enhanced Adaptive Time Delay Control-Based Integral Sliding Mode for Trajectory Tracking of Robot Manipulators," in IEEE Transactions on Control Systems Technology, 2022. DOI: 10.1109/TCST.2022.3208491.

[14] C. E. Boudjedir, D. Boukhetala, and M. Bouri, “Nonlinear PD plus sliding mode control with application to a parallel delta robot,” J. Elect. Eng., vol. 69, no. 5, pp. 329–336, 2018. DOI: 10.2478/jee-2018-0048

[15] C. Karmokolias and R. Saeks, “A fractional representation approach to adaptive control,” 1980 19th IEEE Conference on Decision and Control including the Symposium on Adaptive Processes, 1980.

[16] J. Sabatier, P. Lanusse, P. Melchior, and A. Oustaloup, “Fractional order differentiation and robust control design,” Intelligent Systems, Control and Automation: Science and Engineering, 2015.

[17] C. I. Muresan and O. Prodan, “Vibration suppression in smart structures using fractional order PD controllers,” IEEE International Conference on Automation, Quality and Testing, Robotics, 2014. DOI: 10.1109/AQTR.2014.6857907

[18] A. Al-Mayyahi, A. A. Aldair, and C. Chatwin, “Control of a 3-RRR planar parallel robot using fractional order PID controller,” International Journal of Automation and Computing, vol. 17, no. 6, pp. 822–836, 2020.

[19] A. Dumlu and K. Erenturk, “Trajectory tracking control for a 3-dof parallel manipulator using fractional-order control,” IEEE Transactions on Industrial Electronics, vol. 61, no. 7, pp. 3417–3426, 2014. DOI: 10.1109/TIE.2013.2278964

[20] L. Angel and J. Viola, “Fractional order PID for tracking control of a parallel robotic manipulator type delta,” ISA Transactions, vol. 79, pp. 172–188, 2018. DOI: 10.1016/j.isatra.2018.04.010

[21] Q.-S. Zeng, G.-Y. Cao, and X.-J. Zhu, “The effect of the fractional-order controller's orders variation on the fractional-order control systems,” Proceedings. International Conference on Machine Learning and Cybernetics, 2002. DOI: 10.1109/ICMLC.2002.1176776.

[22] Y. Q. Chen, I. Petras, and D. Xue, “Fractional order control - A tutorial,” 2009 American Control Conference, 2009. DOI: 10.1109/ACC.2009.5160719.

[23] C. E. Boudjedir, M. Bouri, and D. Boukhetala, “Iterative learning control for trajectory tracking of a parallel delta robot,” Automatisierungstechnik, vol. 67, no. 2, pp. 145–156, 2019. DOI: 10.1515/auto-2018-0086

[24] C. E. Boudjedir and D. Boukhetala. "Adaptive robust iterative learning control with application to a Delta robot". Proceedings of the Institution of Mechanical Engineers, Part I: Journal of Systems and Control Engineering, vol. 235, no. 2, pp. 207-221, 2021. DOI: 10.1177/0959651820938531

Someya Amrane received the M.Sc. degree in control engineering from the École Nationale Polytechnique, Constantine, Algeria, in 2019. She is currently working toward the Ph.D. degree in the École Nationale Polytechnique, Algiers, Algeria. Her research interests include fractional-order control, sliding mode control, time delay control, and robotics.

Chems Eddine Boudjedir received the M.Sc. and Ph.D. degrees in control engineering from the École Nationale Polytechnique, Algiers, Algeria, in 2015 and 2019, respectively. He is currently an Associate Professor with the University of Science and Technology Houari Boumediene, Algiers. His research interests include iterative learning control, sliding mode control, time delay control, disturbance observer, and robotics.

Djamel Boukhetala graduated in automation in 1989 and received the Magister and Ph.D. degrees (Doctorat d’État) in automatic control from the École Nationale Polytechnique (ENP), Algiers, Algeria, in 1993 and 2002, respectively. From 1996 to 1999, he was the Head of the Department of Automatic Control. He was the Director of the Control Process Laboratory from 2005 to 2013 and the Director of Postgraduate Studies and Scientific Research at ENP from 2010 to 2019. He is currently a Full Professor in automatic control with ENP. He is currently a member of several scientific councils in higher education and scientific research institutions. His research interests are decentralized control, nonlinear control, fuzzy control, and artificial neural network control applied to robotics, smartgrids, and industrial processes.

Impacts of Changes in Climatic Conditions and Urbanization on Runoff at City Scale

Sana Ghezali and Mohamed Amine Boukhemacha

Abstract−Urbanization and climate change are increasingly recognized as key drivers of hydrological alterations in rapidly growing cities. This study assesses their combined and individual impacts on runoff generation in Algiers, Algeria, over the period 1992–2016 using the Soil Conservation Service Curve Number (SCS-CN) model. Land cover maps from the European Space Agency's Climate Change Initiative and long-term rainfall records were integrated with hydrological soil data to quantify runoff under three scenarios: (i) real conditions combining changes in climatic conditions and urbanization, (ii) fixed urban settings isolating climate effects, and (iii) fixed climatic conditions isolating urbanization impacts. Findings reveal that during the period 1992-2016, the city experienced an expansion of the impervious surfaces (from 19.86% to 41.48%) at the expense of other land covers. Moreover, the results show that although annual precipitation remained close to its baseline (608.25 mm·y^{-1}), runoff displayed a continuing upward shift above its baseline (70.04 mm·y^{-1}) after the early 2000s. Correlation analysis indicates that precipitation highly affects runoff variability ($R^2 = 0.695$) compared to urbanization impacts. Nevertheless, under the fixed climate conditions scenario, the 2-fold urban area expansion (with an increase of +108.4%) between 1992 and 2016 led to a +11.9% increase in runoff, underscoring its structural role in altering hydrological responses. These findings highlight the dual influence of the climatic conditions and land-use change on urban runoff dynamics and emphasize the need for integrated planning to enhance flood resilience and sustainable water management.

***Keywords*− Change in climatic conditions, Runoff, SCS-CN method, Urbanization, Water management.**

NOMENCLATURE

SCS-CN	Soil Conservation Service–Curve Number.
SWAT	Soil and Water Assessment Tool.
HEC-HMS	Hydrologic Engineering Center's Hydrologic Modeling System.
PRMS	Precipitation-streamflow modeling system.
CN	Curve number.
AMC	Antecedent moisture conditions.
CCI-LC	Climate Change Initiative Land Cover.
LULC	Land use and land cover.
HSG	Hydrological soil group.

I. INTRODUCTION

Cities in the Mediterranean region face growing challenges in managing water resources due to rapid urban expansion and climate change [1]. This dual pressure, where land-use transitions and changing rainfall patterns have affected hydrological responses. Rapid urban development changes land cover by replacing vegetation and permeable soils with impervious surfaces such as roads, rooftops, and pavements. This transformation disrupts the hydrological cycle by increasing surface runoff, modifying infiltration and groundwater recharge, and affecting evapotranspiration and water quality [2], [3], [4]. Consequently, the expansion of impervious areas and loss of vegetation significantly heighten flood risks [5].

In parallel, climate change amplifies these pressures through its direct influence on precipitation regimes. Shifts in rainfall intensity, duration, and frequency can intensify hydrological cycle response [6], particularly surface runoff [7], [8], producing both more severe floods and longer droughts. [9].

Several hydrological models were employed to assess runoff and study how changes in precipitation regimes and expansion of impervious surfaces affect surface runoff response, including SWAT [10], [11], [12], HEC-HMS [13], [14] and PRMS [15], [16]. Among these, the Soil Conservation Service Curve Number (SCS-CN) method has emerged as one of the most widely applied empirical models for runoff estimation, due to its relative simplicity, modest data requirements, and proven applicability across diverse climatic and land use contexts [17], [18], [19]. It has been extensively used to assess hydrological impacts of land-use change and climate variability in both urban and rural watersheds [20], [21].

Despite growing attention to the individual effects of climatic conditions and urbanization on runoff, relatively few studies have explicitly addressed their combined impacts over extended time periods. Understanding how these factors interact is essential for regions experiencing rapid urban expansion while simultaneously facing climate pressures. This study addresses this gap by investigating the long-term (1992–2016) runoff response of Algiers, a rapidly urbanizing Mediterranean city, under the impact of climate change and urbanization. Therefore, this study aims to identify the relative roles of precipitation variability and urban expansion (combined and isolated) in affecting runoff dynamics using the SCS-CN method.

II. STUDY ZONE

The study area is Algiers, the capital of Algeria, located on the Mediterranean coast of North Africa between 36°34′–36°49′N

Manuscript received October 8, 2025; revised November 16, 2025.

This work was supported by the Algerian Ministry of Higher Education and Scientific Research (grant contract No.: A17N01ES160220220001).

S. Ghezali is with the with LMGCE/LRS-EAU Laboratories, Ecole Nationale Polytechnique, Algiers, ALGERIA (e-mail: sana.ghezali@g.enp.edu.dz).

M.A. Boukhemacha is with LMGCE Laboratory, Ecole Nationale Polytechnique, Algiers, ALGERIA (e-mail: mohamed_amine.boukhemacha@g.enp.edu.dz).

Digital Object Identifier (DOI): 10.53907/enpesj.v5i2.341

latitude and 2°48′–3°23′E longitude (Fig.1). Based on the Köppen climate classification [22], the city experiences a Mediterranean climate, with an average annual temperature of 18 °C and mean precipitation of about 600 mm, most of which occurs during winter. Algiers covers a total area of 774 km², of which 44.1% was classified as urban land in 2020 [23]. The city has undergone rapid demographic growth, with its population increasing from 1.6 million in 1987 to 2.6 million in 1998, and surpassing 3 million by 2008 [24].

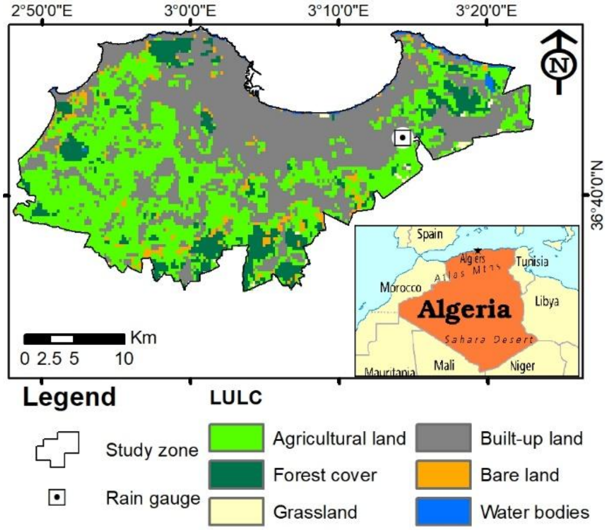

Fig. 1: Study zone location, land use map for 2022 [25] and rain gauge location

III. DATA AND METHODS

To better understand and evaluate how runoff responds to the impacts of climate change and urban development, this study applied the Soil Conservation Service–Curve Number (SCS-CN) model [26]. This method establishes a quantitative relationship between rainfall, land cover, soil type, and antecedent moisture conditions, therefore enabling reliable estimation of direct runoff. It is given by "(1)".

$$Q = \max\left(0, \frac{(P-I_a)^2}{(P-I_a)+S}\right) \ \wedge \ I_a = \lambda S \qquad (1)$$

$$\wedge \ S = \frac{25400}{\mathrm{CN}} - 254$$

where P [mm/day] denotes the precipitation, I_a [mm/day] refers to the initial abstraction, representing the portion of rainfall lost before the onset of runoff through processes such as vegetation interception, evaporation, depression storage, and initial infiltration. Q [mm/day] indicates the direct runoff. The parameter λ is a dimensionless coefficient typically set to 0.2, and S [mm/day] represents the potential maximum retention. The curve number (CN) is a dimensionless index that reflects the combined influence of soil type (Fig.2), land use/land cover, and hydrological conditions. CN values also vary according to antecedent moisture conditions (AMC), which are determined by the cumulative rainfall over the preceding five days. Three AMC classes are defined: AMC I (dry), AMC II (average), and AMC III (wet), as summarized in Table I.

Table. I
ANTECEDENT MOISTURE CONDITIONS CLASSIFICATION [26]

Class	Condition description	Total 5 days of antecedent rainfall	
		Dormant season	Growing season
AMC I	Dry condition	< 13 mm	< 36 mm
AMC II	Average condition	13 to 28 mm	36 to 53 mm
AMC III	Almost completely wet situation	> 28 mm	53 mm

In this study, two datasets were integrated to generate yearly CN2 maps (corresponding to AMC II) for the period 1992–2016. The first dataset consisted of land cover maps derived from the European Space Agency's Climate Change Initiative Land Cover (CCI-LC) product [25]. With a spatial resolution of 300 m, the CCI-LC dataset offers a yearly consistent global coverage and is particularly suitable for long-term land use and land cover assessments. For this analysis, the original land cover classes were reclassified into six categories relevant to hydrological modeling: built-up land, agricultural land, forest cover, grassland, water bodies, and bare land (Fig.3). This reclassification enabled the detection of urban expansion and land use transitions over time, thereby facilitating the assessment of their effects on runoff dynamics in combination with climate variability. The second dataset was a hydrological soil group (HSG) map derived from the soil map (Fig.2). Based on these inputs, CN2 values were produced and subsequently used to compute and map CN1 (AMC I) and CN3 (AMC III) through equations "(2)" and "(3)", respectively producing daily CN maps over the studied period.

$$\mathrm{CN1} = \frac{\mathrm{CN2}}{2.281 - 0.01281 \times \mathrm{CN2}} \qquad (2)$$

$$\mathrm{CN3} = \frac{\mathrm{CN2}}{0.427 + 0.00573 \times \mathrm{CN2}} \qquad (3)$$

In addition to land cover and soil data, meteorological inputs were incorporated into the analysis. Daily precipitation records were obtained from the Dar El-Beida rain gauge, situated within the study area (Fig.1) and managed by the National Water Resources Agency. The precipitation record used covers the period 1992–2016 and served as the primary climatic input for the quantitative estimation of runoff.

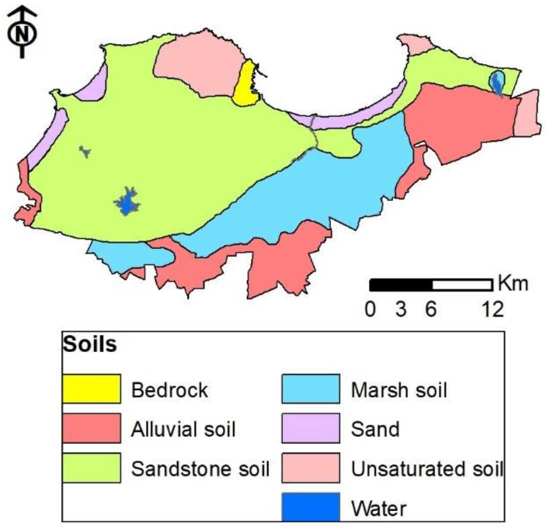

Fig. 2: Soil map of Algiers based on data from **[27]**

To investigate the potential impacts of changes in climatic conditions and urban development on runoff generation, three analytical scenarios were designed:

- Scenario 1: Combined effect (real system analysis). This scenario integrates both changes in climatic conditions and urbanization effects simultaneously, thereby representing the actual evolution of the system and allowing an evaluation of runoff response (*Q*) under real-world conditions.
- Scenario 2: Climate-only conditions (fixed urban extent). In order to isolate the role of climatic variability, LULC was held constant at its 1992 state, while only precipitation and climatic conditions were allowed to vary. This provides insights into the impact of the change in climatic conditions independently of urban expansion.
- Scenario 3: Urbanization-only settings (fixed climate conditions). Conversely, to assess the influence of urban development, climate conditions were fixed to those of the baseline year 1992, while urban expansion was allowed to vary. This isolates the hydrological impacts of urban growth from those of the climatic conditions.

IV. RESULTS AND DISCUSSION

The present study investigates the impacts of changes in climatic conditions and urbanization on runoff (combined and separated) at the city scale during the period 1992-2016. The analysis will be presented first in terms of urban development. (examining the spatiotemporal of land use and land cover (LULC) changes and patterns in the areas across the period 1992-2016), while the second analysis relies on the assessment of the precipitation variability during the same period. And finally, the evaluation of runoff quantity and response under three scenarios: (1) the combined effect of urbanization and changes in climatic conditions, (2) climate-only conditions, and (3) urbanization-only settings.

A. *LULC spatiotemporal analysis*

The spatiotemporal assessment of LULC between 1992 and 2016 (Fig.3-4) highlights pronounced urban expansion across the study area. Built-up areas more than doubled, rising from 19.86% to 41.48%, which corresponds to an average annual growth rate of +0.9%. Agricultural land exhibited the most significant decline, decreasing from 57.32% to 43.53% at a rate of –0.57% per year, indicating a substantial conversion of fertile land into urban surfaces. Grassland showed only a marginal reduction, decreasing from 1.11% to 0.5% (–0.03% annually). In contrast, forest cover registered a slight but steady gain, increasing from 8.66% to 9.77% (0.05% annually), which may reflect localized reforestation or conservation initiatives. Bare land, however, demonstrated considerable changes, dropping from 11.61% to 3.64% over the study period (-0.33% annually), possibly due to urban occupation or conversion into other land uses. Water bodies also declined slightly, from 1.44% to 1.08%.

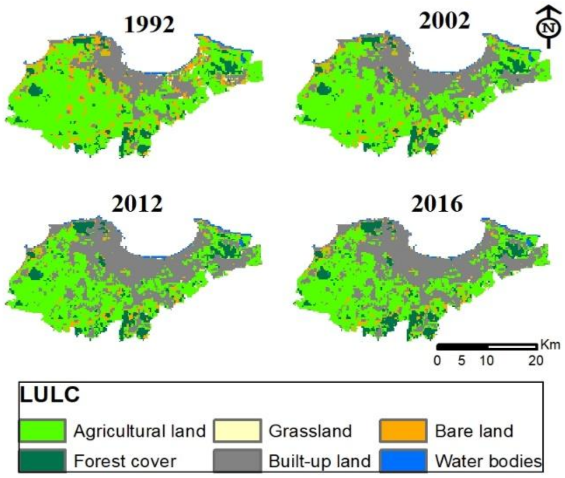

Fig. 3: LULC spatiotemporal evolution in Algiers during 1992-2022

Overall, the observed expansion of built-up areas has come largely at the expense of other vegetated classes, underscoring the intensity of urban growth and its transformative effect on the city fabric. This urban development results in increased pressure on natural resources (e.g., water), while also impacting the natural hydrological cycle by altering infiltration, groundwater recharge, and surface runoff, and elevating flood risks [28], [29], [30], [31], [23].

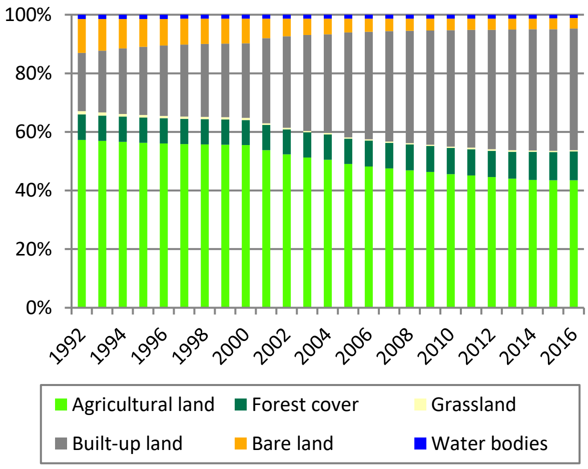

Fig. 4: Trend of LULC changes during 1992-2016.

B. *Temporal variability of precipitation and runoff at the city scale*

The precipitation regime during the studied period reflects a temporal variability (Fig. 5) closely oscillating around the long-term baseline (1992-2016) of 608.25 mm·y⁻¹. Moreover, the long-term polynomial trend remains nearly flat, with values during the mid-2000s that slightly exceed this baseline.

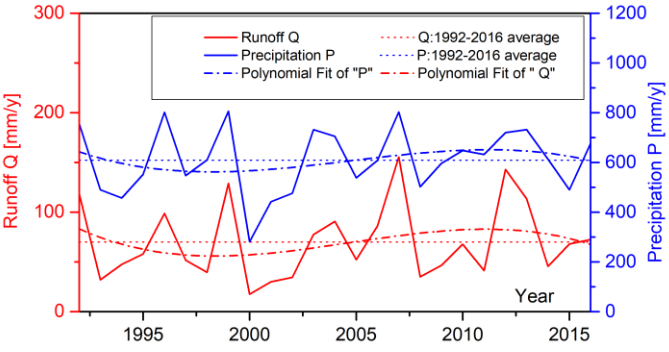

Fig. 5 precipitation variability and runoff patterns under real system scenario for Algiers during the period 1992-2016.

On the other hand, the runoff trend under the combined effects of changes in climatic conditions and urbanization (Fig. 5) exhibits more pronounced variability compared to the long-term baseline (1992-2016) runoff of 70.04 mm·y⁻¹. During the 1990s, the trend generally remained below the multiannual average. However, from the mid-2000s, the runoff values show an upward trajectory, gradually surpassing the long-term baseline. These findings suggest that climate variability (precipitation patterns) modulated the timing of peaks, but the continuing elevation of runoff, even during years of near-average precipitation, points to runoff response to urbanization, where the urban area increased. Similar findings were reported in other urban cities such as Bengaluru, known as the Silicone city of India [32], Robe town, Ethiopia [33], Beijing-Tianjin-Hebei, China [34].

A. Impacts of urbanization and changes in climatic conditions

To identify the dominant factor influencing runoff variability, a comparative analysis was performed under the real system scenario, examining the relationships of runoff with both precipitation and the proportion of urbanized area (Fig.6). The results demonstrate a strong linear relationship between precipitation and runoff (R^2 = 0.695), indicating that approximately 23.8% of rainfall was transformed into runoff during the period 1992–2016. In contrast, the correlation between runoff and urban area percentage was weak (R^2 = 0.023), suggesting that precipitation exerted far greater control on runoff dynamics than urban expansion. This highlights that, during the studied period, climate variability (particularly rainfall fluctuations) was the primary driver of runoff changes in the city.

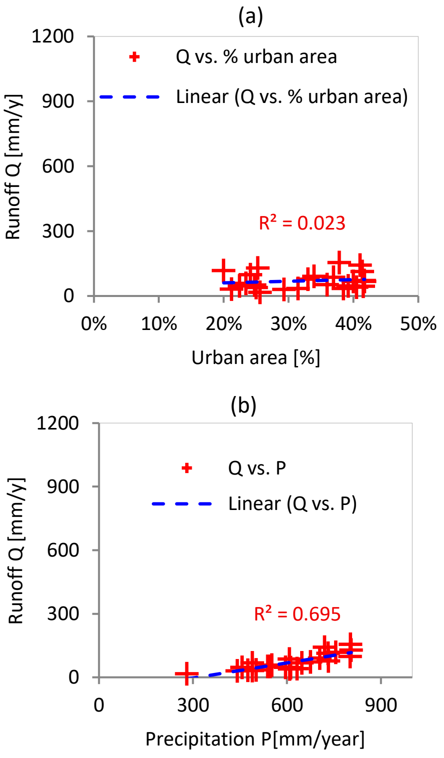

Fig. 6: Correlation between runoff under real system scenario and (a) the percentage of the urban area and (b) the precipitation.

The runoff response under urbanization-only effects (fixed climate conditions) demonstrates a gradual increase relative to the 1992 reference year (Fig.7). From 1992 to around 2000, the increase remained modest, reflecting the relatively slow rate of urban expansion during this period. However, beginning in the early 2000s, the urban-induced runoff effects became more pronounced, with a steady rise observed until 2016. This period coincides with accelerated urban growth in Algiers, which expanded impervious surfaces such as roads and buildings (this aspect was also reported by [35]), resulting in enhanced surface runoff. During 1992-2016, the urban area, with respect to 1992, expanded by +108.4%, which resulted in a +11.9% increase in runoff in 2016. Importantly, this effect persists regardless of precipitation variability, underscoring the structural modification of the city's capacity to regulate runoff. A similar trend was reported by [36], where a 10% increase in impervious surfaces resulted in a 12% rise in runoff.

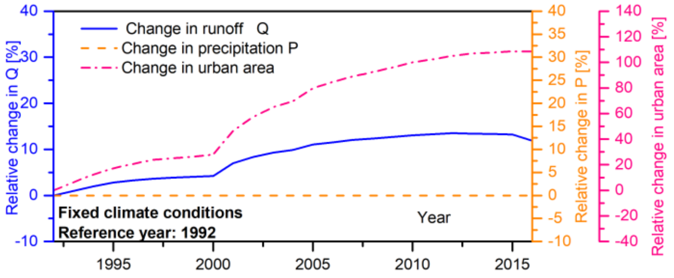

Fig. 7: Relative change (with respect to the year 1992) in precipitation, the urban area percentages and the runoff under a fixed climatic conditions scenario.

On the other hand, when only climatic influences are considered (with fixed urbanization settings at 1992 constants), runoff exhibits pronounced interannual variability that closely follows precipitation patterns (Fig.8). Relative change in precipitation fluctuates between –62.83% in 2000 and +6.55% in 1999, while relative change in the produced runoff ranges from –85.90% in 2000 to +19.63% in 2007. These findings highlight the hydrological system's (particularly runoff) heightened sensitivity to rainfall variability. This aspect was reported in recent studies [37], [38], [39], [40].

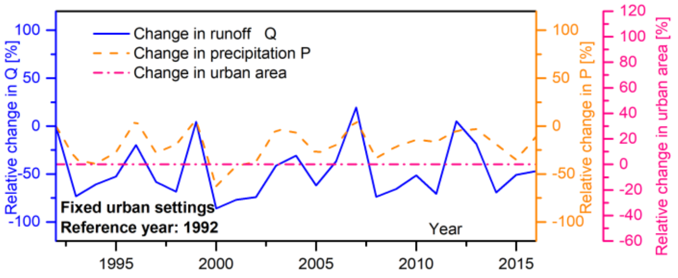

Fig. 8: Relative change (with respect to the year 1992) in precipitation, the urban area percentages and the runoff under a fixed urban settings scenario.

In terms of limitations, the following points summarize the main constraints of this study.

- This study used precipitation data from the Dar El-Beida station which offers the only long, daily, continuous, and quality-controlled rainfall record. However, it may not fully represent spatial rainfall variability across Algiers.
- The absence of continuous discharge records limited the ability to validate simulated runoff directly.
- The study relied on the CCI–LC products with a validated accuracy (approximately 75% globally, as reported by ESA [41]) and applied a standardized reclassification approach. This reclassification could not be verified against ground observations due to the lack of local survey data.

V. CONCLUSION

This study investigated the combined and individual impacts of changes in climatic conditions and urbanization on runoff generation in Algiers from 1992 to 2016, using the SCS-CN method. The spatiotemporal analysis of LULC during the period 1992-2016 indicates an increase in built-up areas from 19.86% to 41.48%, corresponding to an annual growth rate of +0.9%. This urban development was at the expense of other land cover, particularly the agricultural land (reduced from 57.32% to 43.53% at a yearly rate of –0.57%), leading to intensifying pressure on natural resources, altering hydrological cycles, and contributing to environmental degradation. The findings also reveal that precipitation is the dominant driver of interannual runoff variability, as reflected in the strong correlation ($R^2 = 0.695$) between rainfall and runoff, indicating that 23.8% of precipitation contributes to runoff during the study period. Nevertheless, the continuing upward shift in runoff relative to the long-term baseline, even during periods of near-average precipitation, highlights the role of urban expansion in structurally influencing the city's hydrological response. By 2016, urban areas had increased by +108.4% relative to 1992, resulting in an estimated +11.9% rise in runoff under urbanization-only conditions. The results also underscore that changes in climatic conditions amplify short-term fluctuations in runoff through influences on rainfall intensity, while urbanization contributes to a permanent change in the runoff regime by modifying infiltration and enhancing surface flows. Together, these drivers not only increase annual runoff but also elevate the risks of flooding and impact groundwater recharge, thereby intensifying pressure on urban water management systems.

Overall, this study indirectly demonstrates the importance of integrating land-use planning and climate adaptation strategies to mitigate hydrological risks in rapidly urbanizing Mediterranean cities. The methodology and findings provide a transferable framework for other regions facing similar challenges of balancing urban growth with climate adaptation. Future research should aim to couple SCS-CN modeling with advanced climate projections and nature-based solutions (such as green infrastructure to enhance infiltration and reduce runoff) to further explore pathways for sustainable water management.

ACKNOWLEDGMENT

This work was conducted within the MESRS-PRFU project WatSedMan (grant contract No. A17N01ES160220220001) implemented within the LMGCE laboratory of ENP

REFERENCES

[1] C. Leduc, A. Pulido-Bosch, and B. Remini, "Anthropization of groundwater resources in the Mediterranean region: processes and challenges," *Hydrogeol J*, vol. 25, no. 6, pp. 1529–1547, Sep. 2017, doi: 10.1007/s10040-017-1572-6.

[2] S. I. Elmahdy and M. M. Mohamed, "The impact of land use land cover on groundwater level and quality in the Emirate of Abu Dhabi, UAE: an integration approach using remote sensing and hydrological data," *Geocarto International*, vol. 38, no. 1, Dec. 2023, doi: 10.1080/10106049.2023.2272664.

[3] H. Liu, H. Yan, and M. Guan, "Evaluating the effects of topography and land use change on hydrological signatures: a comparative study of two adjacent watersheds," *Hydrol. Earth Syst. Sci.*, vol. 29, no. 8, pp. 2109–2132, Apr. 2025, doi: 10.5194/hess-29-2109-2025.

[4] Z. Yin, G. Liu, Z. Zheng, and X. Li, "Sustainable Stormwater Management: Runoff Impact of Urban Land Layout with Multi-Level Impervious Surface Coverage," *Sustainability*, vol. 17, no. 8, p. 3511, Apr. 2025, doi: 10.3390/su17083511.

[5] Ş. Öztürk, K. Yılmaz, A. E. Dinçer, and V. Kalpakcı, "Effect of urbanization on surface runoff and performance of green roofs and permeable pavement for mitigating urban floods," *Nat Hazards*, vol. 120, no. 13, pp. 12375–12399, Oct. 2024, doi: 10.1007/s11069-024-06688-w.

[6] P. Yeste *et al.*, "Projected hydrologic changes over the north of the Iberian Peninsula using a Euro-CORDEX multi-model ensemble," *Science of The Total Environment*, vol. 777, p. 146126, Jul. 2021, doi: 10.1016/j.scitotenv.2021.146126.

[7] X. Huang and L. Qiu, "Impacts of Climate Change and Land Use/Cover Change on Runoff in the Huangfuchuan River Basin," *Land*, vol. 13, no. 12, p. 2048, Nov. 2024, doi: 10.3390/land13122048.

[8] N. Jiang *et al.*, "The impact of future climate and land use changes on runoff in the Min-Tuo River Basin," *Journal of Water and Climate Change*, vol. 15, no. 11, pp. 5518–5539, Nov. 2024, doi: 10.2166/wcc.2024.384.

[9] IPCC, "Summary for Policymakers. In: Masson-Delmotte V, Zhai PM, Pirani A et al (eds) Climate Change 2021: The Physical Science Basis. Contribution of Working Group I to the Sixth Assessment Report of the Intergovernmental Panel on Climate Change," *Cambridge University Press, Cambridge, United Kingdom and New York, NY, USA*, 2021, doi: 10.1017/9781009157896.001.

[10] E. Szalińska *et al.*, "Total nitrogen and phosphorus loads in surface runoff from urban land use (city of Lublin) under climate change," *Environ Sci Pollut Res*, vol. 31, no. 35, pp. 48135–48153, Jul. 2024, doi: 10.1007/s11356-024-34365-9.

[11] D. Gebrie Habte, S. Belliethathan, and T. Ayenew, "Analysis of Hydrological Response to Climate and Land Use Land Cover Changes in Jewha Watershed Using SWAT Model, Ethiopia," *Air, Soil and Water Research*, vol. 17, p. 11786221241306768, May 2024, doi: 10.1177/11786221241306768.

[12] M. Li *et al.*, "Integration of the vegetation phenology module improves ecohydrological simulation by the SWAT-Carbon model," *Hydrology and Earth System Sciences*, vol. 29, no. 8, pp. 2081–2095, Apr. 2025, doi: 10.5194/hess-29-2081-2025.

[13] B. Abdelkebir, E. Mokhtari, and B. Engel, "Assessment of land use and land cover changes on hydrological responses in the Wadi Soummam watershed, Algeria using the HEC–HMS model," *Water Practice & Technology*, vol. 19, no. 9, pp. 3555–3577, Sep. 2024, doi: 10.2166/wpt.. 2024.224.

[14] L. Djellit, F. Laouacheria, and R. Morbidelli, "Assessment of the impact of LULC changes on peak discharge and runoff volume in Kebir river catchment Northeastern of Algeria," *Model. Earth Syst. Environ.*, vol. 10, no. 3, pp. 3711–3726, Jun. 2024, doi: 10.1007/s40808-024-01981-w.

[15] P. Bosompemaa, A. Brookfield, S. Zipper, and M. C. Hill, "Using national hydrologic models to obtain regional climate change impacts on streamflow basins with unrepresented processes," *Environmental Modelling & Software*, vol. 183, p. 106234, Jan. 2025, doi: 10.1016/j.envsoft.2024.106234.

[16] V. L. R. Ii, "Application of the Precipitation-Runoff Modeling System (PRMS) to simulate the streamflows and water balance of the Red River Basin, 1980–2016," U.S. Geological Survey, 2022–5105, 2023. doi: 10.3133/sir20225105.

[17] M. L. Kotti and T. Hermassi, "Regional Calibration of SCS-CN Model for Ungauged Basins and Flood Modeling Using GIS and HEC-HMS/RAS: A Case Study for the Sidi Salem-Mdjez El Beb Section (Medjerda Valley-Tunisia)," in *Recent Advances in Environmental Science from the Euro-Mediterranean and Surrounding Regions (4th Edition)*, M. Ksibi, A. Sousa, O. Hentati, H. Chenchouni, J. Lopes Velho, A. Negm, J. Rodrigo-Comino, R. Hadji, S. Chakraborty, and A. Ghorbal, Eds., Cham: Springer Nature Switzerland, 2024, pp. 825–828. doi: 10.1007/978-3-031-51904-8_179.

[18] M. A. Boukhemacha, "Soil Conservation Service-Curve Number method-based historical analysis of long-term (1936–2016) temporal evolution of city-scale potential natural groundwater recharge from precipitation: case study Algiers (Algeria)," *Environ Monit Assess*, vol. 195, no. 10, p. 1168, Oct. 2023, doi: 10.1007/s10661-023-11815-4.

[19] H. M. Aragaw and S. K. Mishra, "Clarification of issues and long-duration hydrologic simulation SCS-CN-based proxy modelling," *Acta Geophys.*, vol. 70, no. 2, pp. 729–756, Apr. 2022, doi: 10.1007/s11600-022-00730-w.

[20] A. Mulu, S. B. Kassa, M. L. Wossene, T. M. Meshesha, A. A. Fenta, and Y. B. Hailu, "Runoff estimation using the SCS-CN method and GIS: a case study in the Wuseta watershed, upper blue Nile Basin, Ethiopia," *Discov Water*, vol. 5, no. 1, p. 32, Apr. 2025, doi: 10.1007/s43832-025-00216-y.

[21] M. H. Huq, M. M. Rahman, and G. M. J. Hasan, "Climate-resilient urban drainage planning: An approach using a GIS-based SCS-CN model," *Journal of Water and Climate Change*, vol. 15, no. 7, pp. 2978–2991, Jun. 2024, doi: 10.2166/wcc.2024.616.

[22] W. Koppen, "Das geographische System de Klimate," *Handbuch der klimatologie*, 1936.

[23] S. Ghezali and M. A. Boukhemacha, "Spatiotemporal change analysis and ANN/CCI LC products- based future predictions of land use and land cover: Algiers city, (Algeria) case study," in *2nd International Conference on Future Challenges in Sustainable Urban Planning & Territorial Management: SUPTM 2024*, Universidad Politécnica de Cartagena, Jan. 2024. doi: 10.31428/10317/13564.

[24] National office of statistics, "National office of statistics." 2013. [Online]. Available: www.ons.dz

[25] "ESA/CCI viewer." Accessed: May 21, 2024. [Online]. Available: http://maps.elie.ucl.ac.be/CCI/viewer/

[26] USDA, *National engineering handbook, Soil Conservation Service*. Washington, D.C.: US Department of Agriculture, Washington, D.C., 1971.

[27] S. K. Salvaradjou, L. Montanarella, O. Spaargaren, and D. Dent, "European digital archive of soil maps (EuDASM), volume 1: soil maps of Africa," Office for Official Publications of the European Communities, 2005. Accessed: Nov. 06, 2024. [Online]. Available: https://library.wur.nl/WebQuery/wurpubs/fulltext/26812

[28] I. S. Astuti, K. Sahoo, A. Milewski, and D. R. Mishra, "Impact of Land Use Land Cover (LULC) Change on Surface Runoff in an Increasingly Urbanized Tropical Watershed," *Water Resour Manage*, vol. 33, no. 12, pp. 4087–4103, Sep. 2019, doi: 10.1007/s11269-019-02320-w.

[29] G. C. G. Da Silva, P. C. D. O. Campos, M. D. M. Reis, and I. Paz, "Spatiotemporal Land Use and Land Cover Changes and Associated Runoff Impact in Itaperuna, Brazil," *Sustainability*, vol. 16, no. 1, p. 325, Dec. 2023, doi: 10.3390/su16010325.

[30] M. Banjara, A. Bhusal, A. B. Ghimire, and A. Kalra, "Impact of Land Use and Land Cover Change on Hydrological Processes in Urban Watersheds: Analysis and Forecasting for Flood Risk Management," *Geosciences*, vol. 14, no. 2, p. 40, Feb. 2024, doi: 10.3390/geosciences14020040.

[31] V. S. Felix and A. Ribeiro Neto, "Hydrological modeling of LULC and climate change scenarios in a hydrographic basin in the semiarid region of Brazil.," *Rev. Bras. Geog. Fis.*, vol. 18, no. 2, pp. 1364–1383, Feb. 2025, doi: 10.26848/rbgf.v18.2.p1364-1383.

[32] A. R. Nilap, H. N. Rajakumara, A. Aldrees, H. Sh. Majdi, and W. A. Khan, "Storm water runoff studies in built-up watershed areas using curve number and remote sensing techniques," *Discov Sustain*, vol. 6, no. 1, p. 26, Jan. 2025, doi: 10.1007/s43621-025-00828-3.

[33] T. S. Bibi, K. G. Kara, H. J. Bedada, and R. D. Bededa, "Application of PCSWMM for assessing the impacts of urbanization and climate changes on the efficiency of stormwater drainage systems in managing urban flooding in Robe town, Ethiopia," *Journal of Hydrology: Regional Studies*, vol. 45, p. 101291, Feb. 2023, doi: 10.1016/j.ejrh.2022.101291.

[34] X. Ju, W. Li, J. Li, L. He, J. Mao, and L. Han, "Future climate change and urban growth together affect surface runoff in a large-scale urban agglomeration," *Sustainable Cities and Society*, vol. 99, p. 104970, Dec. 2023, doi: 10.1016/j.scs.2023.104970.

[35] B. Bouchachi and Y. Zhong, "MONITORING URBAN LAND COVER/LAND USE CHANGE IN ALGIERS CITY USING LANDSAT IMAGES (1987–2016)," *Int. Arch. Photogramm. Remote Sens. Spatial Inf. Sci.*, vol. XLII-2/W7, pp. 1083–1090, Sep. 2017, doi: 10.5194/isprs-archives-XLII-2-W7-1083-2017.

[36] M. M. Khanaum and M. S. Borhan, "Effects of Increasing Rainfall Depths and Impervious Areas on the Hydrologic Responses," *OJMH*, vol. 13, no. 02, pp. 114–128, 2023, doi: 10.4236/ojmh.2023.132006.

[37] A. Wypych and Z. Ustrnul, "Precipitation and hydrological extremes during the warm season in response to climate change: the example from the Polish Carpathians," *Reg Environ Change*, vol. 24, no. 2, p. 90, May 2024, doi: 10.1007/s10113-024-02252-1.

[38] E. Bilodeau *et al.*, "Evaluation of the Impact of Rainfall Increases on Runoff in Urban Watersheds," *JWMM*, 2025, doi: 10.14796/JWMM.C559.

[39] S. B. Kimbi, S. Onodera, K. Wang, I. Kaihotsu, and Y. Shimizu, "Assessing the Impact of Urbanization and Climate Change on Hydrological Processes in a Suburban Catchment," *Environments*, vol. 11, no. 10, p. 225, Oct. 2024, doi: 10.3390/environments11100225.

[40] Y. Yang, D. Z. Zhu, M. R. Loewen, W. Zhang, B. Van Duin, and K. Mahmood, "Impacts of climate change on urban stormwater runoff quantity and quality in a cold region," *Science of The Total Environment*, vol. 954, p. 176439, Dec. 2024, doi: 10.1016/j.scitotenv.2024.176439.

[41] ESA, "Land Cover CCI PRODUCT USER GUIDE VERSION 2." The European Space Agency, 2014.

Sana Ghezali was born in Chechar/Khenchela, Algeria in 1992. She received the Engineer's degrees in Hydraulic Engineering from the High National School of Hydraulics, Blida, Algeria, in 2017. She is currently a Ph.D. student at the Hydraulic Department at Ecole Nationale Polytechnique (ENP) of Algiers. Her current research interests include satellite image processing, land use and land cover mapping, hydrologic modeling, and the impacts of climate change.

Mohamed Amine Boukhemacha (biograpgy is not available)

Food Freshness Evaluation Using a CLIP-Based Architecture

Md. Siam Ansary, Amina Brinto, and Shaila Sajnin Keya

Abstract—In this work, we present an efficient deep learning framework for automated fresh and stale food classification using transfer learning with a pretrained CLIP-based feature extractor. The proposed system employs frozen vision transformer (ViT) embeddings from CLIP as generalized visual descriptors and integrates them with a lightweight multi-layer perceptron (MLP) classifier for binary classification. To enhance generalization, extensive data augmentation and stratified dataset partitioning were applied to the publicly available Fresh and Stale Classification dataset. Experimental results reveal a consistent improvement across ten training epochs, achieving a final test accuracy of 97.99%, F1-score of 0.9808, and ROC–AUC of 0.9985. The proposed model demonstrates excellent discriminative performance, robust convergence, and strong generalization capabilities while maintaining computational efficiency. These results confirm the suitability of CLIP-based visual representations for high-accuracy food quality assessment and real-time freshness detection applications.

***Keywords*—image classification, clip, food freshness, health.**

NOMENCLATURE

CLIP	Contrastive Language-Image Pre-training.
MLP	Multilayer perceptron.
ViT	Vision Transformers.
CNN	Convolutional Neural Network.
ACC	Accuracy.
P	Precision.
R	Recall.
F1	F1-score.
SP	Specificity.
ROC	Receiver Operating Characteristic.
AUC	Area under the curve.
MCC	Matthews Correlation Coefficient.
CUDA	Compute Unified Device Architecture.
GPU	Graphics Processing Unit.

I. INTRODUCTION

Food quality assessment plays a critical role in ensuring consumer safety, reducing waste, and maintaining supply-chain efficiency. Traditional approaches for freshness detection rely heavily on manual inspection or sensor-based measurements, which are time-consuming, labor-intensive, and prone to human error. Recent advancements in deep learning and computer vision have enabled automated food-quality recognition by leveraging large-scale image datasets and pretrained models. However, many existing solutions depend on fine-tuning deep convolutional networks, which require significant computational resources and domain-specific data.

To address these limitations, this study proposes a transfer-learning–based classification framework that integrates pretrained CLIP (Contrastive Language–Image Pretraining) embeddings with a lightweight Multi-Layer Perceptron (MLP) classifier. CLIP's vision transformer (ViT-B/16) backbone was employed as a fixed feature extractor to capture rich semantic and textural representations from images of food items. The extracted features were subsequently classified using a compact, fully connected MLP network. This approach reduces training cost while maintaining high discriminative performance.

The proposed model was evaluated on the publicly available Fresh and Stale Classification dataset from Kaggle. The data were divided into training, validation, and test subsets using stratified sampling to maintain class balance. The system achieved outstanding accuracy and F1-score, demonstrating the effectiveness of pretrained transformer features for specialized classification tasks. The major contributions of this research are as follows:

1. Development of a CLIP-based feature extraction framework for food freshness classification without end-to-end fine-tuning.

2. Implementation of a lightweight MLP classifier optimized for fast convergence and minimal computational overhead.

3. Comprehensive evaluation using multiple performance metrics including accuracy, precision, recall, F1-score, ROC–AUC, and Matthews correlation coefficient.

4. Empirical validation showing that frozen CLIP embeddings can achieve near state-of-the-art results on a small-scale, domain-specific dataset.

Manuscript received 18 October 2025; revised 30 November 2025.

Md. Siam Ansary is with the Department of Computer Science and Engineering (CSE), Ahsanullah University of Science and Technology, Dhaka, BANGLADESH. (e-mail: siamansary.cse@gmail.com).

Amina Brinto is with the Department of Obstetrics and Gynaecology, Kurmitola General Hospital, Dhaka, Bangladesh. (e-mail: aminabrinto@gmail.com).

Shaila Sajnin Keya is with the Institute of Nutrition and Food Science, University of Dhaka, BANGLADESH. (e-mail: shailasajninkeya1@gmail.com).

Digital Object Identifier (DOI): 10.53907/enpesj.v5i2.344

The experimental findings highlight that transfer learning using CLIP-derived representations provides a powerful and efficient pathway for food-quality classification, opening avenues for deployment in industrial inspection systems, automated retail environments, and mobile consumer applications.

II. LITERATURE REVIEW

Yuan *et al.* [1] worked on vegetable and fruit freshness detection using deep visual features. They extracted CNN-based representations from RGB images and trained a classifier that achieved high recognition accuracy for freshness identification across multiple produce categories.

Gao *et al.* [2] developed a food image classification model utilizing a Vision Transformer (ViT) with extensive data and feature augmentation. Their framework significantly outperformed conventional CNN architectures, showing higher precision on benchmark food datasets.

Jo *et al.* [3] conducted research on fresh meat quality assessment through hyperspectral imaging (HSI). By integrating spatial–spectral CNNs, they predicted physicochemical properties related to meat freshness and demonstrated substantial gains over RGB-only models.

Choi *et al.* [4] proposed a hybrid model combining hyperspectral imaging and chemometric analysis for predicting pork freshness. The model accurately estimated total volatile basic nitrogen (TVB-N) values and sensory freshness scores, confirming the potential of HSI for non-destructive freshness assessment.

Lun *et al.* [5] presented a comprehensive review of deep learning–enhanced spectroscopic technologies for food quality analysis. Their study emphasized the synergy between deep neural networks and spectral sensing methods in evaluating ripeness, adulteration, and spoilage.

Sonwani *et al.* [6] worked on an integrated food spoilage monitoring system employing multiple sensors and machine learning algorithms. The framework successfully detected early spoilage signs under real-world conditions by analyzing volatile gas emissions and environmental parameters.

Shu *et al.* [7] investigated fruit freshness classification using a ResNet-101 backbone enhanced with non-local attention mechanisms. Their model achieved superior recall and F1-score on fruit datasets with varying freshness levels, proving the effectiveness of attention-based CNNs.

Nikzadfar *et al.* [8] reviewed hyperspectral imaging and artificial intelligence integration for food quality and safety. They analyzed recent methods that combine spatial–spectral data with deep learning architectures for rapid and non-invasive freshness detection.

Gatti *et al.* [9] applied CLIP-based transfer learning for visual verification in food packaging. They extracted frozen CLIP embeddings and trained lightweight classifiers to detect mismatches in food order packaging, achieving high accuracy in industrial inspection environments.

Mehdizadeh *et al.* [10] explored AI-driven, non-destructive detection of meat freshness using spectral sensors. Their model correlated deep-learning predictions with chemical indicators of spoilage, reaching ROC–AUC scores above 0.95.

Varga *et al.* [11] investigated fruit ripeness estimation using hyperspectral imaging combined with deep learning. They applied convolutional neural networks to predict ripeness stages with strong generalization across different fruit types.

Anwar *et al.* [12] conducted a review on food quality assessment using machine learning and sensors. Their study concluded that sensor fusion, combining electronic nose, imaging, and spectral data, enhances reliability in freshness classification.

Radford *et al.* [13] introduced CLIP (Contrastive Language–Image Pretraining), which enabled large-scale visual–language representation learning. Their model set a foundation for zero-shot transfer learning, later utilized for various food classification tasks.

Dosovitskiy *et al.* [14] developed the Vision Transformer (ViT) architecture that processes image patches through self-attention mechanisms. ViT demonstrated superior performance on image classification benchmarks and influenced modern food-vision approaches.

Bossard *et al.* [15] proposed the Food-101 dataset and baseline CNN models for food category classification. This dataset has since been widely used for evaluating and fine-tuning deep food recognition systems.

Ghosh *et al.* [16] presented NoisyViT, a robust vision transformer framework for food image recognition under noisy environments. Their approach enhanced classification stability and improved performance on low-quality food imagery.

Liu *et al.* [17] conducted a comprehensive review on deep learning in food image recognition. They discussed CNNs, transformers, and multimodal architectures, highlighting recent advances and challenges in large-scale food datasets.

III. IMPLEMENTATION METHODOLOGY

The implementation pipeline was designed to systematically train, validate, and evaluate a deep learning model for binary image classification between *fresh* and *stale* food samples. The overall workflow comprises six major stages: dataset preparation, preprocessing and augmentation, model architecture design, feature extraction, classifier training, and evaluation. Each component was implemented in Python using PyTorch and the `timm` vision library, executed in Google Colab with GPU acceleration.

A. Dataset Preparation

The "Fresh and Stale Classification" dataset from Kaggle was used for experimentation. The dataset consists of images categorized into two classes: *fresh* and *stale*. Images were organized into a directory structure compatible with `torchvision.datasets.ImageFolder`, enabling automatic label assignment based on folder names. The dataset was split into 80% training, 10% validation, and 10% testing subsets using *Stratified Shuffle Split* to preserve class distribution across all splits.

B. Data Preprocessing and Augmentation

To ensure robust feature learning and to prevent overfitting, distinct preprocessing pipelines were defined for training and validation phases using the `torchvision.transforms` module. Training transformations included random resized cropping, horizontal flipping, and color jittering to introduce variability in scale, orientation, and illumination. Validation and test transformations involved only resizing and center cropping for consistency. All images were normalized using the standard ImageNet mean and standard deviation values to align with the normalization of pretrained networks.

C. Feature Extraction Using Pretrained Backbone

To leverage transfer learning, a pretrained feature extractor was employed rather than training an entire convolutional network from scratch. The Vision Transformer (ViT-B/16) variant of CLIP (`vit_base_patch16_clip_224.openai`) was loaded using the `timm` library. The model's classification head was removed by setting `num_classes=0`, allowing it to output high-dimensional feature embeddings through global average pooling. These embeddings capture semantic information from the input images without fine-tuning the pretrained parameters, ensuring computational efficiency and reducing overfitting risk.

D. Classifier Architecture

On top of the extracted visual embeddings, a lightweight Multi-Layer Perceptron (MLP) classifier was implemented to perform the final binary classification. The MLP architecture consisted of:

- A fully connected layer projecting concatenated feature vectors to a hidden dimension of 512
- Batch Normalization and ReLU activation to stabilize and accelerate convergence
- Dropout (0.5) for regularization
- A final linear layer mapping to two output neurons representing the two classes (fresh and stale)

The classifier was optimized independently, while the feature extractor remained frozen during training.

E. Model Training

The classifier was trained using the Adam optimizer with a learning rate of 0.001 and Cross-Entropy Loss as the objective function. The training process spanned 10 epochs with a batch size of 32. During each iteration, images were forwarded through the frozen feature extractor to generate embeddings, which were then input to the MLP for classification. The optimizer updated only the classifier parameters based on computed gradients.

To ensure reproducibility, all random seeds were fixed across Python, NumPy, and PyTorch modules. The device configuration automatically selected GPU (`cuda`) if available; otherwise, computation defaulted to CPU.

F. Model Evaluation

Performance was assessed on the held-out test set using several evaluation metrics:

- **ACC:** overall prediction correctness
- **P** and **R:** to quantify class-wise reliability and completeness
- **F1:** harmonic mean of precision and recall
- **SP:** ability to correctly identify fresh samples
- **ROC–AUC:** area under the Receiver Operating Characteristic curve
- **MCC:** balanced performance metric even for class-imbalanced data

G. Implementation Environment

All experiments were conducted on Google Colab with an NVIDIA GPU runtime. The implementation utilized the following key Python packages: `torch`, `torchvision`, `timm`, `scikit-learn`, `numpy`, and `PIL`. The entire workflow was executed under Python 3.10. The source code was designed for reproducibility, portability, and clarity to facilitate further extensions or integration with other pretrained architectures.

IV. EVALUATED RESULTS

The proposed model was evaluated on the “Fresh and Stale Classification” dataset using an 80–10–10 split for training, validation, and testing, respectively. Table I summarizes the epoch-wise performance across ten training epochs, reporting loss, accuracy, and F1-score for both training and validation phases.

As shown in Table I, the training and validation losses consistently decreased across epochs, demonstrating stable convergence and effective learning. Validation accuracy improved from 95.33% in the first epoch to a peak of 98.52% at epoch 9, while the corresponding F1-score reached 0.9859, indicating strong generalization capability. The marginal difference between training and validation metrics suggests that overfitting was well controlled due to appropriate regularization and data augmentation.

After completing ten epochs of training, the best-performing model was tested on the held-out test set. The comprehensive evaluation results are presented in Table II.

The high ROC–AUC score (0.9985) and F1-score (0.9808) indicate that the model is capable of distinguishing between *fresh* and *stale* samples with remarkable precision.

Moreover, the Matthews correlation coefficient (0.9601) reflects strong agreement between the predicted and actual classes, even under potential class imbalance.

Table. I
EPOCH-WISE PERFORMANCE OF THE PROPOSED MODEL

Epoch	Train Loss	Val Loss	Train Acc	Val Acc	Train F1	Val F1
1	0.2455	0.1124	0.8954	0.9533	0.9009	0.9542
2	0.1993	0.0718	0.9175	0.9738	0.9219	0.9749
3	0.1841	0.0606	0.9232	0.9795	0.9273	0.9805
4	0.1714	0.0651	0.9313	0.9742	0.9351	0.9759
5	0.1651	0.0590	0.9344	0.9764	0.9380	0.9774
6	0.1560	0.0499	0.9353	0.9852	0.9387	0.9860
7	0.1566	0.0590	0.9370	0.9772	0.9404	0.9782
8	0.1510	0.0514	0.9393	0.9810	0.9425	0.9819
9	0.1419	0.0438	0.9435	0.9852	0.9466	0.9859
10	0.1423	0.0469	0.9432	0.9821	0.9463	0.9830

Table. II
FINAL TEST METRICS OF THE PROPOSED MODEL

Metric	Value
Accuracy	0.9799
Precision	0.9948
Recall (Sensitivity)	0.9671
Specificity	0.9943
F1-score	0.9808
ROC–AUC Score	0.9985
Matthews Correlation Coefficient	0.9601

curve.png

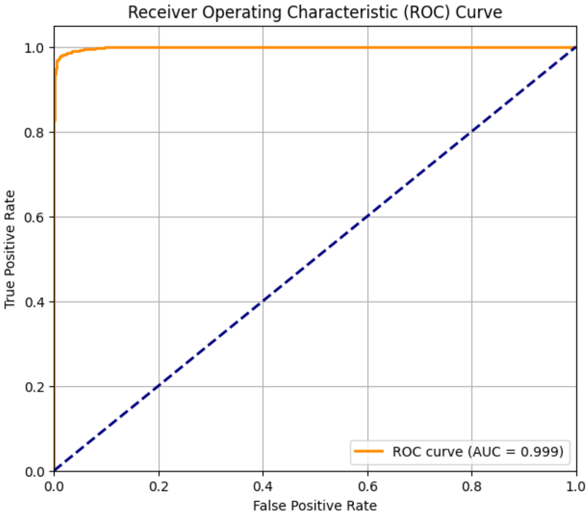

Fig. 1: Receiver Operating Characteristic (ROC) curve on the test set.

V. RESULT ANALYSIS

The experimental findings demonstrate that the proposed CLIP-based feature extraction combined with a lightweight multi-layer perceptron classifier achieved highly promising results on the Fresh and Stale Classification dataset. Throughout ten training epochs, both the training and validation metrics exhibited a consistent upward trend, confirming the model's stability and strong convergence behavior. The validation accuracy improved steadily from 95.33% in the first epoch to 98.52% by the ninth epoch, while the corresponding validation F1-score reached 0.9859, signifying excellent class-wise balance between precision and recall. The simultaneous decline in training and validation losses indicates that the model successfully minimized overfitting while learning meaningful representations from the data.

The final test evaluation further reinforces the model's robustness. With an overall accuracy of 97.99%, precision of 99.48%, and recall of 96.71%, the classifier proved highly reliable in identifying both fresh and stale samples. The ROC–AUC score of 0.9985 demonstrates outstanding discriminative capability, nearly reaching perfect separation between the two categories. Additionally, the Matthews correlation coefficient (0.9601) confirms a very strong correlation between predicted and actual labels, even in the presence of potential class imbalance.

A closer examination of the confusion matrix reveals that out of 2,634 test samples, only 53 misclassifications occurred—comprising 7 false positives and 46 false negatives—which corresponds to an error rate below 2%. This highlights the model's exceptional generalization ability and reliability in practical applications.

The observed results clearly validate the effectiveness of leveraging pretrained visual transformers (CLIP) as frozen feature extractors for domain-specific image classification tasks. By utilizing generalized visual embeddings learned from large-scale datasets, the model successfully transferred high-level semantic knowledge to a specialized food-quality classification problem. Furthermore, the lightweight MLP classifier ensured computational efficiency without sacrificing performance, making the proposed pipeline well-suited for real-time or resource-constrained environments.

In summary, the performance metrics collectively demonstrate that the proposed approach achieved state-of-the-art accuracy and robustness, confirming its potential as an efficient and scalable solution for automated freshness assessment. The strong balance across precision, recall, and F1-score also reflects the model's ability to make reliable decisions across both classes, ensuring practical viability for industrial and consumer applications.

VI. FUTURE WORKS

Although the proposed system achieved remarkable accuracy and robustness, several directions remain for future research. First, further improvements could be attained through multimodal integration, combining visual embeddings with chemical or spectral sensor data to enhance freshness prediction accuracy. Additionally, incorporating temporal analysis using video-based or time-series models may help capture gradual degradation patterns in perishable items.

Exploring fine-tuning strategies on domain-specific subsets of CLIP or other large vision–language models could improve adaptability to diverse food types. Moreover, implementing model quantization and pruning would facilitate deployment on low-power edge devices such as smartphones or embedded inspection systems. Finally, the system can be extended to multi-class scenarios to provide more granular insights for food safety monitoring and shelf-life prediction.

VII. CONCLUSION

This study introduced a novel and efficient approach for fresh and stale image classification using transfer learning with pre-trained CLIP visual embeddings and a simple yet effective MLP classifier. The experimental results demonstrated consistent performance improvements throughout training, achieving a final accuracy of 97.99%, F1-score of 0.9808, and ROC–AUC of 0.9985 on the test dataset. The results confirm that pre-trained transformer-based visual representations can generalize remarkably well to food-quality inspection tasks with minimal fine-tuning requirements.

The proposed model's high precision, recall, and robustness make it a viable candidate for practical real-world deployment in automated inspection, packaging, and food-safety assurance systems. In conclusion, this work underscores the potential of CLIP-based transfer learning to bridge the gap between large-scale vision-language models and domain-specific classification problems, providing a foundation for future innovations in intelligent food-quality monitoring.

REFERENCES

[1] Yue Yuan, Xianlong Chen, "Vegetable and fruit freshness detection based on deep features and principal component analysis," *ScienceDirect*, 2024. [Online]. Available: https://www.sciencedirect.com/science/article/pii/S2665927123002241

[2] Xinle Gao, Zhiyong Xiao, Zhaohong Deng, "High accuracy food image classification via vision transformer with data augmentation and feature augmentation," *ScienceDirect*, 2024. [Online]. Available: https://www.sciencedirect.com/science/article/abs/pii/S0260877423004314

[3] Kyung Jo, Seonmin Lee, Seul-Ki-Chan Jeong, Dae-Hyun Lee, Hayeon Jeon, Samooel Jung, "Hyperspectral imaging–based assessment of fresh meat quality: Progress and applications," *Microchemical Journal*, 2023, doi: 10.1016/j.microc.2023.109785. Available: https://www.sciencedirect.com/science/article/abs/pii/S0026265X23014042?via%3Dihub

[4] Minwoo Choi, Hye-Jin Kim, Azfar Ismail, Hyun-Jun Kim, Heesang Hong, Ghiseok Kim, Cheorun Jo, "Combination model for freshness prediction of pork using HSI and chemometrics," *Animal Bioscience*, 2024, doi: 10.5713/ab.24.0255. Available: https://www.animbiosci.org/journal/view.php?doi=10.5713/ab.24.0255

[5] Zhichen Lun, Xiaohong Wu, Jiajun Dong, Bin Wu, "Deep Learning-Enhanced Spectroscopic Technologies for Food Quality Assessment: Convergence and Emerging Frontiers," *PMC*, 2025. [Online]. Available: https://www.ncbi.nlm.nih.gov/pmc/articles/PMC12248972/

[6] Ekta Sonwani, Urvashi Bansal, Roobaea Alroobaea, Abdullah M. Baqasah, Mustapha Hedabou, "An Artificial Intelligence Approach Toward Food Spoilage Detection and Analysis," *Frontiers in Public Health*, 2022, doi: 10.3389/fpubh.2021.816226. Available: https://www.frontiersin.org/journals/public-health/articles/10.3389/fpubh.2021.816226/full

[7] Yuan Shu, Jipeng Zhang, Yihan Wang, Yangyang Wei, "Fruit Freshness Classification and Detection Based on ResNet-101 and Non-local Attention Mechanism," *PMC*, 2025. [Online]. Available: https://www.ncbi.nlm.nih.gov/pmc/articles/PMC12154944/

[8] Mehrad Nikzadfar, Mahdi Rashvand, Hongwei Zhang, Alex Shenfield, Francesco Genovese, Giuseppe Altieri, Attilio Matera, Iolanda Tornese, Sabina Laveglia, Giuliana Paterna, Carmela Lovallo, Orkhan Mammadov, Burcu Aykanat, Giovanni Carlo Di Renzo, "Hyperspectral Imaging Aiding Artificial Intelligence: A Reliable Approach for Food Qualification and Safety," *Applied Sciences*, 2024. [Online]. Available: https://www.mdpi.com/2076-3417/14/21/9821

[9] M Gatti, Anwar Ur Rehman, Ignazio Gallo, "A CLIP-Based Framework to Enhance Order Accuracy in Food Packaging," *Electronics*, 2025. [Online]. Available: https://www.mdpi.com/2079-9292/14/7/1420

[10] Saman Abdanan Mehdizadeh, Mohammad Noshad, Mahsa Chaharlangi, Yiannis Ampatzidis, "AI-driven non-destructive detection of meat freshness using a multi-indicator sensor array and smartphone technology," *ScienceDirect*, 2025. [Online]. Available: https://www.sciencedirect.com/science/article/pii/S2772375525000565

[11] L. A. Varga, J. Makowski, and A. Zell, "Measuring the Ripeness of Fruit with Hyperspectral Imaging and Deep Learning," *arXiv preprint*, 2021. [Online]. Available: https://arxiv.org/abs/2104.09808

[12] H Anwar, Talha Anwar, Shamas Murtaza, "Review on food quality assessment using machine learning and electronic nose system," *ScienceDirect*, 2023. doi: https://doi.org/10.1016/j.biosx.2023.100365. Available: https://www.sciencedirect.com/science/article/pii/S2590137023000626?via%3Dihub

[13] Alec Radford, Jong Wook Kim, Chris Hallacy, Aditya Ramesh, Gabriel Goh, Sandhini Agarwal, Girish Sastry, Amanda Askell, Pamela Mishkin, Jack Clark, Gretchen Krueger, Ilya Sutskever, "Learning Transferable Visual Models From Natural Language Supervision," *arXiv preprint*, 2021. [Online]. Available: https://arxiv.org/abs/2103.00020

[14] Alexey Dosovitskiy, Lucas Beyer, Alexander Kolesnikov, Dirk Weissenborn, Xiaohua Zhai, Thomas Unterthiner, Mostafa Dehghani, Matthias Minderer, Georg Heigold, Sylvain Gelly, Jakob Uszkoreit, Neil Houlsby, "An Image is Worth 16×16 Words: Transformers for Image Recognition at Scale," *ICLR*, 2021. [Online]. Available: https://arxiv.org/abs/2010.11929

[15] L. Bossard, M. Guillaumin, and L. Van Gool, "Food-101 – Mining Discriminative Components with Random Forests," *ECCV*, 2014. [Online]. Available: https://data.vision.ee.ethz.ch/cvl/datasets_extra/food-101/

[16] Tonmoy Ghosh, Edward Sazonov, "Improving Food Image Recognition with Noisy Vision Transformers," *arXiv preprint*, 2025. [Online]. Available: https://arxiv.org/pdf/2503.18997

[17] Detianjun Liu, Enguang Zuo, Dingding Wang, Liang He, Liujing Dong, Xinyao Lu, "Deep Learning in Food Image Recognition: A Comprehensive Review," *Applied Sciences*, 2025. [Online]. Available: https://www.mdpi.com/2076-3417/15/14/7626

VIII. BIOGRAPHY

Md. Siam Ansary has obtained Bachelor of Science in Computer Science and Engineering degree from Ahsanullah University of Science and Technology (AUST) of Dhaka, Bangladesh. Later, he completed Master in Information Technology from University of Dhaka. Currently, he is working as a fulltime faculty member at AUST.

Amina Brinto has completed Bachelor of Medicine and Bachelor of Surgery (MBBS) degree from Dhaka Community Medical College (DCMC) under University of Dhaka, Bangladesh. Later, she has cleared Fellowship of the College of Physicians and Surgeons (FCPS) - Part I under Bangladesh College of Physicians and Surgeons (BCPS). She is currently with Department of Obstetrics and Gynaecology, Kurmitola General Hospital, Dhaka.

Shaila Sajnin Keya has obtained Bachelor of Science degree in Nutrition and Food Science from University of Dhaka, Bangladesh. Later, she completed Masters of Science degree in Nutrition and Food Science from University of Dhaka.

Minimal Distortion Principle versus Back Projection for Independent Vector Analysis

Soufiane Tebache, Adel Belouchrani, Lynda Berrah and Nacira Mendjel

Abstract—This paper deals with the scaling ambiguity issue in blind convolutive source separation when performed in the frequency domain. It discusses the relationship between two major techniques, mainly the Minimal Distortion Principle and the Back Projection, that allow to overcome the aforementioned indeterminacy. The Minimal Distortion Principle minimizes the mean square difference between the separated sources and the sensor signals, while the back projection recovers the sensor-observed amplitudes of each estimated source signal. Herein, we prove that the Minimal Distortion Principle is a particular solution of the Back Projection. Another contribution of this paper consists of exploiting one of the most beneficial outcomes of the Back Projection, that is spatial diversity. Our proposed approach applies Single Input Multiple Output deconvolution to the outputs of the back projected source signals, after their estimation by the Independent Vector Analysis algorithm. This method has the advantage of improving the estimation accuracy and removing the channel effect. Experimental results show the effectiveness of our proposal with respect to both the Minimum Distortion Principle and the conventional Back Projection solution.

***Keywords*—Back projection, Minimal Distortion Principle, Independent Vector Analysis, SIMO Deconvolution.**

I. INTRODUCTION

Blind Source Separation (BSS) is a powerful tool for separating mixtures of sources from a set of sensors, where neither the source signals nor the mixing parameters are known. This problem leads to two types of indeterminacy: permutation and scaling. When dealing with wide-band propagation, as in the speech signal case, one faces the problem of convolutive mixtures. Existing solutions in the time domain lead to complex and time-consuming computations. Efficient methods solve the underling problem in the time-frequency domain using the Short-Time Fourier Transform (STFT). The latter transforms the convolutive BSS problem into several independent BSS problems with instantaneous models, which can be solved using well-established instantaneous BSS algorithms at each frequency bin. However, the estimated source signals in each frequency bin have arbitrary permutations and scaling that significantly affect the separation performance. Various post-processing [1, 2] can be used to address permutation ambiguity, but this increases computational cost. A more elegant solution is Independent Vector Analysis (IVA) [3], which uses the entire frequency spectrum as input, instead of considering each frequency bin as an independent BSS problem, to overcome the permutation ambiguity.

However, the scaling ambiguity remains and is equivalent to an arbitrary filter of the source signals in the case of the aforementioned approach. The Minimum Distortion Principle (MDP) [9] is a well-known method for dealing with such ambiguity, it selects the separators that minimizes the mean square difference between the separated source signals and the sensor signals. Another technique, called Back Projection (BP) [16], can recover the sources after separation to their sensor-observed amplitudes.

In this paper, we discuss the relationship between Minimal Distortion Principle (MDP) and Back Projection and prove that the MDP is a particular solution of the Back Projection. We observe that the Back Projection actually provides spatial diversity, which has not been exploited yet in the literature. Our second contribution consists of using Single Input Multiple Output (SIMO) deconvolution after separation. This is performed through IVA for each output signal in order to take advantage of the spatial diversity provided by the Back Projection. Such a proposal allows performance enhancement in terms of signal to distortion ratio with respect to reverberate time.

The paper is organized as follows: Section II. formulates the BSS problem briefly, the proposed solution and the proof of the MDP-BP relationship are provided in Section III., simulation results are presented in Section IV., and finally, Section V. concludes the paper.

II. PROBLEM FORMULATION

Let us observe, at time instant n, M signals, $\mathbf{x}(n) = [x_1(n), \cdots, x_M(n)]$, assumed to be the mixtures of L independent source signals $\mathbf{s}(n) = [s_1(n), \cdots, s_L(n)]$ according to the following noiseless convolutive model:

$$x_m(n) = \sum_{l=1}^{L} \sum_{p=0}^{P-1} a_{ml}(p) s_l(n-p) \quad m = 1, .., M \tag{1}$$

$$\mathbf{x}(n) = \sum_{p=0}^{P-1} \mathbf{A}(p)\mathbf{s}(n-p) \tag{2}$$

where $\mathbf{A}$(p), $p = 0, ..., P-1$, is the $M \times L$ transfer function matrix, whose elements are denoted $a_{ml}(p)$, and P is the impulse

Manuscript received October 8, 2025; revised November 7, 2025.

S. Tebache, A. Belouchrani, L. Berrah and N. Mendjel are with Ecole Nationale Polytechnique/LDCCP lab., Algiers, ALGERIA. (e-mail: soufiane.tebache@g.enp.edu.dz, adel.belouchrani@g.enp.edu.dz, lynda.berrah@g.enp.edu.dz, and nacira.mendjel@g.enp.edu.dz)

Digital Object Identifier (DOI): 10.53907/enpesj.v5i2.342

Part of this paper was presented in the conference paper [18].

response length. By assuming a significantly longer time analyzing window than the impulse response length, it is possible to express the convolution in the frequency domain as individual multiplications for each frequency bin, as follows:

$$\mathbf{x}_{TF}(f,n) = \mathbf{A}(f)\mathbf{s}_{TF}(f,n) \tag{3}$$

where $\mathbf{x}_{TF}(f,n)$ represents a column vector with M elements, denoted $x_{TF_m}(f,n)$, which corresponds to the $(f,n)^{th}$ element of the Short-Time Fourier Transform (STFT) [14], $\mathbf{X}_{TF_m}$, of the sensor signal $x_m(t)$, $\mathbf{s}_{TF}(f,n)$ denotes a column vector with L elements, denoted $s_{TF_l}(f,n)$, which corresponds to the $(f,n)^{th}$ element of the STFT, $\mathbf{S}_{TF_l}$, of the source signal $s_l(t)$. The matrix $\mathbf{A}(f)$ is an $M \times L$ mixing matrix for frequency bin f. In order to separate the source signals from the observed mixtures, an unmixing matrix $\mathbf{W}(f)$ should be estimated for each frequency bin:

$$\mathbf{y}_{TF}(f,n) = \mathbf{W}(f)\mathbf{x}_{TF}(f,n) \tag{4}$$

In the sequel, we assume that $M = L$ and that the $\mathbf{A}(f)$ matrices are well conditioned.

III. PROPOSED APPROACH

The proposed solution starts by applying the Independent Vector Analysis (IVA) [3] that solves implicitly the permutation ambiguity at the frequency bins, then addresses the scaling ambiguity through Back Projection and finally, recovers the source signal through a SIMO deconvolution algorithm. In subsection B., we discuss the relationship between Minimal Distortion Principle (MDP) and Back Projection, and show that the MDP is a particular solution of the Back Projection.

A. Independent Vector Analysis (IVA)

The IVA algorithm [3] considers the sources as multidimensional random vectors containing all the frequency components of each source signal. It aims to maximize the independence between individual source signals while maintaining the dependency within each vector. This process get rid of the permutation ambiguity between the frequency bins. The unmixing matrix is estimated at each frequency bin according to the following iterative update [11]:

$$\mathbf{W}(f) \leftarrow \mathbf{W}(f) + \eta\Delta\mathbf{W}(f) \tag{5}$$

With

$$\begin{aligned}
\Delta\mathbf{W}(f) &= \left\{\mathbf{I} + E\left[\boldsymbol{\varphi}^f(\mathbf{y}_{TF})\mathbf{y}_{TF}(f)^H\right]\right\}\mathbf{W}(f) \\
\mathbf{y}_{TF} &= [\mathbf{y}_{TF_1}, \ldots, \mathbf{y}_{TF_L}]^T \\
\boldsymbol{\varphi}^f(\mathbf{y}_{TF}) &= \left[\varphi_1^f(\mathbf{y}_{TF_1}), \ldots, \varphi_L^f(\mathbf{y}_{TF_L})\right]^T \\
\varphi_l^f(\mathbf{y}_{TF_l}) &= \frac{\partial}{\partial y_{TF_l}(f)} \log\left(p(\mathbf{y}_{TF_l})\right)
\end{aligned}$$

where the step size, $\eta \in [0,1]$, is a tuning parameter that imposes a trade-off between convergence speed and stability [11], and $p(.)$ is a density probability function.

B. Minimal Distortion Principle versus Back Projection

To deal with the scaling ambiguity in the frequency domain, two major techniques exist in the literature, mainly the Minimal Distortion Principle (MDP) [9] and the Back Projection (BP) [16]. The MDP chooses the proper separators that minimize the mean square difference between the separated sources and the sensor signals, its solution consists of the following unmixing matrix at frequency bin f:

$$\mathbf{W}_s(f) = diag(\mathbf{W}^{-1}(f))\mathbf{W}(f) \tag{6}$$

where $diag(.)$ denotes the diagonal matrix operator and $\mathbf{W}(f)$ is the unmixing matrix, at frequency bin f, estimated by the IVA algorithm.

The Back Projection technique projects back the estimated source signals to the sensor array, it actually rescales the source signals to match their observed amplitudes at each sensor:

Let $\hat{\boldsymbol{A}}(f) = \mathbf{W}^{-1}(f)$ be the estimated mixing matrix, the inverse of the estimated unmixing matrix, at the f^{th} frequency bin, and $y_{TF_l}(f,n)$, be the estimate of the l^{th} source signal $s_{TF_l}(f,n)$ at the time-frequency point (f,n). Because of the inherent scaling indeterminacy, we have the following relationships:

$$y_{TF_l}(f,n) = \alpha_l(f)s_{TF_l}(f,n) \tag{7}$$

$$\hat{\boldsymbol{a}}_l(f) = \frac{1}{\alpha_l(f)}\boldsymbol{a}_l(f) \tag{8}$$

where $\alpha_l(f)$ is an arbitrary factor. To get the signals, denoted $\underline{\mathbf{s}}_{TF_l}(f,n)$, free from the scaling indeterminacy, one can multiply the l^{th} separated signal $y_{TF_l}(f,n)$ by its corresponding column of the estimated mixing matrix $\hat{\boldsymbol{a}}_l(f)$:

$$\underline{\mathbf{s}}_{TF_l}(f,n) = \hat{\boldsymbol{a}}_l(f)y_{TF_l}(f,n) \tag{9}$$

By substituting equations (7) and (8) in equation (9), one gets:

$$\underline{\mathbf{s}}_{TF_l}(f,n) = \boldsymbol{a}_l(f)s_{TF_l}(f,n), l = 1, \cdots, L \tag{10}$$

where $\underline{\mathbf{s}}_{TF_l}(f,n) = [\underline{s}_{TF_{l_1}}(f,n), \ldots, \underline{s}_{TF_{l_M}}(f,n)]^T$ with $\underline{s}_{TF_{l_k}}(f,n)$ being the contribution of the l^{th} estimated source signal at the k^{th} sensor. It appears clearly from equation (10) that the recovered source signals at their sensor-observed amplitudes are free from the scaling ambiguity $\alpha_l(f)$. Note that equation (10) describes a Single Input Multiple Output (SIMO) system for each source, separately. Thanks to the multidimensionality of its output, such a system provides the spatial diversity needed to recover its input (in our case the corresponding source) using only second order statistics.

Let $\mathbf{W}(f)$ be an estimate of the unmixing matrix, at frequency bin f, of the blind convolutive separation problem. The scale indeterminacy free unmixing matrix of the Minimum Distortion Principle,

$$\mathbf{W}_s(f) = diag(\mathbf{W}^{-1}(f))\mathbf{W}(f)$$

is a particular solution of the Back Projection.

Using equation (9), the expression of the l^{th} signal recovered by Back Projection at the l^{th} sensor is given by:

$$\underline{s}_{TF_{l_l}}(f,n) = \hat{a}_{ll}(f)y_{TF_l}(f,n), l = 1, \cdots, L. \tag{11}$$

This can be obtained by dimension reduction at each frequency bin, e.g. by data whitening.

Consider the following source vector:

$$\underline{\mathbf{s}}_{TF}(f,n)=[\underline{s}_{TF_{1_1}}(f,n),\underline{s}_{TF_{2_2}}(f,n),...,\underline{s}_{TF_{L_L}}(f,n)]^T \tag{12}$$

Using equation (11), the source vector $\underline{\mathbf{s}}_{TF}(f,n)$ reads:

$$\underline{\mathbf{s}}_{TF}(f,n)=\begin{bmatrix}\hat{a}_{11}(f) & 0 & \dots & 0\\ 0 & \hat{a}_{22}(f) & \dots & 0\\ \vdots & \vdots & \ddots & \vdots\\ 0 & 0 & \dots & \hat{a}_{LL}(f)\end{bmatrix}\mathbf{y}_{TF}(f,n) \tag{13}$$

Note that

$$\begin{bmatrix}\hat{a}_{11}(f) & 0 & \dots & 0\\ 0 & \hat{a}_{22}(f) & \dots & 0\\ \vdots & \vdots & \ddots & \vdots\\ 0 & 0 & \dots & \hat{a}_{LL}(f)\end{bmatrix}=diag(\hat{\boldsymbol{A}}(f)) \tag{14}$$

where $\hat{\boldsymbol{A}}(f)$ is an estimate of the mixing matrix at frequency bin f, that is the inverse of the estimated unmixing matrix $\mathbf{W}(f)$:

$$\hat{\boldsymbol{A}}(f)=\mathbf{W}^{-1}(f) \tag{15}$$

According to equations (4), (14) and (15), equation (13) is rewritten as:

$$\begin{aligned}\underline{\mathbf{s}}_{TF}(f,n) &= diag(\mathbf{W}^{-1}(f))\mathbf{W}(f)\mathbf{x}_{TF}(f,n)\\ &= \mathbf{W}_s(f)\mathbf{x}_{TF}(f,n)\end{aligned} \tag{16}$$

with $\mathbf{W}_s(f)=diag(\mathbf{W}^{-1}(f))(\mathbf{W})(f)$, where one recognizes the MDP unmixing matrix (6).

This Theorem shows that the Minimum Distortion Principle is a particular solution of the Back Projection, in which only the $l-l^{th}$ components, $\underline{s}_{TF_{l_l}}(f,n), l=1,\cdots,L$ are used.

C. Back projection-Spatial diversity

In reference [17], the authors estimate the source signals as the back projected components onto the first sensor, i.e.

$$\underline{s}_{TF_{l_1}}(f,n), l=1,\cdots,L \tag{17}$$

The above expression does not exploit the spatial diversity offred by the source vectors $\underline{\mathbf{s}}_{TF_l}(f,n), l=1,\cdots,L$. Our contribution consists of exploiting this spatial diversity through Single Input Multiple Output (SIMO) deconvolution of the back projected output signal obtained after separation in the time-frequency domain by the IVA algorithm.

The source vectors of equation (9) obtained after the back projection of the IVA algorithm outputs in the time-frequency domain are transformed to the time domain through the Inverse Short Time Fourier Transform (ISTFT):

$$\underline{s}_{l_k}(n)=ISTFT(\underline{s}_{TF_{l_k}}(f,n)), k,l=1,\cdots,L \tag{18}$$

According to equation (10), one has:

$$\underline{s}_{l_k}(n)=ISTFT(a_{l_k}(f)s_{TF_l}(f,n)), \tag{19}$$

Since we have assumed a significantly longer analyzing window than the impulse response, the multiplications in the frequency domain are translated to linear convolutions in the time domain. Hence, we obtain L SIMO systems:

$$\underline{s}_{l_k}(n)=\sum_{p=0}^{P-1}a_{l,k}(p)s_l(n-p), k,l=1,\cdots,L \tag{20}$$

The Robust Normalized Multichannel Frequency-Domain Least-Mean-Square algorithm [15] and the SIMO equalizer reported in [8] are employed in this paper for performing the blind identification of the L SIMO channels $a_{l,k}(p), p=0,\cdots,P-1; k,l=1,\cdots,L$, and their equalization to retrieve the L original sources $s_l(n), l=1,\cdots,L$, respectively.

IV. NUMERICAL EXPERIMENTS

Herein, an evaluation is conducted in the case of speech signals.

A. Experimental setup

Pyroomacoustics software package [19] is used to generate the Room Impulse Responses (RIRs) and the corresponding convolutive mixtures according to a simulation scenario: A room measuring $5.5\ m\times 3.5\ m\times 3\ m$ with RT60 reverberation time of $130\ ms$ was chosen, and an array of seven microphones was placed in the center of the room, with one microphone in the center and the other six spaced equally around a circle of a $4.5\ cm$ radius. Two sources were positioned at different angles $0.5\ m$ away from the microphone array, and mixtures were produced using $10\ s$ speaking utterances at a sampling frequency of $16\ kHz$. Figure 1 shows the simulation scenario and the position of the two sources.

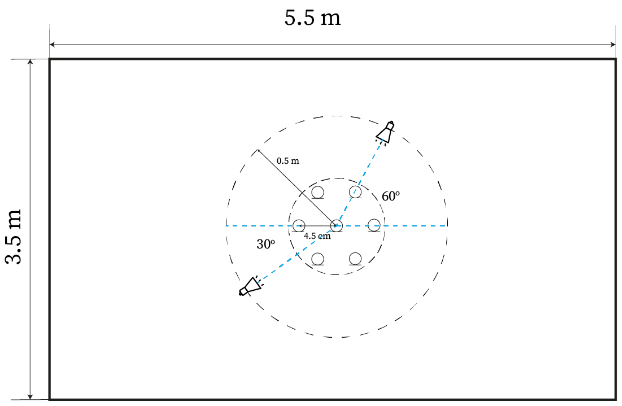

Fig. 1: Simulation scenario with 2 sources.

B. Performance evaluation

To assess the quality of the separation, we compute the standard energy ratios in decibels (dB), specifically the Signal-to-Distortion (SDR) for the l^{th} source as:

$$SDR_l=10\log_{10}\frac{||s_l||^2}{||s_l-\hat{s}_l||^2} \tag{21}$$

where $||.||$ denotes the Euclidean norm.

RT60 reverberation time is the duration required for the sound energy in a room to decrease by 60 dB after the source emission has stopped (ISO 3382).

Herein, one evaluates the robustness of the proposed IVA-based algorithm versus RT60 reverberation time using MDP [9], BP [17] and our proposal BP-SIMO, respectively. The SDRs of the two sources are computed for different RT60s ranging from 150 ms to 450 ms. Figures 2 and 3 depict the evolution of the BSS performance (SDR) of the first and second separated signal, respectively, as the RT60 increases.

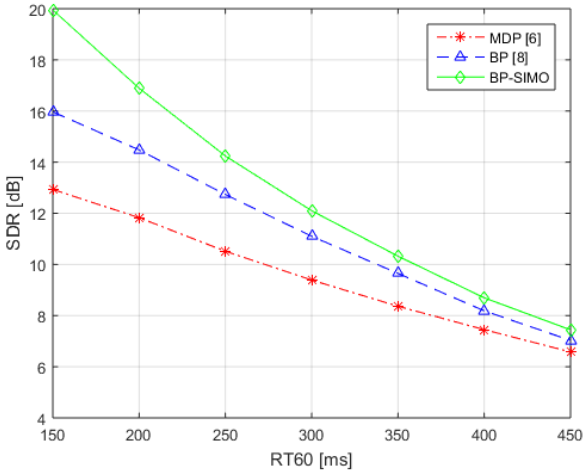

Fig. 2: Effect of reverberation on the SDR of the first separated signal.

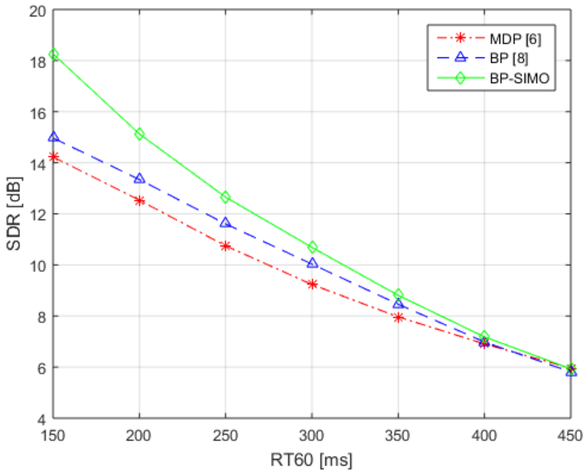

Fig. 3: Effect of reverberation on the SDR of the second separated signal.

The above graphs show that an increase in RT60 reverberate time leads to a gradual degradation of performance. This degradation occurs because sound waves in a reverberate room bounce off surfaces and create multiple reflections that can overlap with the direct sound, making it difficult for BSS algorithms to accurately distinguish between individual sources. The results highlight, as well, that our BP-SIMO approach outperforms the BP [17] and MDP [9] methods for all RT60 values.

V. CONCLUSION

New insights on the scaling ambiguity problem involved in Independent Vector Analysis is given. The relationship between the Minimal Distortion Principle and Back Projection for solving the aforementioned ambiguity is discussed. The paper shows that the Minimal Distortion Principle is actually a particular solution of the Back Projection. A second contribution consisted of exploiting, through SIMO deconvolution, the spatial diversity provided by the Back Projection. Herein, the SIMO deconvolution has been performed using the Robust Normalized Multichannel Frequency-Domain Least-Mean-Square algorithm [15] for the channel blind identification and the SIMO equalizer reported in [8] for the channel equalization. Performance results, in terms of signal to distortion ratio, confirm that the proposed approach enhances the quality of source separation, with respect to reverberate time, as applied to speech signals.

REFERENCES

[1] Leandro E. and Diego H. Milone, "Using multiple frequency bins for stabilization of FD-ICA algorithms, Signal Processing, vol. 119, pp. 162-168, 2016.

[2] Yatabe, K., "Consistent ICA : Determined BSS Meets Spectrogram Consistency", IEEE Signal Processing Letters, vol. 27, 2020.

[3] Kim, T. and Lee, I. and Lee, T.-W., "Independent vector analysis: definition and algorithms", 2006 Fortieth Asilomar Conference on Signals, Systems and Computers, pp. 1393–1396, 2006.

[4] Herault, J. and Jutten, C., "Space or Time Adaptive Signal Processing by Neural Network Models, American Institute of Physics Inc., pp. 206–211, 1986

[5] Comon, P., "Independent component analysis, A new concept?", Signal Processing, vol. 36, no. 3, pp. 287-314, 1994.

[6] Comon, P., "Workshop on Higher-Order Spectral Analysis", Separation Of Stochastic Processes, 1989.

[7] Even, J. and Saruwatari, H. and Shikano, K., "Enhanced wiener post-processing based on partial projection back of the blind signal separation noise estimate", 17th European Signal Processing Conference, 2009.

[8] Miyoshi, M. and Kaneda, Y., "Inverse filtering of room acoustics", IEEE Transactions on acoustics, speech, and signal processing, vol. 36, no. 2, pp. 145-152, 1988.

[9] Matsuoka, K., "Minimal distortion principle for blind source separation", Proceedings of the 41st SICE Annual Conference. SICE 2002., vol. 4, pp. 2138–2143, 2002.

[10] Scheibler, R., "Generalized Minimal Distortion Principle for Blind Source Separation", in Proc. Interspeech, Shanghai, China, 2020

[11] Kim, T. and Attias, H.-T. and Lee, S.-Y. and Lee, T.-W., "Blind source separation exploiting higher-order frequency dependencies", IEEE transactions on audio, speech, and language processing, vol. 15, no. 1, pp. 70-79, 2007.

[12] Huang, Yiteng and Benesty, Jacob, "Adaptive blind channel identification: multi-channel least mean square and Newton algorithms", Signal Processing, vol. 82, pp. 1127-1138, 2002.

[13] Xu, Guanghan and Liu, Hui and Tong, Lang and Kailath, Thomas, "A least-squares approach to blind channel identification", IEEE Transactions on signal processing, vol. 43, no. 12, pp. 2982-2993, 1995.

[14] Oppenheim, A. V., "Speech spectrograms using the fast Fourier transform, IEEE Spectrum, vol. 7, no. 8, pp. 57-62, 1970.

[15] Haque, M. A. and Hasan, M. K., "Noise robust multichannel frequency-domain LMS algorithms for blind channel identification", IEEE Signal Processing Letters, vol. 15, pp. 305-308, 2008.

[16] Murata, N. and Ikeda, S. and Ziehe, A., "An approach to blind source separation based on temporal structure of speech signals", Neurocomputing, vol. 41, pp. 1-24, 2001.

[17] Nakashima, T. and Ono, N., "Inverse-free Online Independent Vector Analysis with Flexible Iterative Source Steering", 2022 Asia-Pacific Signal and Information Processing Association Annual Summit and Conference (APSIPA ASC), 2022.

[18] Belouchrani, A. and Mendjel, N. and Berrah, L. and Tebache, S., "Independent Vector Analysis Based MIMO Deconvolution: Exploiting Spatial Diversity Through Back Projection", 22nd IEEE Statistical Signal Processing Workshop, Hanoi, Vietnam, 2-5 July 2023.

[19] Scheibler, R. and Bezzam, E. and Dokmanić, I., "Pyroomacoustics: A python package for audio room simulation and array processing algorithms2, 2018 IEEE international conference on acoustics, speech and signal processing (ICASSP), 2018.

[20] Emmanuel Vincent, "BSS Eval Toolbox Version 3.0 for Matlab", 2007.

[21] Hiroe, Atsuo, "Solution of permutation problem in frequency domain ICA using multivariate probability density functions", 6th International Conference, ICA 2006, Charleston, SC, USA, March 5-8, 2006.

[22] Liu, A. and Song, G. and Lee, S. and Fu, X. and Chen, X., A State-dependent IVA Model for Muscle Artifacts Removal from EEG Recordings, IEEE Transactions on Instrumentation and Measurement, vol. 70, 2021.

[23] Belouchrani, A. and Cichock, A., "Robust whitening procedure in blind source separation context2, IEE Electronics Letters, vol. 36, no. 24, 2000.

A New Multi-Path Hybrid Classifier for Transformer Oil Fault Diagnostic

Youcef Benmahamed, Omar Kherif, Sofiane Chiheb, Madjid Teguar, Sherif Ghoneim and Ahmed Boubakeur

Abstract—This work aims to provide advances in diagnosis algorithms using intelligent techniques and represents an application in fault detection and classification in oil-immersed power transformers. The paper proposes a new methodology of classification using hybrid algorithms to describe an improved DGA diagnostic tool based on combining different classifiers and several input vectors. A total of six classes of electrical and thermal faults are labeled. For each fault, binary classifications are first conducted using two classifiers trained and evaluated using nine different input vectors. For this, a dataset of 501 samples is used, and the best pairs (classifier, input vector) are selected for each given binary classification. From these pairs, different hybrid classifiers are proposed. Each classifier reaches its outcome through an independent pathway, and these classifiers together form the proposed multi-path hybrid classifier. The final decision of this classifier is obtained from the decisions made at the output of each path. This application brings a global accuracy rate of up to 95% for the transformer oil diagnosis, demonstrating the proposed technique's effectiveness in the classification field. The proposed model and other conventional algorithms are compared using a small independent database of twenty elements..

***Keywords*—DGA, fault diagnosis, power transformer oil, hybrid classifier, SVM, KNN, Decision Tree.**

NOMENCLATURE

DGA	Dissolved Gas Analysis.
KNN	K-Nearest Neighbor.
SVM	Support Vector Machine.
DT	Decision Tree.

I. INTRODUCTION

The continuous and reliable operation of electricity is one of the main challenges of power companies, from generation to transmission and distribution. In this chain, power transformers play an essential role for the target. Numerous studies were conducted to investigate the impact of faults in power transformers as well as to develop and/or improve resolution techniques to prevent such faults (e.g., [1–4]). Studying more than 340 power transformers with a voltage rate from 33 to 400 kV, authors in [5] stated that insulation problems are the most common fault, accounting for 37% of power transformer failures.

Mineral insulating oil is the most common oil used in outdoor transformers. This oil is characterized by its significant dielectric strength to withstand a fairly high voltage. It also helps to reduce heat generated by transformer windings. Indeed, oil-immersed transformers' lifetime can be governed by the state of the insulation system. This latter is generally exposed to some defects arising from overheating, paper carbonization, arcing, and discharges of low or high energy [4, 6, 7]. Evaluation procedures and relevant tests of these oils can be found within the recommendations of [8, 9].

Dissolved Gas Analysis (DGA) method is one of the most effective methods used in the field of faults detection within oil-immersed power transformers [10, 11]. This method analyzes the concentration of gases liberated in the transformer oil. Different hydrocarbon gases are released due to insulating oil and paper decomposition under electrical and thermal stresses.

In general, the most important gases, in alphabetical order, are Acetylene (C_2H_2), Ethane (C_2H_6), Ethylene (C_2H_4), Hydrogen (H_2), and Methane (CH_4). A particular combination of gases characterizes each type of fault within transformer oil.

Some of the application of DGA methods can be summarized as follows; i) DGA identifies different transformer fault types, due to different thermal, electrical, and mechanical stresses on the insulating oil. Each fault produces a specific pattern of gases that can be detected through DGA. ii) DGA detects faults early before leading damage to the transformer, so it helps prevent costly repairs and downtime. iii) Monitoring changes in gas levels over time provides a trend analysis that helps predict future faults and plan maintenance activities accordingly. iv) it provides an overall assessment of the transformer's condition through analyzing various gases and their levels, which helps in determining whether the transformer is operating within normal limits or needs maintenance. v) it also helps to locate the fault within the transformer by analyzing the distribution of gases within different parts of the transformer. So, it is a powerful tool for transformer fault diagnosis [12, 13].

Manuscript received September 28, 2024; revised November 8, 2025.

Y. BENMAHAMED, M. TEGUAR and A. BOUBAKEUR are with Laboratoire de Recherche en Electrotechnique (LRE), Ecole Nationale Polytechnique (ENP), 10 Rue des Frères OUDEK, El Harrach 16200, Algiers, Algeria. (e-mail: youcef.benmahamed@g.enp.edu.dz, madjid.teguar@g.enp.edu.dz, and ahmed.boubakeur@g.enp.edu.dz),

O. KHERIF is with Advanced High Voltage Research Centre, Cardiff University, Cardiff CF24 3AA, UK. (e-mail: KherifO@cardiff.ac.uk).

S. CHIHEB is with National Higher School of Technology and Engineering, Laboratoire de Technologies des Systems Energétiques, 23005, Annaba, Algeria (s.chiheb@ensti-annaba.dz)

S. GHONEIM is with Electrical Engineering Department, College of Engineering, Taif University, P. O. Box 11099, Taif 21944, Saudi Arabia. (e-mail: s.ghoneim@tu.edu.sa).

Digital Object Identifier (DOI): 10.53907/enpesj.v5i2.286

The dissolved gases produce under the electrical, thermal, and mechanical stresses. For instance, Ethylene is related to hotspots between 150 C and 1000 C, and acetylene is associated with arcs where temperatures reach a few thousand degrees. Furthermore, partial discharges in transformer oil can result in a considerable increase in hydrogen concentration because of the ionic bombardment [13]. Six classes of faults are widely considered in this field, namely partial discharge (PD), low energy discharges (D1), high energy discharges (D2), thermal faults < 300 C (T1), thermal faults of 300 C to 700 C (T2), and thermal faults > 700 C (T3).

The literature surveys indicated some shortcomings of using DGA for transformer fault diagnosis. In some cases, the dissolved gases amount is not sufficient to refer the exact transformer fault type and it can produce false positives, where the normal aging or environmental factors increase the gas levels producing false results [15]. The nonlinearity of the data samples can also lead to incorrect of transformer fault type. DGA Data sample processes consume time, effort and cost [16]. The accuracy of DGA results influences by other factors such as the quality of the oil sample, the sampling technique used, and the laboratory analysis method [17]. Due to wrong diagnosis of the specific transformer fault types, it is difficult to determine the appropriate maintenance or repair actions [18]. Interpreting DGA results requires specialized knowledge and expertise, which may not be readily available to all users [19].

In literature, different techniques have been developed to diagnose transformer faults. These techniques include graphical DGA methods (e.g., [20, 21]) and intelligent techniques (e.g., [22–24]). In addition, improved techniques (coupled methods) have also been created to accurately diagnose transformer faults (single and/or multiple faults) and indicate each fault's likelihood quantitatively (e.g., [23–26]). Arranging the input data of the DGA methods can affect on the DGA results. Therefore, many researchers have focused on developing input vectors that can enhance the DGA results to diagnose transformer faults correctly [4, 7, 27, 28].

This work describes an advanced classification methodology using a combination of different input vectors and various classifiers, and an application is presented to enhance the transformer fault diagnostic accuracy based on DGA. Furthermore, hybrid algorithms are proposed to improve DGA diagnostic tools. From a total dataset of 501 samples, 481 are used to train and test the proposed models, where six electrical and thermal fault classes are labeled. As main result, it was found that the global accuracy rate, reaching 95% for the power transformer diagnosis, demonstrates the effectiveness of the proposed technique.

The paper is organized as follows: the proposed methodology is presented in a Section to provide a general overview and a reference point for different applications. Section III covers the selected classifiers and input vectors for the transformer oil fault diagnosis. The dataset is also presented in this section. Results and discussions are shown in Section IV. The results obtained and compared with other classifiers are shown at the end of this section. The paper finalizes with conclusions and perspectives.

II. PROPOSED MULTI-PATH HYBRID CLASSIFIER

A. *Geeral principal*

In [27], the authors proposed several input vectors to train and assess a KNN classification algorithm based on a decision tree principle. The work was conducted to select the best input vector to achieve a high-accuracy diagnosis for the transformer faults. The accuracy rate has been analyzed to choose the most appropriate input vector for the proposed method. The obtained results were fascinating compared to conventional techniques of classification. Therefore, the idea is generalized in this work and introduces a new technique. This technique uses multiple classifiers, and the final decision is determined by an election (e.g., high number of appearances). Figure 1 shows the chart of the proposed technique.

The first step involves selecting an M number of different classifiers according to the desired application. The parameters associated with each classifier should be defined and adjusted for the application. Then, a set of criteria should be established to define the best pair's characterization. For instance, the simplest criterion represents the pair with the highest accuracy rate or an accuracy rate higher than a given value. Finally, a K number of criteria should be selected, and this number will affect the number of paths in the proposed multi-path hybrid classifier.

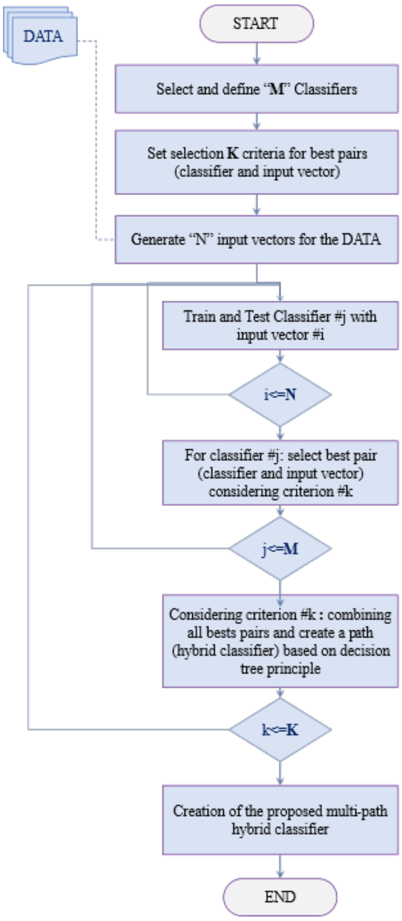

Fig. 1: A general structure of the proposed methodology.

As shown in Figure 1, the next step consists of generating different input vectors from the same dataset. The collected data generates various modified datasets, grouping the M input vectors. Taking into account the transformer oil fault diagnosis, for instance, the original data represents the first input vector, which consists of the concentration of gases in parts per million (ppm). A second input vector may be the relative concentration of each gas compared to the sum of concentrations. It should be noted that the input vector generation is a process that depends on the data where the data transformation should be established to make the data more separable and easier to use in the classification process. A detailed example of the selected input vectors is presented in Section III.

It is important to note that the selected combinations together help with the identification of various possible pathways. Therefore, the combination of these pathways represents the proposed multi-path hybrid classifier where the final decision is obtained from pre-defined criteria as shown in the forthcoming parts.

B. Pairs and paths selection

Each classifier is trained and evaluated by all the selected input vectors using the dataset defined for the testing process. Several techniques can be adopted for this phase, such as a binary classification based on the decision tree principle and multicategory classification. Figure 2 shows two possible scenarios for the classification process.

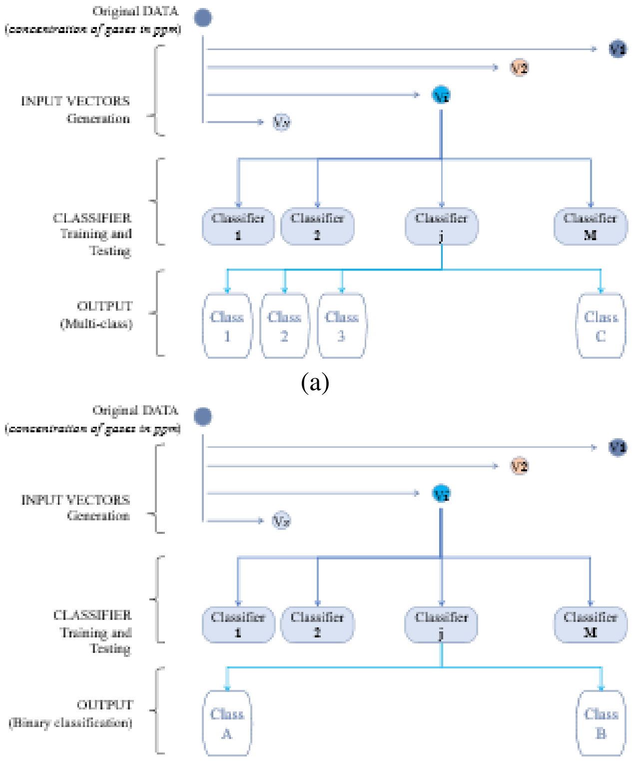

(a)

(b)

Fig. 2: Best combination identification process:(a) Multiclass condition,(b) Binary condition.

A decision tree principle can be considered in both scenarios, representing a branched flowchart with two or multiple pathways for potential decisions. For a given classifier, the tree starts with a decision node, which implies a decision must be made. For the multiclass scenario in Figure 2(a), a branch is created from the decision node where the obtained decision might successively run to another decision. For the second scenario, the process is simple by applying a "one vs. all" strategy. This means that each dataset is used to train and evaluate a given classifier about two classes of faults denoted by Class 1 and Class 2 as shown in Figure 2(b).

As an application in transformer oil diagnosis, for instance, Class 1 (=Fi) might be used to refer to one of the six faults in transformer oil (i.e., PD, D1, D2, T1, T2, and T3). In this case, Class 2 (=Xi) should represent a complementary class depending on the classification (i.e., Xi = PD, D1, D2, T1, T2, and T3 – Fi). A binary classification is considered by selecting this process, which means two decisions can be obtained on the output of each classifier. It will help identify the appropriate input vector and classifier for binary classification. Figure 3 demonstrates the proposed process to determine the best combination vector-classifier to create paths for the global hybrid classifier.

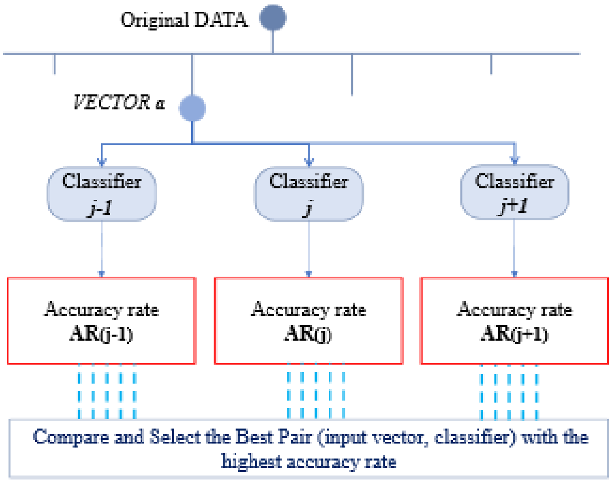

Fig. 3: Best pair selection process.

Figure 3 shows that the training and testing processes are conducted using input vectors applied to various classifiers. Indeed, many tests should be conducted so that the accuracy rate of each binary classification can be obtained as a function of the selected classifier and input vector. Therefore, this process helps identify the possible paths for global classification. Figure 4 illustrates a typical structure of the proposed technique used to determine the global accuracy rate of any path.

The best pairs selection process allows the creation of a hybrid classifier with one possible decision. This hybrid classifier, the denoted path, is not unique; different proposals can be made according to the desired accuracy rate. Eventually, each pathway reaches an outcome by passing through different classifiers and elaborating various input vectors. A combination of these decisions offers a trusted outcome that is generated from the result of the selected pathways, especially once the same outcome is obtained for different paths.

It is worth noting that the proposed multi-path hybrid classifier can be used in various classification problems, including multi-input multi-output classification (MIMO-C) systems. In addition, different scenarios can be generated from the proposed structure according to the output classes for a given situation.

III. INPUT VECTOR AND CLASSIFIER

In this work, nine input vectors have been used to train and test different classifiers, where the best combination (classifier and

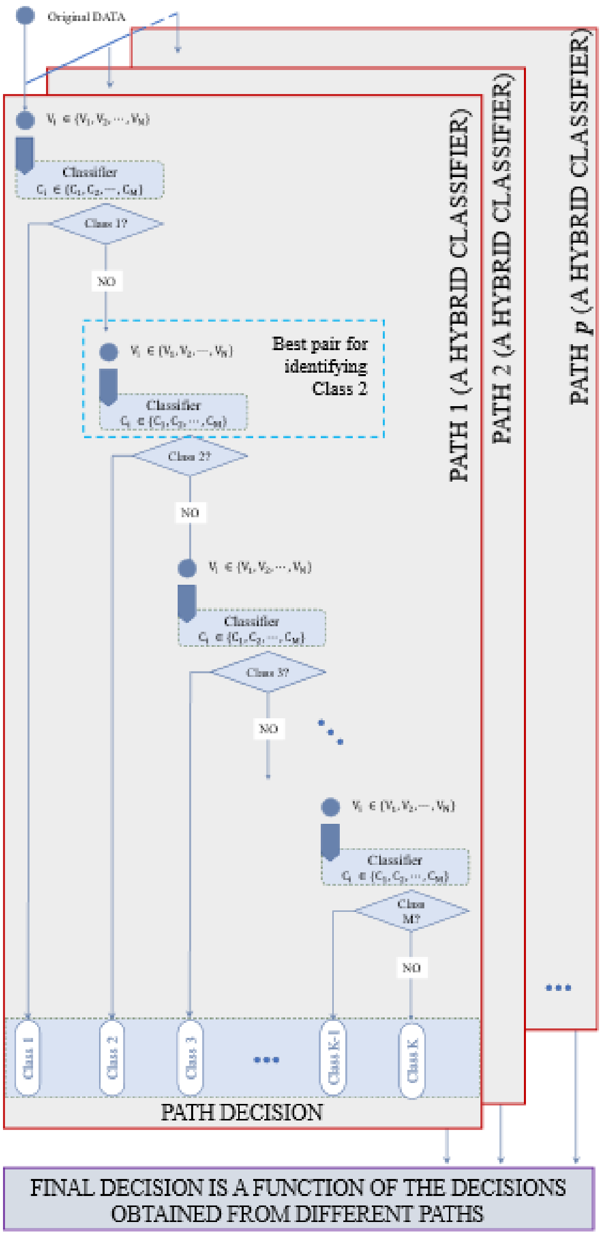

Fig. 4: General structure of the proposed classifier.

input vector) is selected for the considered binary classification. Indeed, pre-classification is first adopted to recognize the first three best combinations (input vector and classifier) that gives the highest accuracy rate where a database of 501 whose 481 samples were reserved the process of training and testing. Table I gives the distribution of the training and testing samples according to their identified fault type. Additional twenty samples (shown in Section IV.) have been used to examine the validity of the proposed classifier.

As the Authors in [18] detailed, the 481 samples were collected from different sources where gas concentration values were observed in service for faulty equipment inspected in service. The database is mainly collected from relevant publications (e.g., [29]) and Egyptian Electric Utility (Report [30]). Data are collected from [31] and [32] for the twenty samples used for validation.

A holdout method is used for the dataset decomposition based on the well-known decomposition (2/3 for training and 1/3 for testing). Although the dataset is unbalanced, the authors randomly assign sample sets for each class by 2/3 in the training phase, and by 1/3 in the testing phase. In this way, one can ensure that the existence of each class in the training and testing processes – proportionally by its initial dimension. This scenario helps with the reduction of the potential risk of each classifier. Therefore, 321 samples have been randomly selected for the training phase and 160 samples for the testing. Among other data mining methods, three classifiers have been considered as follows:

Table. I
DISTRIBUTION OF SAMPLES OVER FAULT TYPES

Symbol	Training	Testing	Total
PD	32	16	48
D1	53	26	79
D2	84	42	126
T1	63	32	95
T2	32	16	48
T3	57	28	85
Total	321	160	481

- Support Vector Machine (SVM)
- K-Nearest Neighbor (KNN)
- Decision tree (DT)

As mentioned previously, a binary classification has been independently developed for all of the classifiers. In order to simplify the comparison process and avoid going inside the algorithms, MATLAB toolboxes have been used for the application. These toolboxes are exploited to use the SVM, KNN, NB, DT classifiers. Details of each are available online on [33–35].

It is well-known that many interpretative methods based on DGA were reported to detect the incipient fault nature within an oil-immersed power transformer. These mainly include, as input vectors, the concentration of the dissolved gases in ppm, relative concentration of gases in percentage, IEC ratios, Rogers four-ratios, Dornenburg ratios, Duval triangle coordinates, Duval pentagon coordinates, a combination of Rogers and Dornenburg ratios, and a combination of Duval triangle-pentagon coordinates as follows:

V1 Concentrations of the gases in parts per million
V2 Percentage to the total sum
V3 IEC ratios
V4 Rogers four-ratios
V5 Dornenburg ratios
V6 Duval triangle coordinates
V7 Duval pentagon coordinates
V8 Rogers and Dornenburg ratios
V9 Duval triangle-pentagon coordinates

It should be noted that more details about these input vectors and their formulation are reported in a previous work [25].

Table. II

CLASSIFICATION RESULTS FOR TWO DIFFERENT CLASSIFIERS FOR 10 SAMPLES OF PD CLASS

SAMPLE	ACTUAL CLASS	PREDICTED CLASS																	
		KNN									SVM								
		V1	V2	V3	V4	V5	V6	V7	V8	V9	V1	V2	V3	V4	V5	V6	V7	V8	V9
PD-1	PD	PD	PD	PD	D1	PD	PD	PD	PD	PD	PD	PD	D2	PD	PD	D1	PD	D2	PD
PD-2	PD	PD	PD	PD	PD	PD	T3	PD	T1	PD	PD	PD	PD	PD	T1	D1	PD	PD	PD
PD-3	PD	PD	PD	PD	PD	PD	T3	PD	PD	PD	PD	PD	PD	PD	PD	T3	PD	D2	PD
PD-4	PD	PD	PD	PD	T1	PD	T1	PD	T1	PD	PD	PD	PD	PD	T3	PD	T3	T2	PD
PD-5	PD	PD	PD	PD	PD	PD	PD	PD	T3	PD	PD	PD	D2	PD	PD	D1	PD	D2	PD
PD-6	PD	PD	PD	PD	PD	T1	T3	PD	T1	PD	PD	PD	PD	PD	PD	D1	PD	D2	PD
PD-7	PD	PD	PD	D1	PD	PD	T3	PD	PD	PD	PD	PD	PD	PD	PD	T3	PD	D2	PD
PD-8	PD	PD	PD	PD	PD	PD	T3	PD	T1	PD	PD	PD	PD	PD	T2	T3	PD	PD	PD
PD-9	PD	PD	PD	PD	PD	PD	T3	PD	T1	PD	PD	PD	PD	PD	PD	T1	PD	D2	PD
PD-10	PD	PD	PD	T1	PD	PD	T2	PD	D2	PD	T1	T1	PD	PD	T3	T3	T3	T1	PD

Table. III

CLASSIFICATION RESULTS FOR TWO DIFFERENT CLASSIFIERS FOR 10 SAMPLES OF D2 CLASS

SAMPLE	ACTUAL CLASS	PREDICTED CLASS																	
		KNN									SVM								
		V1	V2	V3	V4	V5	V6	V7	V8	V9	V1	V2	V3	V4	V5	V6	V7	V8	V9
D2-1	D2	D2	D2	D2	D2	D2	D2	D2	D2	D2	D1	D2	D2	D2	D2	T1	D2	D2	D2
D2-2	D2	D2	D2	D2	D2	D2	D2	D2	D2	D2	D2	D2	D2	D2	D2	T3	D2	D2	D2
D2-3	D2	D2	D2	D2	D2	D2	D2	D2	D2	D2	D2	D2	D2	D2	D2	T3	D2	D2	D2
D2-4	D2	D2	D2	D2	D2	D2	D2	D2	D2	D2	D1	D2	D2	D2	D2	D2	D2	D2	D2
D2-5	D2	D2	D2	D2	D2	PD	D2	D2	T1	D2	D2	D2	D2	D2	D2	D2	D2	D2	T1
D2-6	D2	D2	D2	D2	D2	D2	D2	D2	D2	D2	D1	D2	D2	D2	D2	T3	T2	D2	D2
D2-7	D2	D2	D2	D2	D2	D2	D2	D2	D2	D2	D1	D2	D2	D2	D2	T3	T2	D2	D2
D2-8	D2	D2	D2	D2	D2	D2	D2	D2	D2	D2	D1	D2	D2	D2	D2	T1	D2	D2	D2
D2-9	D2	D2	D2	D2	D2	PD	D2	D2	PD	D2	D2	D2	D2	D2	D2	T1	D2	D2	D2
D2-10	D2	D2	D2	D2	D2	D2	D2	D2	D2	D2	D2	D2	D2	D2	D2	D2	D2	D2	D2

IV. RESULTS AND DISCUSSIONS

This section provides the obtained results when applying the proposed classification methodology. A binary classification is presented, and the corresponding results are discussed to identify the hybrid classifiers. Secondly, an example of a multipath hybrid classifier is presented and discussed. Finally, the obtained results along with a comparison with other classifiers are shown.

A. Binary classification and pair selection

The proposed methodology's first step is finding the best pairs (classifier, input vector) from each binary classification. A set of 481 samples has been used for the training and testing stages, two-thirds of the samples were reserved for training phase and one-third for testing utilizing the MATLAB' functions. Table II illustrates a brief description and example of the binary classification results using two different classifiers (KNN and SVM) and considering the nine input vectors (V1 to V9). The classification results in this table consider only the PD class of faults where ten samples are selected arbitrary to examine the existence of best pairs.

From the results obtained, one can clearly see that the classifier selection and the input vector are key factors in the classification purpose. For the same classifier, different decisions are obtained when considering different input vectors. The correct decision is obtained from both classifiers when using the input vector V9. Vectors V1 and V2 allow obtaining 100% accuracy with KNN against 90% with the SVM classifier.

Likewise, one can see that vector V4 is effective with SVM classifier since all obtained decisions are correct, which is not the case when considering the KNN classifier. Regarding correct decisions, the KNN classifier shows a ratio of 70/90 against 63/90 for the SVM classifier. It can be explained by the fact that the KNN classifier is more suitable for such a classification than the SVM and the selected input vectors.

Overall, the results can be summarized in the fact that the pair (classier, input vector) considerably impact the obtained decision of a classification. In order to examine such conclusions, different samples are considered where the same analysis is conducted. Table III gives the obtained results using the two classifiers and considering the nine input vectors for D2 faults.

Compared to the results in Table II, the decisions for the second classification in Table III show a higher accuracy rate when using the D2 fault. It may imply that conclusions on a specific pair (classifier, input vector) applied to a given class of faults cannot be generalized to other classes. For instance, input vector V6 with KNN classifier gives an accuracy rate of 100% for D2 classification against 20% for PD one.

Regarding the SVM classifier, one can see from Tables II and III that input vector V8 is suitable for distinguishing D2 from the PD fault. Therefore, each classification should be associated with one or more pairs (classifier, input vector) to provide a high accuracy classification decision. The testing data consists of 160 samples, which all group the six defined classes of faults. Table IV calculates the accuracy rate for the two classifiers using the nine input vectors.

The results show accuracy rates varying between 0 and 100% for different classifiers and input vectors. For instance, one can identify the pair (KNN, V9) as the best for classifying the PD fault while the pair (SVM, V6) is the worst for the same fault class. Regarding T1 fault, the best pair is (SVM, V2) and the worst is (KNN, V8). Based on the overall results, one can conduct binary classifications considering tree decision principle where the best pair shall be used in each stage to provide the best decision at the end of the classification process.

It is worth noting that the classification can be made with different input vector/classifier combinations. Therefore, not only a single path that could exist, but one can define several paths. Thus, a multi-path hybrid classifier should be considered as described in the following section.

B. Multi-path hybrid classifier

Based on the results, numerous paths can be proposed using combinations between faults classified in Table IV in descending order.

Table. IV
ACCURACY RATE FOR DIFFERENT INPUT VECTORS

	Accuracy rate using KNN (%)					
	PD	D1	D2	T1	T2	T3
V1	93.75	80.77	90.48	87.50	75.00	96.43
V2	93.75	76.92	97.62	87.50	75.00	96.43
V3	75.00	50.00	78.54	93.75	75.00	85.71
V4	62.50	53.85	78.54	71.88	81.25	85.71
V5	87.50	11.54	71.43	03.13	06.25	10.71
V6	37.50	23.08	85.71	78.13	37.50	71.43
V7	93.75	73.08	95.24	90.63	75.00	92.86
V8	18.75	11.54	88.10	00.00	00.00	14.29
V9	100	76.92	90.48	87.50	93.75	92.86
	Accuracy rate using SVM (%)					
V1	87.50	88.46	83.33	87.50	43.75	96.43
V2	93.75	80.77	90.48	96.88	87.50	89.29
V3	93.75	11.54	35.71	71.88	37.50	89.29
V4	25.00	73.08	28.57	90.63	00.00	00.00
V5	75.00	46.15	83.33	75.00	62.75	00.00
V6	00.00	00.00	88.10	84.38	00.00	82.14
V7	87.50	73.08	92.86	90.63	68.75	92.86
V8	68.75	03.85	97.62	71.88	87.50	00.00
V9	93.75	76.92	92.86	93.75	81.25	92.86

The straightforward way is to consider the same pairs for the classification. It means that one can create a multi-path classifier without hybridization in each single path (i.e., the same classifier and input vector for a given path). Eighteen classifications have been considered using two classifiers and nine different input vectors. In this case, the corresponding accuracy rates are summarized in Table V.

Table. V
ACCURACY RATE FOR DIFFERENT CLASSIFICATION PATHS

	ACCURACY RATE (%)	
	KNN	SVM
V1	88.13	83.75
V2	89.38	89.38
V3	77.50	48.75
V4	73.13	33.75
V5	32.50	60.00
V6	61.88	57.50
V7	88.13	86.25
V8	29.39	56.25
V9	89.38	90.00

As can be seen in Table V, some input vectors give good accuracy rates for both classifiers (e.g., V1, V2, V7 and V9) whilst a low accuracy rate is obtained if one changes the classifier for some input vectors (e.g., V3 with KNN and V3 with SVM). The best results in the considered case are obtained for an input vector V9 and SVM classification. In addition, using V2 with both classifiers results in an accuracy rate of 89.38%. The same result is obtained from different paths when the input vector V9 is used with KNN classification. Overall, better results may be obtained if one can study furthermore this hybridization.

From the results in Table V, one can create a multi-path classification where the final decision is taken from those decisions calculated at the output of several paths.

Table. VI
ACCURACY RATE FOR DIFFERENT MULTI-PATH CLASSIFIERS

	SPECIFICATION		ACCURACY
	CLASSIFIER	INPUT	RATE (%)
Path 1	SVM	V9	-
Path 2	SVM	V2	-
Path 3	KNN	V1	-
Multi-path 1–3	-	-	90.00
Path 4	KNN	V7	-
Path 5	KNN	V9	-
Multi-path 1–5	-	-	92.50
Path 6	SVM	V1	-
Path 7	KNN	V2	-
Multi-path 1–7	-	-	91.88
Path 8	SVM	V7	-
Path 9	KNN	V3	-
Multi-path 1–9	-	-	91.88

As a simple example, the number of paths is increased, and the final decision is made for different scenarios. Four different multipath classifiers have proposed where the number of paths is increased from classifier to another as follows:

- Multi-path Classifier 1: Paths 1, 2 and 3.
- Multi-path Classifier 2: Paths 1, 2, 3, 4 and 5.
- Multi-path Classifier 3: Paths 1, 2, 3, 4, 5, 6 and 7.
- Multi-path Classifier 4: Paths 1, 2, 3, 4, 5, 6, 7, 8 and 9.

Multipath classifier 1 groups three different paths (Paths 1, 2 and 3). Path 1 is the classification using SVM classifier with the input vector V9. Path 2 is the classification using the SVM and V2.

In general, the described paths and the obtained accuracy rates are given in Table VI where the final decision for each multipath classifier is selected from the outputs of the different paths.

In this table, the criterion for selecting final decision consists of selecting the decision with higher recurrence, which is obtained from the paths' decisions. In case of equality or difficulties in the selection, the criterion consists of prioritizing the decision of the best path (usually the first one has higher accuracy rate compared to the others).

It should be noted that the selection criteria can affect the output of the multipath classifiers. It could be another paper's subject since different factors may contribute to the final decision. For instance, it was found that the number of paths used in the multipath classifier considerably impacts the final decision. Figure 5 shows the obtained accuracy rate as a function of the number of paths.

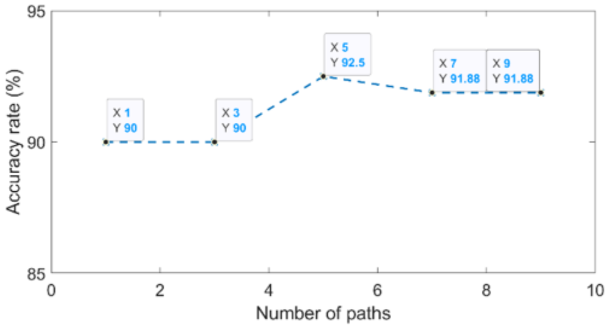

Fig. 5: Accuracy rate as a function of number of paths.

The results indicate that the number of the selected paths is a sensitive factor for creating a multi-path hybrid classifier. A higher number of paths may reduce the effectiveness of the classifiers.

Therefore, an appropriate selection should be adopted where optimal choices of classification algorithm with appropriate input data should be considered to diagnose transformer faults better.

Table. VII
COMPARISON BETWEEN THE PROPOSED ALGORITHM AND OTHER RELEVANT METHODS

	H2	CH4	C2H6	C2H4	C2H2	ACT	IEC-60599	Roger's 4 ratios	Duval	TKNN	TSVM	DT-V4	MPH
1	1230	163	27	692	233	D2	D2	UD	D2	D1	D2	D2	D2
2	120	10	30	25	5	D1	PD	UD	T3	D1	PD	D1	D1
3	3700	6400	2400	10	7690	T2	UD	UD	D1	T2	T3	T1	T2
4	6	2990	29990	67	26076	T1	UD		D1	T1	T1	T1	T1
5	34	21	4	56	49	D2	D2	D2	D2	D2	D2	D2	D2
6	120	140	30	0	120	T1	UD	UD	D1	T1	T2	T1	T1
7	240	17	0	5	40	PD	UD	UD	D1	PD	PD	PD	PD
8	6454	2313	121	6432	2159	D2	D2	UD	D2	D2	D2	D2	D2
9	650	53	20	0	34	PD	UD	PD	D1	PD	PD	PD	PD
10	125	680	290	20	900	T3	UD	UD	D1	T3	T3	T1	T3
11	1076	95	71	231	4	PD	UD	UD	T3	PD	PD	PD	PD
12	140	95	10	80	60	D2	D2	D2	D2	D2	D2	D2	D2
13	300	700	280	36	1700	T3	UD	UD	D1	T3	T1	T3	T3
14	960	4000	1290	6	1560	T2	UD	UD	D1	T2	T1	T2	T2
15	1450	940	211	61	322	T1	UD	UD	D1	T1	T1	T1	T1
16	2500	10500	4790	6	13500	T2	UD	UD	D1	T2	T1	T2	T2
17	305	100	33	541	161	D1	D2	UD	D2	D2	D2	D1	D2
18	796	999	234	31	1599	T3	UD	UD	D1	T3	T1	T3	T3
19	37800	1740	249	8	8	PD	PD	PD	PD	PD	PD	PD	PD
20	33046	619	58	0	2	PD	UD	PD	PD	PD	PD	PD	PD
							5/20	5/20	6/20	18/20	12/20	18/20	19/20
ACCURACY RATE (%)							25	25	30	90	55	90	95

ACT: ACTUAL CLASS OF FAULT UD: UNDETERMINED

Therefore, an appropriate selection should be adopted where optimal choices of classification algorithm with appropriate input data should be considered to diagnose transformer faults better.

C. Independant data and validation

A dataset of 20 new samples tests different classifiers for the validation and comparison stages, including conventional ones (IEC-60566 method, Roger's ratios and Duval triangle).

A total of seven classifiers are considered as shown in Table VII which gives the decisions of different classifiers along with the accuracy rates. The classifier MPH is a multi-path hybrid classifier that combines three paths–TKNN (as best path), TSVM and DT-V4. TKNN is a hybridization between the decision tree and the KNN classifier whilst TSVM is similar hybridization using SVM with Decision tree principle as studied in a previous work [26]. DT-V4 is a classification using DT classification using the input vector V4. It should be noted that the selection here is just an example and an infinite number of choices can be considered.

The results show that the MPH improved the diagnosis results (95 %) compared to other conventional techniques and single-path classifiers. Therefore, the proposed methodology can help classify faults in oil-immersed power transformers by providing a better accuracy rate than conventional diagnostic techniques.

V. CONCLUSION

A study on transformer oil diagnosis using DGA has been made in this paper using 501 samples to provide an advance in the field. The pioneer classifiers SVM and KNN have been used with different input vectors to understand the pair "classifier, input vector" effect on the diagnostic accuracy. For a given sample, the decision is based on the use of a vote on the results of the two algorithms (SVM and KNN) through the injection of several input vectors. Analyzing the results, classification paths were considered, where multiple paths were combined to form a new multi-path hybrid classifier. This strategy can be more practical for improving the diagnosis of power transformer oil than using the classical way when employing a single classifier and a unique input vector. Enrichment in the input vector crafted the classifier to reduce the percentage of misdiagnosis and the hybridization with another classifier made a strong decision on the state of the sample. Hybridizing several algorithms and input vectors can effectively diagnose the power transformer fault.

REFERENCES

[1] S. Ghoneim, T.A. Farrag, A.A. Rashed, E.M. El-Kenawy, and A. Ibrahim, "Adaptive Dynamic Meta-Heuristics for Feature Selection and Classification in Diagnostic Accuracy of Transformer Faults," IEEE Access, vol. 9, 2021, pp. 78324–78340, doi: 10.1109/ACCESS.2021.3083593.

[2] Recent Developments in DGA Interpretation, CIGRE Technical Brochure 296, Paris, France, Jun. 2006.

[3] E. Altayef, F. Anayi, M. S. Packianather and O. Kherif, "On the Effects of Lamination Artificial Faults in a 15 kVA Three-Phase Transformer Core," IEEE Access, vol. 10, pp. 19348-19355, 2022, doi: 10.1109/ACCESS.2022.3151367.

[4] Y. Benmahamed, M. Teguar, and A. Boubakeur, "Application of SVM and KNN to Duval pentagon 1 for transformer oil diagnosis," IEEE Trans. Dielectr. Electr. Insul., vol. 24, no. 6, pp. 3443–3451, Dec. 2017.

[5] M. Kezunovic and Y. Guo, "Modeling and simulation of the power transformer faults and related protective relay behavior," IEEE Trans. Power Del., vol. 15, no. 1, pp. 44–50, Jan. 2000.

[6] X. Ji, Y. Zhang, and Q. Liu, "Insulation Condition Assessment of Power Transformers Employing Fused Information in Time and Space Dimensions, Electric Power Components and Systems", Electric Power Components and Systems, vol. 48, no. 1-2, pp. 213-223, Mar. 2020.

[7] Y. Benmahamed, O. Kherif, M. Teguar, A. Boubakeur and S. Ghoneim, "Accuracy Improvement of Transformer Faults Diagnostic Based on DGA Data Using SVM-BA Classifier", MDPI Energies, vol. 14, no. 10, pp. 2970, 2021, doi: 10.3390/en14102970.

[8] Mineral Oil-Impregnated Electrical Equipment in Service—Guide to the Interpretation of Dissolved and Free Gases Analysis, IEC Publication 60599, 2007.

[9] "IEEE Guide for the Interpretation of Gases Generated in Mineral Oil-Immersed Transformers," in IEEE Std C57.104-2019 (Revision of IEEE Std C57.104-2008), vol., no., pp.1-98, 1 Nov. 2019.

[10] M. Duval, 'Dissolved gas analysis: It can save your transformer,' IEEE Elect. Insul. Mag., vol. 5, no. 6, pp. 22–27, Nov./Dec. 1989.

[11] K. Kaur, D. Bhalla and J. Singh, "Fault Diagnosis for Oil Immersed Transformer Using Certainty Factor," in IEEE Transactions on Dielectrics and Electrical Insulation, vol. 31, no. 1, pp. 485-494, Feb. 2024, doi: 10.1109/TDEI.2023.3307513.

[12] T. Manoj, C. Ranga, Sherif S. M. Ghoneim, U. Mohan Rao, Saad A. Mohamed Abdelwahab, "Alternate and Effective Dissolved Gas Interpretation to Understand the Transformer Incipient Faults", IEEE Transactions on Dielectrics and electrical insulation, Jan. 2023.

[13] Rahman Azis Prasojo, Muhammad Akmal A Putra, Meyti Eka Apriyani, Anugrah Nur Rahmanto, Sherif SM Ghoneim, Karar Mahmoud, Matti Lehtonen, Mohamed MF Darwish, "Precise transformer fault diagnosis via random forest model enhanced by synthetic minority over-sampling technique", Electric Power Systems Research, Volume, 220, Pages 109361, 2023.

[14] N. Bakar, A. Abu-Siada, and S. Islam, "A review of dissolved gas analysis measurement and interpretation techniques," IEEE Elect. Insul. Mag., vol. 30, no. 3, pp. 39–49, May/Jun. 2014.

[15] Prasojo, R.A.; Gumilang, H.; Suwarno; Maulidevi, N.U.; Soedjarno, B.A. A Fuzzy Logic Model for Power Transformer Faults' Severity Determination Based on Gas Level, Gas Rate, and Dissolved Gas Analysis Interpretation. Energies 2020, 13, 1009. https://doi.org/10.3390/en13041009.

[16] Sherif S. M. Ghoneim, Karar Mahmoud, Matti Lehtonen, And Mohamed M. F. Darwish, "Enhancing Diagnostic Accuracy of Transformer Faults Using Teaching-learning-Based Optimization", IEEE Access, VOLUME 9, 2021, pp. 30817- 30832.

[17] Ward, S.A.; El-Faraskoury, A.; Badawi, M.; Ibrahim, S.A.; Mahmoud, K.; Lehtonen, M.; Darwish, M.M.F. Towards Precise Interpretation of Oil Transformers via Novel Combined Techniques Based on DGA and Partial Discharge Sensors. Sensors 2021, 21, 2223. https://doi.org/10.3390/s21062223.

[18] B. Zhao, M. Yang, H.R. Diao, B. An, Y.C. Zhao, Y.M. Zhang, A novel approach to transformer fault diagnosis using IDM and naive credal classifier, International Journal of Electrical Power Energy Systems, Volume 105, 2019, Pages 846-855.

[19] Abu-Siada, A. Improved Consistent Interpretation Approach of Fault Type within Power Transformers Using Dissolved Gas Analysis and Gene Expression Programming. Energies 2019, 12, 730. https://doi.org/10.3390/en12040730

[20] M. Duval, “A review of faults detectable by gas-in-oil analysis in transformers,” in IEEE Electrical Insulation Magazine, vol. 18, no. 3, pp. 8-17, May-June 2002.

[21] M. Duval and L. Lamarre, “The Duval Pentagon- Anew Complementary Tool for the Interpretation of Dissolved Gas Analysis in Transformers,” IEEE Elec. Insul. Mag., Vol. 30, No. 6, pp. 9-12, 2014.

[22] M. Zhang and W. Chen, “Fault Diagnosis of Power Transformer Based on SSA—MDS Pretreatment,” in IEEE Access, vol. 10, pp. 92505-92515, 2022.

[23] J. Li, G. Li, C. Hai, and M. Guo, “Transformer Fault Diagnosis Based on Multi-Class AdaBoost Algorithm,” in IEEE Access, vol. 10, pp. 1522-1532, 2022.

[24] H. Zhou, L. Lu, G. Wang and Z. Su, "A New Validity Detection Method of Online Status Monitoring Data for Power Transformer," in IEEE Access, vol. 12, pp. 16095-16104, 2024, doi: 10.1109/ACCESS.2024.3358399.

[25] I. B. M. Taha, A. Hoballah and S. S. M. Ghoneim, “Optimal ratio limits of rogers’ four-ratios and IEC 60599 code methods using particle swarm optimization fuzzy-logic approach,” in IEEE Transactions on Dielectrics and Electrical Insulation, vol. 27, no. 1, pp. 222-230, Feb. 2020.

[26] Y. Wu, X. Sun, Y. Zhang, X. Zhong and L. Cheng, “A Power Transformer Fault Diagnosis Method-Based Hybrid Improved Seagull Optimization Algorithm and Support Vector Machine,” in IEEE Access, vol. 10, pp. 17268-17286, 2022.

[27] O. Kherif, Y. Benmahamed, M. Teguar, A. Boubakeur and S. S. M. Ghoneim, “Accuracy Improvement of Power Transformer Faults Diagnostic Using KNN Classifier with Decision Tree Principle,” in IEEE Access, vol. 9, pp. 81693-81701, 2021.

[28] Sherif S. M. Ghoneim, Ibrahim B. M. Taha, Rizk Fahim, Saad A. Mohamed Abdelwahab, “Effect of Data Transformation on the Diagnostic Accuracy of Transformer Faults and the Performance of the Supervised Classifiers”, International Journal of Renewable Energy Research, Vol.12, No.2, June, 2022.

[29] M. Duval, and A. DePablo, "Interpretation of turn-to-turn insulation fault by dissolved gas analysis," in IEEE Transactions on Dielectrics and Electrical Insulation, vol. 25, no. 4, pp. 1560-1566, August 2018, doi: 10.1109/TDEI.2018.007477.

[30] Egyptian Electricity Holding Company (EEHC) Reports, 1991-2016.

[31] J. Dukarm and F. Jakob “Thermodynamic estimation of transformer fault severity” IEEE/PES Transmission and Distribution Conference and Exposition (TD), Dallas, TX, USA, pp. 1-1, 2016

[32] J. Soni and D. Suthar “An Experimental Analysis to Check Accuracy of DGA Using Duval Pentagonal Method in Power Transformer”, ICRISET2017 the Int. Conf. on Research and Innovations in Science, Engineering and Technology, vol 1, pp. 394–401, Aug. 2017

[33] https://www.mathworks.com/help/stats/fitcsvm.html

[34] https://www.mathworks.com/help/stats/fitcknn.html

[35] https://www.mathworks.com/help/stats/fitctree.html

VI. BIOGRAPHY

YOUCEF BENMAHAMED received the engineer’s and master’s degrees in power electronics engineering, in 2014, and the Ph.D. degree in high voltage techniques from the École Nationale Polytechnique (ENP) of Algiers, in 2019. He is currently an associate professor with the ENP. His research interests include diagnosis, artificial intelligence, and optimization techniques.

OMAR KHERIF Omar obtained a M/Eng. and a Ph.D. in electrical engineering from the Ecole Nationale Polytechnique (ENP, Algiers) in 2015 and 2019, respectively. Currently, he holds the position of Discipline Manager (Earthing Lightning Protection Systems) at RINA Tech UK Limited. He was the Head of Design Services with Kingsmill Industries (UK) Limited, following the successful completion of a KTP Project involving Cardiff University and Kingsmill Industries (UK) Limited. Dr Kherif is an active member of IEEE, IEEE SIGHT, GEL/81(BSI), IET, CNHT, ICAEE, CISTEM and EMTP/ATP-EUG. His main interests are in high voltage engineering, electromagnetic transients, earthing and lightning protection solutions.

SOFIANE CHIHEB received his M.S. degree from the Badji Mokhtar University of Annaba, in 2013 and his Ph. D. degree in electrical engineering from the Ecole Nationale Polytechnique (ENP), in 2018. He is currently an associate professor with the National Higher School of Technology and Engineering (ENSTI) Annaba - Algeria. His research interests include high voltage techniques, grounding systems, power grids and renewable energies.

MADJID TEGUAR received the degree in electrical engineering, the master’s degree, and the Ph.D. degree in high voltage engineering from the École Nationale Polytechnique (ENP) of Algiers, in 1990, 1993, and 2003, respectively. He is currently a Professor of Electrical Engineering with ENP. His research interests include insulation systems, insulation coordination, earthing of electrical energy systems, and polymeric cables insulation.

SHERIF S. M. GHONEIM received the B.Sc. and M.Sc. degrees from the Faculty of Engineering at Shoubra, Zagazig University, Egypt, in 1994 and 2000, respectively, and the Ph.D. degree in electrical power and machines from the Faculty of Engineering, Cairo University, in 2008. Since 1996, he has been teaching with the Faculty of Industrial Education, Suez Canal University, Egypt. From 2005 to 2007, he was a Guest Researcher with the Institute of Energy Transport and Storage (ETS), University of Duisburg–Essen, Germany. He joined Taif University as an Associate Professor at the Electrical Engineering Department, Faculty of Engineering. His research interests include grounding systems, dissolved gas analysis, breakdown in SF6 gas, and AI technique applications.

AHMED BOUBAKEUR was born in Biskra, Algeria, in 1952. He received the engineer’s degree in electrical engineering from the École Nationale Polytechnique (ENP) of Algiers, in 1975, and the Ph.D. degree in technical sciences from the Institute of High Voltage Engineering, Warsaw University of Technology, Poland, in 1979. He is currently a Professor with the ENP of Algiers, where he has been giving lecturers and supervising research in the field of high voltage engineering, since 1982. His research interests include discharge phenomena, insulators pollution, lightning, polymeric cables insulation, transformer oil ageing, neural networks and fuzzy logic application in HV insulation diagnosis, and electric field calculation and measurement. He is also a member of IEEE DEIS and the Algerian HV Power Systems Association ARELEC (National Algerian Comity of CIGRE and ENP Elders Association ADEP). He has been a member of the Editorial Board and an Associate Editor of IET Science, Measurement & Technology (SMT).

Woody Biomass Cogeneration with Hot Air Turbine: Application to a Wood Pellet Production Unit in Algeria

Amel Hamdi, Mohammed Amouri, Hocine Bennour, Toudert Ahmed Zaïd & Rabah Bouarab

Abstract− In this paper, the performance of a hot air turbine operating in an industrial combined heat and power (CHP) cogeneration is investigated, electrical and thermal energy supplied are intended for a pellet production unit. This unit is powered by Eucalyptus residue at 50% moisture content recovered from a forest located in El Taref, north-east of Algeria. The results show that when the air temperature at the boiler inlet Te exceeds 100 °C, an excess air ratio α above 90 % is required to maintain the flame temperature below 1200 K. Based on this, the parameters were set to α = 80 % and Te = 100 °C, resulting in a flame temperature of 1192 K. The turbine inlet temperature T3, which must remain below the flame temperature, was fixed at 1140 K. Once these conditions were established, the compression ratio maximizing the overall efficiency was determined to be around 8, yielding a cogeneration efficiency of 53 %, with an electrical efficiency of 20 % and a thermal efficiency of 33 %.

***Keywords*−Biomass, Cogeneration, Hot air turbine, Pellet.**

NOMENCLATURE

C_{ph}	specific oil (kJ/kg K)
C_{pb}	specific heat wood (kJ/kg K)
C_{pf}	specific heat of fume (kJ/kg K)
C_{P_a}, C_{P_g}	specific heats of air and products of combustion respectively (Btu/lb °F)
h	enthalpy (kJ/kg)
$\dot{m}_b$	wood mass flow rate (kg/s)
$\dot{m}_{cog}$	amount of wood for cogeneration system (kg/s)
$\dot{Q}$	Dryer heat requirement (kW)
$\dot{Q}_C$	Condenser heat rejection rate (kW)
$\dot{w}_{ORC}$	ORC power (kW)
$\dot{W}_{net}$	power required to supply the production unit (kW)
T	temperature (K)
τ	compression ratio
CHP	combined heating and power
ORC	Organic rankine cycle
LHV	lower heating value
HHV	higher heating value
α	total air ratio
α_0	excess air ratio
ε	gas / oil exchanger efficiency
η	efficiency

Manuscript received November 22, 2025; revised January 5, 2026.

A. Hamdi, R. Bouarab and T. Ahmed Zaid are with Laboratoire de Valorisation des Energies Fossiles, Chemical Engineering Department, Ecole Nationale Polytechnique, Algiers, Algeria. (email: amel.hamdi@g.enp.edu.dz , rabah.bouarab@g.enp.edu.dz, toudert.ahmed-zaid@g.enp.edu.dz).

M. AMOURI is with Centre de Développement des Energies Renouvelables CDER, Bouzareah, Algies, Algeria (email: m.amouri@cder.dz)

H. Bennour is with Mechanical Engineering Department, Ecole Nationale Polytechnique, Algiers, Algeria. (email: hben582009@gmail.com)

Digital Object Identifier (DOI): 10.53907/enpesj.v5i2.352

I. INTRODUCTION

The most common primary energy sources are fossil fuels like coal, natural gas, and petroleum, but their emissions seriously harm the environment by causing acid rain, global warming, ozone layer degradation, and ecosystem contamination. Supporting a sustainable energy transition and addressing environmental issues can be achieved through promoting and developing renewable energy [1]-[3].

As the best long-term solution to achieve environmental goals, the Algerian government is committed to promoting renewable energy through related policies and programs aimed at preserving dwindling fossil resources [4].

Initially the objectives of the National Plan for Renewable Energy (2011-2020) were to reach 11.000 MW of RE by 2030. However, in 2015, the Algerian government revised the initial program to target 22,000 MW of renewable energy by 2030 with the objective that 27% of all electricity produced come from renewable sources [5], [6].

Biomass has been recognized as a promising energy source. because it offers many social, economic, and environmental benefits [7]-[9], Currently, there is significant interest in utilizing agricultural waste as a replacement for fossil fuel. It can significantly contribute to decarbonizing energy production and achieving carbon neutrality targets [10], [11]. The pretreatment of biomass to improve its fuel quality or to meet specific performance standards across different energy system scales is a widely adopted practice. Biomass pelletization through the densification of raw materials significantly increases bulk density and reduces storage and transportation costs. In comparison to the direct combustion of untreated biomass, the use of biomass pellets in specially designed stoves can greatly enhance combustion efficiency and reduce pollutant emissions. It is widely recognized that, due to their higher density, biomass pellets exhibit slower devolatilization and prolonged combustion duration, which promotes more complete and efficient [12], [13].

Wood pellets are characterized by a high bulk density of up to 750 kg/m³ and a lower heating value of approximately 16.5 GJ per ton. In contrast, woodchips have a lower bulk density of around 250 kg/m³ and an energy content of about 13 GJ per ton [14]. According to Monteiro et al. [15], combining biomass power generation with pellet production plants represents a highly effective strategy for optimizing pellet manufacturing processes. Combined heat and power (CHP) operations often represent the most efficient use of biomass, The energy conversion rate of biomass cogeneration can reach more than twice that of pure power generation [16], [17]. Various biomass cogeneration systems have been developed and implemented to optimize the production of heat and electricity. Wood combustion generates exhaust gases at high temperatures typically between 900 and 1000 °C [18], [19], which makes it especially well-suited for integration with high-temperature heat recovery technologies such as hot air turbines. Hot air turbines are a developing technology that enables the use of low-quality fuels by isolating the working fluid from combustion gases. Heat is transferred through a high-temperature exchanger operating above 900 °C to ensure reliable turbine operation [20], [21]. Indeed, Ibrahim et al. [22] highlighted in their study that the air temperature at the inlet of the turbine and the compressor's air compression ratio are critical parameters in this technology, with an optimal compression ratio existing that maximizes the system's efficiency.

This study analyzes a cogeneration system designed to supply 500 kW of electrical power for the production unit and to deliver thermal energy (via flue gases at 400–600 °C) for wood drying in a rotary drum dryer. A mathematical model was developed to evaluate system performance and optimize its operating parameters. The simulations are carried out in MATLAB using thermodynamic properties from the CoolProp database. An algorithm has been developed to determine the following parameters:

1. The variation of exhaust gas temperature at the chimney outlet,
2. the variation of flue gas temperature at the dryer outlet,
3. the variation of the electrical efficiency of the system,
4. The variation of the thermal efficiency of the system and
5. the variation of the overall cogeneration efficiency, as functions of the compression ratio, flame temperature, and turbine inlet air temperature.

This parametric study enabled the identification of the system's optimal parameters and the estimation of the required wood quantity for the project.

II. MATERIALS AND METHODS

A. *Production Unit*

Wood pellets, made from wood industry byproducts, are 6–8 mm in diameter and up to 40 mm long. Production involves chipping, crushing, drying, pelletizing, and cooling, followed by packaging for transport [23]. A simplified representation of a typical unit available on the global market is shown in Fig. 1, along with the amount of electricity required for each stage of the process [24].

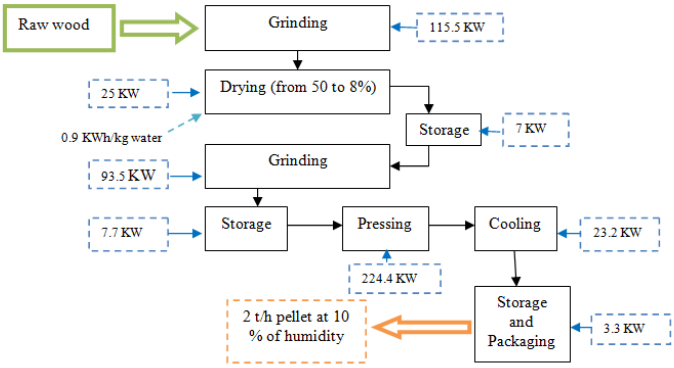

Fig. 1: A simplified representation of a common pellet production unit.

B. *Biomass Resources*

This study is based on the assumption of continuous wood availability, used as a working hypothesis to simplify the model and focus on the technical aspects of energy consumption. The assumption, validated by the General Directorate of Forests (DGF), presumes constant wood production throughout the year. The exploitable areas were determined according to a five-year program (see Table I).

Table. I

EXPLOITED AREA FROM 2016 TO 2020 AND QUANTITY OF SLASH RECOVERED FROM EL TAREF FORESTS [31]

Year	2016	2017	2018	2019	2020
Exploited area (ha)	619	780	747	1000	782
Slash recovered (ton)	7738	9750	9338	12500	9775

In El Taref region, Eucalyptus plantations cover 10,822 hectares. Eucalyptus is well-suited for short-rotation systems due to its fast growth, environmental adaptability, and high lignin and cellulose content, making it ideal for biomass-based heat and electricity production. These plantations also support soil regeneration and reduce erosion [25], [26]. The DGF estimates that 20 to 30 m³/ha of woody biomass with a density of 500 kg/m³ can be recovered; this study assumes a recoverable volume of 25 m³/ha. The elemental composition of Eucalyptus is shown in Table II.

C. *Combustion Assumptions*

The study assumes complete combustion of wood, with all products gaseous except for ashes. Considering air contains 3.76 moles of nitrogen per mole of oxygen, the theoretical air needed for combustion is calculated. For raw wood at 50% moisture, 2.81 kg of air per kg of wood is required, with 25–100% excess air typically used to ensure full combustion [27].

Table. II

ELEMENTAL MASS COMPOSITION BASED ON DRY SUBSTANCE AND AT 50% MOISTURE CONTENT [32]

	C	H	O	N	S	Ash
Dry	48.33	5.89	45.13	0.15	0.01	0.49
50 % moisture content	24.16	2.95	22.56	0.07	0.01	0.24

D. *Composition of Flue Gases*

Assuming complete combustion of Eucalyptus with ashes settling in the furnace, the resulting flue gases contain CO2, H2O, SO2, N2, and O2 (when excess air is present). The fuel's smoke power, measured as kilograms of smoke per kilogram of raw wood, is calculated as follows.

$$m_f = [CO_2] + [H_2O]_f + [SO_2] + [N_2] + [O_2] \tag{1}$$

where: [CO2], [H2O], [SO2], [N2] and [O2], represent masses formed from the combustion of 1 kg of raw fuel.

E. Calorific value of the fuel

The higher heating value (HHV) and lower heating value (LHV) of the fuel are determined using correlations based on the mass composition (dry basis). Using various calculations, the average values of HHV and LHV are 19220 kJ/kg and 7700 kJ/kg, respectively [28], [29].

F. Flame temperature T5

According to empirical formulas in the literature, furnace combustion is not totally adiabatic. One such formula is Eq. 2 (from [30]) as follows:

$$T_5 = \frac{LHV + A\alpha(HHV)C_{p_a}(T_a - 80)10^{-6}}{(1 - 0.01)(Ash) + A\alpha(HHV)C_{p_g}10^{-6}} \qquad (2)$$

where: A is the theoretical air required per million (Btu fired,lb) (A = At * 106/HHV); Cpa and Cpf are the specific heats of air and products of combustion respectively (Btu/lb. °F); the LHV and HHV are given in British thermal units (Btu/lb); (Ash) is given as a percentage; α : total air ratio (theoretical air ratio + excess air ratio α0). Theoretical air ratio is the ratio of the actual air required to the stoichiometric air required. For perfect combustion, the theoretical air ratio is 1.

III. SYSTEM DESCRIPTION

The proposed TAC system for the cogeneration unit is illustrated in Fig. 2.

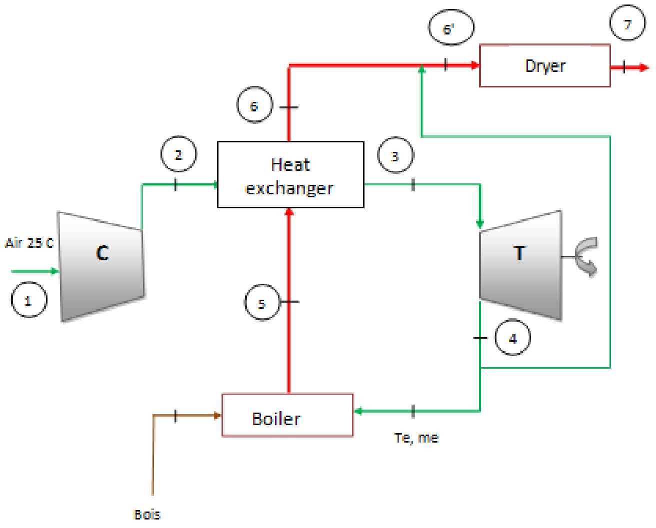

Fig 1: Hot air turbine system proposed for the cogeneration unit

It consists of a boiler, a compressor, a heat exchanger, and a turbine. Combustion gases from the wood-fired boiler can reach temperatures of up to 950 °C. These hot gases are directed into a heat exchanger, where they are used to heat air that has been previously compressed. After passing through the heat exchanger, the compressed air reaches high temperatures, typically between 700 and 950 °C. This hot air then drives a turbine connected to a generator, producing electricity. At the turbine outlet, the air remains hot. A portion of this air is mixed with the combustion gases exiting the heat exchanger and routed to a wood dryer, which is part of the pellet production unit. The remaining hot air is mixed with ambient air to improve combustion efficiency in the boiler.

A. Hypotheses

All operations (compressions, expansions, and heat exchanges) are assumed to be internally reversible; the air is assumed to behave as an ideal gas. The calculations were conducted with the following parameters: isentropic efficiency of the turbine (ηisT=0.90), Compressor efficiency (ηc =0.88) and T1: air temperature at compressor inlet (T1=25 C).

B. Balance Sheet on the Cogeneration Unit

The temperature rise across the compressor is determined using the following thermodynamic relationship

$$T_{2s} = T_1 * \tau^{\frac{\gamma-1}{\gamma}} \qquad (3)$$

Noting that $\alpha = \frac{\gamma-1}{\gamma}$, it yields

$$T_{2s} = T_1 * \tau^{\alpha} \qquad (4)$$

The efficiency of the compressor is defined as follows:

$$\eta_c = \frac{T_{2s}-T_1}{T_2-T_1} \qquad (5)$$

$$T_2 = T_1 * (1 + \frac{\tau^{\alpha}-1}{\eta_c}) \qquad (6)$$

However, T_{4s} can be expressed as follows

$$T_{4s} = T_3 * \tau^{-\alpha} \qquad (7)$$

The turbine efficiency is defined as follows:

$$\eta_t = \frac{T_3-T_4}{T_3-T_{4s}} \qquad (8)$$

which gives

$$T_4 = T_3(1 - \eta_t * (1 - \tau^{-\alpha})) \qquad (9)$$

Energy balance on the air-gas heat exchanger is given as follows

$$\dot{m}_a Cp_{a2}T_2 + \dot{m}_f Cp_{f5}T_5 = \dot{m}_a Cp_{a3}T_3 + \dot{m}_f Cp_{f6}T_6 \qquad (10)$$

$$\frac{\dot{m}_a(Cp_{a2}T_2-Cp_{a3}T_3)+\dot{m}_f Cp_{f5}T_5}{\dot{m}_f}=Cp_{f6}T_6 \qquad (11)$$

where, Eq. 11 is solved by iterations using MATLAB to find T6, while Cp_{f6} is determined as a function of T6.

A portion of the air exiting the turbine is injected into the flue gases leaving the heat exchanger. To determine the mass flow rate of ambient air ($\dot{m}_e$) required to achieve the desired air temperature at the boiler inlet, an energy balance is performed at point e, where the hot air from the turbine mixes with ambient air.

$$\dot{m}_a Cp_{a4}T_4 + \dot{m}_e Cp_{a25}T_{atm} = \dot{m}_a Cp_{aTe}T_e + \dot{m}_e Cp_{a4}T_4 \qquad (12)$$

$$\dot{m}_e = \frac{\dot{m}_a(Cp_{aTe}T_e-Cp_{a4}T_4)}{(Cp_{a25}T_{atm}-Cp_{a4}T_4)} \qquad (13)$$

The energy balance at point 6′, representing the mixing of combustion gases with turbine outlet air, is expressed as:

$$\dot{m}_e Cp_e T_4 + \dot{m}_{f6}Cp_{f6}T_6 = (\dot{m}_{f6}+\dot{m}_e)Cp_{f6'}T_{6'} \qquad (14)$$

$$\frac{\dot{m}_e Cp_e T_4+\dot{m}_{f6}Cp_{f6}T_6}{(\dot{m}_{f6}+\dot{m}_e)}=Cp_{f6'}T_{6'} \qquad (15)$$

It should be clarified that Eq. 15 is solved by iterations using MATLAB to find T6', where $Cp_{f6'}$ is determined as a function of T6'. As for the Dryer heat requirement, the mass balance through the dryer gives:

$$(\dot{m}_{f6'}+\dot{m}_e)Cp_{f6'}T_{6'} + \dot{m}_{b1}Cp_{b1}T_{b1} = (\dot{m}_{f6'}+\dot{m}_e)Cp_{f7}T_7 + \dot{m}_{b2}Cp_{b2}T_{b2} + \dot{m}_{ev}h_g \quad (16)$$

$$(\dot{m}_{f6'}+\dot{m}_e)Cp_{f6'}T_{6'} + \dot{m}_{b1}Cp_{b1}T_{b1} - \dot{m}_{b2}Cp_{b2}T_{b2} = (\dot{m}_{f6'}+\dot{m}_e)Cp_{f7}T_7 + \dot{m}_{ev}h_g \quad (17)$$

The equation is solved iteratively to determine T7. The iterations are performed using MATLAB, where Cpf6′ and hg are evaluated at each step based on T7 and the molar fraction of water in the flue gases, respectively.

Installation efficiency:

Turbine power

$$\dot{w}_T = \dot{m}_a\ (Cp_{a3}T_3 - Cp_{a4}T_4) \quad (18)$$

Compressor power

$$\dot{w}_c = \dot{m}_a\ (Cp_{a2}T_2 - Cp_{a1}T_1) \quad (19)$$

$$\dot{w}_{cycle} = \dot{w}_t - \dot{w}_c \quad (20)$$

Note that the power needed to operate the production unit ($\dot{w}_{unite}$) is 500 KW. In this case, the quantity of wood required to generate this energy is calculated as follows:

$$\dot{m}_{cog} = \frac{\dot{w}_{unite}}{\dot{w}_{cycle}} \quad (21)$$

$$\eta_{el} = \frac{\dot{w}_{unite}}{PCI*\dot{m}_{cog}} \quad (22)$$

in which, Q̇ is the quantity of heat released by the fumes at the dryer. This can be written as follows

$$\dot{Q} = (\dot{m}_{f6'}+\dot{m}_e)\dot{m}_{cog}Cp_{f6'}T_{6'} - (\dot{m}_{f6'}+\dot{m}_e)\dot{m}_{cog}Cp_{f7}T_7 (23)$$

$$\eta_{th} = \frac{\dot{Q}}{PCI*\dot{m}_{cog}} \quad (24)$$

$$\eta_{cog} = \eta_{el} + \eta_{th} \quad (25)$$

IV. RESULTS AND DISCUSSION

In order to investigate how the flame temperature, air temperature at the turbine's inlet (T3), and compression ratio affect the cycle's performance, we have increased the amount of excess air from 35% to 85%, T3 from 1000 K to 1180 K, and the compression ratio from 2 to 10. To ensure stable and complete combustion without operational issues, it is essential to minimize bottom ash formation and limit unburned gaseous and solid emissions. Bottom ash forms when ash reaches its melting point, which, for wood, must remain below its softening temperature approximately 1200 °C. To prevent this, the flame temperature should be kept under 1000 °C by adjusting the excess air ratio (α_0). Unburned materials not only reduce system efficiency but also have harmful environmental effects. Additionally, the flue gas temperature at the boiler outlet should remain above the acid dew point to prevent condensation. While this point typically ranges from 125 to 135 °C for sulfur-rich fuels [33], [34], a lower limit of 100 °C is acceptable in this study due to the low sulfur content (0.01%) of the wood.

The temperature at the dryer inlet, T6', must remain above the dryer's operating temperature (>400 °C). The evolution of flame temperature as a function of the total air ratio (α) and the boiler inlet air temperature (Te) is shown in Fig. 3.

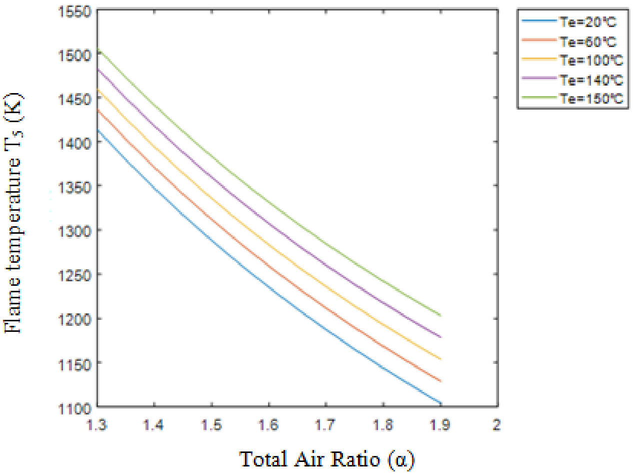

Fig.2: Evolution of flame temperature with total air ratio (α) and boiler inlet air temperature (Te)

This figure shows that the flame temperature varies inversely with the excess air ratio: as the excess air increases, the flame temperature decreases. This trend is expected, since higher excess air dilutes the combustion gases with a larger amount of nitrogen and unreacted oxygen, thereby lowering the flame temperature. Conversely, the flame temperature increases with higher boiler inlet air temperatures. Indeed, preheated combustion air enhances the combustion reaction and reduces thermal losses associated with heating the oxidant. It is also observed that for boiler inlet air temperatures above 100 °C, an excess air ratio higher than 90% is required to maintain the flame temperature below 1200 K. From these observations, optimal operating parameters can be set. By selecting: an excess air ratio α = 80% and a boiler inlet air temperature Te = 100 °C, the resulting flame temperature is 1192 K (≈ 919 °C), which represents a satisfactory compromise between energy performance and compliance with material constraints and pollutant emission limits.

The influence of turbine inlet air temperature and compression ratio has been studied. Variation of electrical, thermal, and cogeneration efficiencies all with compression ratio are presented in Fig. 4, Fig. 5 and Fig. 6, respectively.

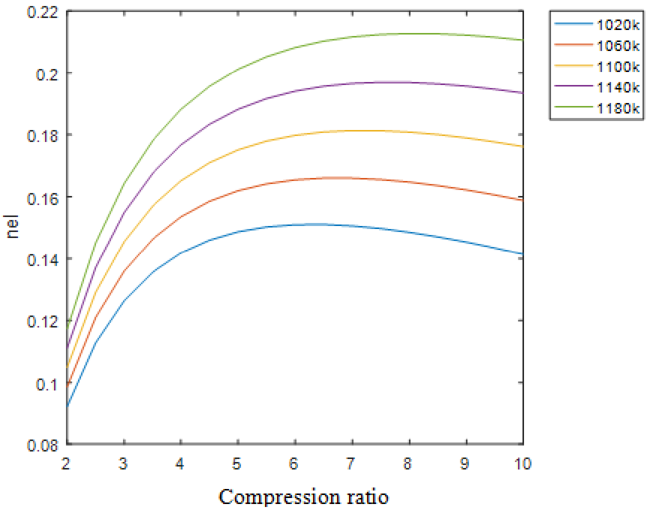

Fig.3: Variation of electrical efficiency with compression ratio

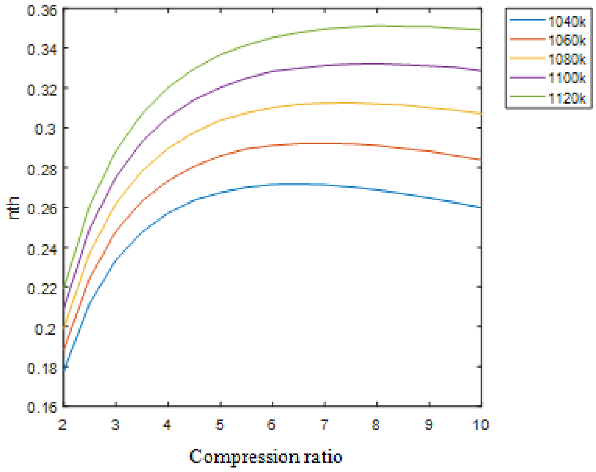

Fig.4: Variation of thermal efficiency with compression ratio

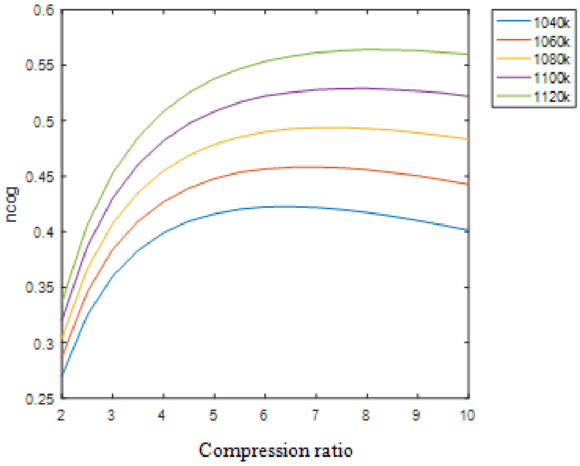

Fig.5: Variation of cogeneration efficiency with compression ratio

From the results shown in Fig.4, 5, and 6, it can be observed that, regardless of the value of T3, the curves display a similar trend, which can be divided into two distinct phases:

First phase: a rapid increase in performance up to a maximum point. This growth reflects the energy gain obtained from raising the turbine inlet air temperature.

Second phase: beyond this maximum, a stability zone appears, where performance remains nearly constant. The recorded values stay close to those at the optimal point, indicating that increasing T3 beyond a certain threshold brings little additional improvement.

Furthermore, for a fixed compression ratio, the different parameters studied (efficiency, gas temperature, etc.) generally increase with T3. However, this temperature must remain below the flame temperature, with a minimum safety margin of 50 °C. This constraint is essential to avoid overheating issues that could damage materials and increase NOx emissions. Taking these conditions into account, the turbine inlet air temperature can be set at T3 = 1140 K (867 °C). This choice represents an optimal compromise, ensuring both high energy performance and safe cycle operation.

Fig.7 and Fig. 8 illustrate the evolution of the inlet and outlet temperatures of the dryer, respectively.

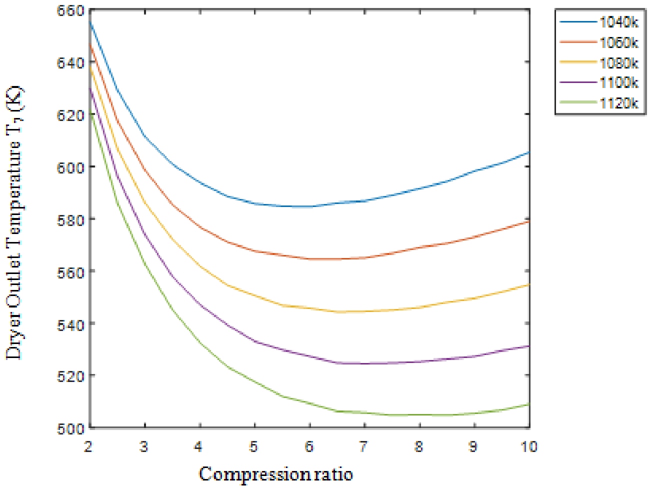

Fig.6: Curves of Dryer Outlet Temperature (T7) Evolution as a Function of Compression Ratio

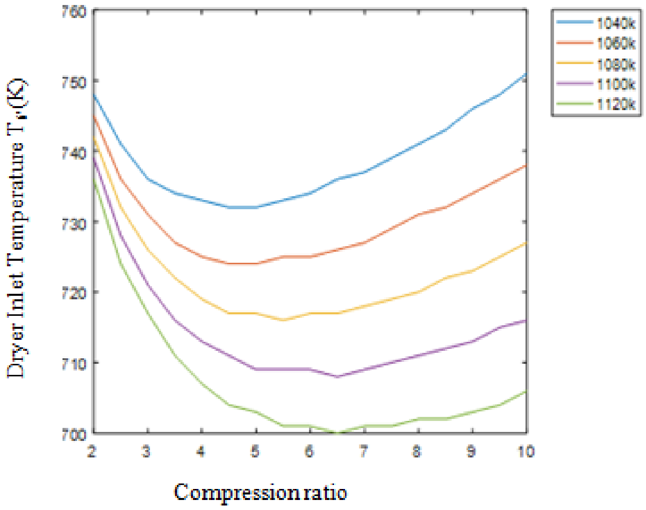

Fig.7: Curves of Dryer inlet Temperature (T6') Evolution as a Function of Compression Ratio

Initially, both curves decrease rapidly, reach a minimum, and then rise again. This trend reflects the nonlinear behavior of heat exchange between the exhaust gases and the moist wood. The passage through a minimum explains the reduction in overall efficiency observed from this point: the energy contained in the gases is recovered less effectively, which lowers drying performance. Critical flue gas temperatures are maintained regardless of compression ratio or turbine inlet temperature: T7 stays above the acid dew point to prevent corrosion, and T6′ remains above 400 °C to ensure efficient and continuous wood drying. These results demonstrate that, despite the efficiency drop observed near the minimum, the process remains thermodynamically viable and safe, while ensuring both drying quality and equipment protection.

Table III identifies the compression ratio that maximizes efficiency, τ = 8, for which the overall efficiency of the plant is 52.91%.

To validate the developed model, the results of the present study were compared with several reference studies available in the literature [21], [35]-[37].

Table IV highlights the performance of different case studies involving biomass-fired hot air turbine cogeneration systems. The discrepancies observed among the results are mainly attributed to the installed capacity, the type of biomass used, the operating conditions (turbine inlet temperature, compression ratio), as well as the selected simulation model. The net power output calculated in the present work is 500kW, which is significantly higher than the reported values ranging from 30 to 100 kW. This difference is essentially related to the design conditions. However, the turbine outlet temperature remains comparable to that reported in previous studies, with a value of 867 °C in this work versus 830-900 °C in the literature. Regarding electrical efficiency, the developed model yields 19.68%, which is close to the values obtained by Vera et *al.* [35]-[37] and Pantaleo et *al.* [38] but slightly lower than those reported by Iora and Silva [35] and Durante et *al.* [21], which reach 23.5% and 27.6%, respectively. In contrast, the thermal efficiency and overall cogeneration efficiency obtained (33.23% and 52.91%) fell within the range of reference studies, although some values, such as the overall efficiency of 83.6% reported by Vera et al., are higher due to specific operating conditions. These results confirm the consistency of the proposed model with previous works, while also highlighting the differences arising from calculation assumptions, the types of biomass employed, and operating parameters (compression ratio, flame temperature, and turbine characteristics). This comparison therefore validates the developed model and situates its performance within the range of those found in the broader scientific literature on biomass-fueled hot air turbine cogeneration systems.

Table I: Program results for T3=1140 K, T5=1192K, and Te=373K

τ	**$T_{6'}$ (K)**	**T_7 (K)**	η_{th}	η_{el}	η_{cog}	**m_{cog} (Kg/s)**
2,0	739,00	630,00	0,2091	0,1111	0,3202	0,5845
2,5	728,00	596,00	0,2494	0,1371	0,3866	0,4735
3,0	721,00	573,75	0,2752	0,1550	0,4301	0,4191
3,5	716,00	557,75	0,2931	0,1676	0,4607	0,3875
4,0	713,00	547,00	0,3053	0,1767	0,4820	0,3675
4,5	711,00	539,25	0,3141	0,1834	0,4975	0,3541
5,0	709,00	533,00	0,3202	0,1882	0,5084	0,345
5,5	709,00	529,75	0,3249	0,1917	0,5166	0,3388
6,0	709,00	527,25	0,3283	0,1941	0,5224	0,3346
6,5	708,00	524,75	0,3299	0,1956	0,5255	0,3319
7,0	709,00	524,50	0,3314	0,1965	0,5279	0,3304
7,5	710,00	524,75	0,3320	0,1969	0,5289	0,3298
8,0	**711,00**	**525,25**	**0,3323**	**0,1968**	**0,5291**	**0,3299**
8,5	712,00	526,25	0,3317	0,1964	0,5281	0,3307
9,0	713,00	527,25	0,3311	0,1956	0,5268	0,3319
9,5	715,00	529,50	0,3304	0,1946	0,5250	0,3336
10,0	716,00	531,25	0,3286	0,1934	0,5220	0,3357

Table IV: Performance of Hot Air Turbines in Biomass Cogeneration Units Compared with Modeling and Simulation Results from the Literature

	Present study	Iora and Silva [35]	Durante et *al.* [21]	Vera, Jurado, and Carpio [36]	Vera, Jurado, de Mena, et *al.* [37]	Pantaleo et *al.* [38]
w_{net} (kW)	500	72.7	98.82	70	30	77.54
$T_{\text{outlet turbine}}$ (C)	867	850	-	850	830	900
η_{el}	19.68	23.5	27.6	19.6	20.1	19.19
η_{th}	33.23	43	-	64	40.1	-
τ	8	5.37	5.5	4	4	-
η_{cog}	52.91	66.5	-	83.6	60.2	-
Type of biomass	eucalyptus	-	eucalyptus	olive residues	olive residues	biomass

V. CONCLUSION

Our study was designed as an analysis to assess the feasibility conditions of an industry adapted to the wood-energy sector in Algeria. To address this issue, we designed a pellet production unit with a capacity of 2 t/h, coupled with a cogeneration system to ensure self-consumption. The latter cogenerates an electrical power of 500 kW and thermal energy in the form of combustion flue gases at temperatures between 400 and 600 °C. The supply chain is fed with biomass from eucalyptus residues with 50% moisture content, collected from forests located in the northeast of Algeria (El Tarf).

The simulation carried out in MATLAB enabled the determination of the optimal operating parameters for each studied system, taking into account both thermodynamic conditions and performance constraints. This approach facilitated the parametric analysis of the cycles.

The analysis showed that if the air temperature at the boiler inlet exceeds 100 °C, an excess air ratio above 90% is required to keep the flame temperature below 1 200 K. Based on this, the parameters were set to α = 80% and Te = 100 °C, resulting in a flame temperature of 1 192 K (919 °C). The turbine inlet temperature T3 must remain below the flame temperature and was fixed at 1 140 K (867 °C). Once these parameters were defined, the compression ratio maximizing efficiency was determined to be about 8, yielding a cogeneration efficiency of 53% (electrical efficiency = 20%, thermal efficiency = 33%). Therefore, to produce 2 t/h of pellets at 10% moisture content, the unit requires 4.78 t/h of wood at 50% moisture content, of which 1.18 t/h is consumed by cogeneration, which achieves an overall efficiency of 53% (20% electrical and 33% thermal). The potential of the studied region would allow meeting the heating needs of up to 2 700–2 750 households, i.e., about 15 000 inhabitants (approximately 3.2% of the total population of the region).

This study highlights the potential of forestry residues as a renewable energy source to develop Algeria's wood-energy sector, particularly for pellet production, offering an eco-friendly alternative to fossil fuels. However, challenges such as sustainable biomass availability, forest fires, high moisture content, technical constraints, and economic costs must be addressed. Success depends on sound resource management, supportive policies, skilled workforce, and public acceptance. Careful planning is essential to ensure the long-term viability of biomass cogeneration and support Algeria's energy transition.

REFERENCES

[1] N. Arshed, M. Munir, et M. Iqbal, *"Sustainability assessment using STIRPAT approach to environmental quality: an extended panel data analysis", Environ Sci Pollut Res, vol. 28, no 14, p. 18163-18175, Apr. 2021, doi: 10.1007/s11356-020-12044-9.*

[2] S. F. Moosavian, Y. Noorollahi, et M. Shoaei, *"Renewable energy resources utilization planning for sustainable energy system development on a stand-alone island", Journal of Cleaner Production, vol. 439, p. 140892, Feb. 2024, doi: 10.1016/j.jclepro.2024.140892.*

[3] B. Bergougui, *"Moving toward environmental mitigation in Algeria: Asymmetric impact of fossil fuel energy, renewable energy and technological innovation on CO2 emissions", Energy Strategy Reviews, vol. 51, p. 101281, jan. 2024, doi: 10.1016/j.esr.2023.101281.*

[4] S. Haddoum, H. Bennour, and T. Ahmed Zaïd, *"Algerian Energy Policy: Perspectives, Barriers, and Missed Opportunities", Global Challenges, vol. 2, no 8, p. 1700134, 2018, doi: 10.1002/gch2.201700134.*

[5] P. Díaz-Cuevas, B. Haddad, et M. Fernandez-Nunez, *"Energy for the future: Planning and mapping renewable energy. The case of Algeria", Sustainable Energy Technologies and Assessments, vol. 47, p. 101445, oct. 2021, doi: 10.1016/j.seta.2021.101445.*

[6] *Ministry of energy and mining of Algeria, Le Programme des Energies et Renouvelables et de l'Efficacit´e Energetique, « Le Programme des Energies Renouvelables et de l'Efficacit´e Energetique ». Consulté le: Jul. 23, 2025.*

[7] T. Li et *al., "Performance analysis of an integrated biomass-to-energy system based on gasification and pyrolysis", Energy Conversion and Management, vol. 287, p. 117085, Jul. 2023, doi: 10.1016/j.enconman.2023.117085.*

[8] *[8] M. Mutascu, « Is biomass energy really sustainable in the United States? », Renewable and Sustainable Energy Reviews, vol. 181, p. 113325, juill. 2023, doi: 10.1016/j.rser.2023.113325.*

[9] M. Shahbaz, C. Raghutla, K. R. Chittedi, Z. Jiao, and X. V. Vo, *"The effect of renewable energy consumption on economic growth: Evidence from the renewable energy country attractive index", Energy, vol. 207, p. 118162, sept. 2020, doi: 10.1016/j.energy.2020.118162.*

[10] R. T. Baur, S. Tuedic, J. Promploy, and K. Kirasamutranon, *"Optimizing biomass pellet quality from sugarcane leaves and bamboo for sustainable biofuel production", Advances in Bamboo Science, vol. 11, p. 100153, mai 2025, doi: 10.1016/j.bamboo.2025.100153.*

[11] L. J. R. Nunes, M. Casau, M. F. Dias, J. C. O. Matias, and L. C. Teixeira, *"Agroforest woody residual biomass-to-energy supply chain analysis: Feasible and sustainable renewable resource exploitation for an alternative to fossil fuels", Results in Engineering, vol. 17, p. 101010, Mar. 2023, doi: 10.1016/j.rineng.2023.101010.*

[12] H. Tran, E. Juno, and S. Arunachalam, *"Emissions of wood pelletization and bioenergy use in the United States", Renewable Energy, vol. 219, p. 119536, Dec. 2023, doi: 10.1016/j.renene.2023.119536.*

[13] Y. Nie, X. Song, M. Shan, and X. Yang, *"Effect of pelletization on biomass thermal degradation in combustion: A case study of peanut shell and wood sawdust using macro-TGA", Energy and Built Environment, avr. 2024, doi: 10.1016/j.enbenv.2024.04.002.*

[14] C. Whittaker and I. Shield, *"Short rotation woody energy crop supply chains", in Biomass supply chains for bioenergy and biorefining, Elsevier, 2016, p. 217-248.*

[15] E. Monteiro, V. Mantha, and A. Rouboa, *"The Feasibility of Biomass Pellets Production in Portugal", Energy Sources, Part B: Economics, Planning, and Policy, vol. 8, no 1, p. 28-34, Jan. 2013, doi: 10.1080/15567249.2011.608414.*

[16] J. Gao et al., *"Site selection decision for biomass cogeneration projects from a sustainable perspective: A case study of China", Energy, vol. 286, p. 129518, Jan. 2024, doi: 10.1016/j.energy.2023.129518.*

[17] S. K. Ghosh, *"Biomass & Bio-waste Supply Chain Sustainability for Bio-energy and Bio-fuel Production", Procedia Environmental Sciences, vol. 31, p. 31-39, Jan. 2016, doi: 10.1016/j.proenv.2016.02.005.*

[18] G. Carraro, V. Bori, A. Lazzaretto, G. Toniato, and P. Danieli, *"Experimental investigation of an innovative biomass-fired micro-ORC system for cogeneration applications", Renewable Energy, vol. 161, p. 1226-1243, 2020.*

[19] A. Hamdi, M. Amouri, H. Bennour, T. Ahmed-Zaid, and R. Bouarab, *"Sizing of an organic rankine cycle cogeneration plant fueled with woody biomass: Application to an integrated wood pellet production unit", International Journal of Green Energy, p. 1-13, Jul. 2025, doi: 10.1080/15435075.2025.2530123.*

[20] K. A. Al-attab and Z. A. Zainal, *"Externally fired gas turbine technology: A review", Applied Energy, vol. 138, p. 474-487, Jan. 2015, doi: 10.1016/j.apenergy.2014.10.049.*

[21] A. Durante, G. Pena-Vergara, P. L. Curto-Risso, A. Medina, et A. Calvo Hernández, *"Thermodynamic simulation of a multi-step externally fired gas turbine powered by biomass", Energy Conversion and Management, vol. 140, p. 182-191, mai 2017, doi: 10.1016/j.enconman.2017.02.050.*

[22] T. K. Ibrahim et M. M. Rahman, *"Effect of compression ratio on the performance of different strategies for the gas turbine", International Journal of Automotive and Mechanical Engineering, vol. 9, p. 1747-1757, 2014.*

[23] E. D. Walker, N. F. Lee, C. Nica, A. Barnes, B. Graham, et K. Martin, *"Amplifying concerns: An exploration of community noise levels in rural communities impacted by wood pellet production", Environmental Challenges, vol. 17, p. 101024, Dec. 2024, doi: 10.1016/j.envc.2024.101024.*

[24] *Starmax Agri Solutions, BIOPELLET SYSTEM (2 tph), Turkey, offer, 2019.*

[25] E. Acuña, R. Rubilar, J. Cancino, T. J. Albaugh, and C. A. Maier, *"Economic assessment of Eucalyptus globulus short rotation energy crops under contrasting silvicultural intensities on marginal agricultural land", Land Use Policy, vol. 76, p. 329-337, Jul. 2018, doi: 10.1016/j.landusepol.2018.05.028.*

[26] G. Kewessa, T. Dejene, and P. Martín-Pinto, *"Soil fungal communities under plantations of different Eucalyptus species in Ethiopia: Insights for evidence-based management", Science of The Total Environment, vol. 982, p. 179663, Jun. 2025, doi: 10.1016/j.scitotenv.2025.179663.*

[27] T. Nussbaumer, *"Combustion and Co-combustion of Biomass: Fundamentals, Technologies, and Primary Measures for Emission Reduction", Energy Fuels, vol. 17, no 6, p. 1510-1521, Nov. 2003, doi: 10.1021/ef030031q.*

[28] C. Sheng and J. L. T. Azevedo, *"Estimating the higher heating value of biomass fuels from basic analysis data", Biomass and Bioenergy, vol. 28, no 5, p. 499-507, May 2005, doi: 10.1016/j.biombioe.2004.11.008.*

[29] J. M. Vargas-Moreno, A. J. Callejón-Ferre, J. Pérez-Alonso, et B. Velázquez-Martí, *"A review of the mathematical models for predicting the heating value of biomass materials", Renewable and Sustainable Energy Reviews, vol. 16, no 5, p. 3065-3083, Jun. 2012, doi: 10.1016/j.rser.2012.02.054.*

[30] V. Ganapathy, *Industrial boilers and heat recovery steam generators: design, applications, and calculations. CRC Press, 2002.*

[31] DGF, *"Plan de gestion de la wilaya d'El Tarf", Algerie, 2016.*

[32] R. Saidur, E. A. Abdelaziz, A. Demirbas, M. S. Hossain, and S. Mekhilef, *"A review on biomass as a fuel for boilers", Renewable and Sustainable Energy Reviews, vol. 15, no 5, p. 2262-2289, Jun. 2011, doi: 10.1016/j.rser.2011.02.015.*

[33] L. Keller and J.-P. Jaccoud, *"Température minimale des gaz de fumée dans les chauffages existants", No. 18, Aug. 1988, doi: 10.5169/SEALS-76830.*

[34] M. Terhan, *Prediction sulphuric acid and water vapour dew point temperatures of flue gases and combustion analysis for solid fuels in turkey", Journal of Thermal Engineering, vol. 7, no 2, p. 30-46, Feb. 2021, doi: 10.18186/thermal.867125.*

[35] P. Iora and P. Silva, *"Innovative combined heat and power system based on a double shaft intercooled externally fired gas cycle", Applied Energy, vol. 105, p. 108-115, May 2013, doi: 10.1016/j.apenergy.2012.11.059.*

[36] D. Vera, F. Jurado, and J. Carpio, *"Study of a downdraft gasifier and externally fired gas turbine for olive industry wastes", Fuel Processing Technology, vol. 92, no 10, p. 1970-1979, Oct. 2011, doi: 10.1016/j.fuproc.2011.05.017.*

[37] D. Vera, F. Jurado, B. de Mena, and G. Schories, *"Comparison between externally fired gas turbine and gasifier-gas turbine system for the olive oil industry", Energy, vol. 36, no 12, p. 6720-6730, Dec. 2011, doi: 10.1016/j.energy.2011.10.036.*

[38] A. M. Pantaleo, S. M. Camporeale, and N. Shah, *"Thermo-economic assessment of externally fired micro-gas turbine fired by natural gas and biomass: Applications in Italy", Energy Conversion and management, vol. 75, p. 202-213, 2013.*

Amel HAMDI is an engineer holding a master's degree in chemical engineering, awarded by the École Nationale Polytechnique, Algiers, in 2015. Since then, she has been pursuing a PhD at the École Nationale Polytechnique, Algiers, with a research focus on the energetic valorization of biomass. Her work has resulted in one published article and her active participation in two international conferences and one national seminar.

Mohamed AMOURI received the Engineer Diploma from Ibn Khaldoun University, Tiaret, and the Master's and PhD degrees from the École Nationale Polytechnique, Algiers, in 2012 and 2019, respectively. He is currently a researcher at the Centre de Développement des Énergies Renouvelables (CDER). His current research interests include biodiesel production, life cycle assessment, and microalgae cultivation.

Hocine BENNOUR is an assistant professor at the Mechanical Engineering Department (ENP, Algiers). He has been involved in teaching and research in thermodynamic cycles, Energy conversion and Turbomachinery

Toudert AHMED ZAID is Professor at the Chemical Engineering Department (ENP, Algiers). He has an experience of 20 years in the domain of surfactants and dispersed systems. He has authored or coauthored more than forty papers; mainly in this research area.

Rabah BOUARAB is Professor at the Chemical Engineering Department of Ecole Nationale Polytechnique, Algiers. He has an experience of 26 years in the field of hydrogen production. He has authored or co-authored more than 40 papers mainly in this research area.

Efficient Face Recognition Using Embedding-Based Distillation

Hana Remma, Chaimaa Ouarezki, Youcef Ouadjer, Mourad Adnane, and Sid-Ahmed Berrani

Abstract—Knowledge distillation (KD) facilitates the compression of large, high-performing neural networks into efficient student models, enabling deployment on resource-limited devices like mobile phones and IoT systems. This paper introduces a KD methodology, which involves training a student to capture a teacher's soft labels, intermediate feature representations, and ground truth labels, ensuring both compactness and accuracy. Applied to face recognition, our hybrid KD framework trains a MobileFaceNet student under an InceptionResNetV1 teacher, achieving 90.40% accuracy and a 96.25% AUC, outperforming lightweight models while remaining suitable for edge devices. These results highlight the potential of KD to enable robust, scalable face recognition solutions for real-world, resource-constrained environments.

***Keywords*—Face Recognition, Knowledge Distillation, Mobile devices, Efficient Deep learning.**

NOMENCLATURE

KD	Knowledge Distillation.
FAR	False Acceptance Rate.
FRR	False Rejection Rate.
EER	Equal Error Rate.
AUC	Area Under the Curve
ROC	Receiver Operating Characteristics

I. INTRODUCTION

Face recognition is a technology with numerous real-world applications, such as biometric authentication, video surveillance, and human-computer interaction. Recent advances in deep learning have led to high-performing models like ArcFace [1], CosFace [2], and MagFace [3], which achieve remarkable accuracy on large-scale benchmarks. However, these state-of-the-art (SOTA) models typically rely on deep architectures with hundreds of millions (100) of parameters and high computational complexity, making them unsuitable for deployment on resource-constrained devices such as smartphones, IoT nodes, and embedded systems.

To address this limitation, several strategies have been explored to reduce model size while preserving accuracy. Model compression techniques, including pruning [4] and quantization [5], aim to eliminate redundant weights or reduce numerical precision. While these methods significantly reduce storage and inference costs, they often require meticulous fine-tuning and may result in performance degradation, especially on challenging face recognition tasks. For example, the lightweight architecture of ShuffleFaceNet [6], constructs compact models from the ground up using depthwise separable convolutions or channel shuffling. These models offer faster inference and lower memory footprints but still fall short in recognition accuracy compared to their larger counterparts.

An alternative and increasingly popular direction is knowledge distillation (KD), initially introduced by Hinton et al. [7, 8], which transfers knowledge from a large teacher model to a smaller student. In the context of face recognition, KD has been applied to improve embedding quality by aligning student features with those of a pretrained teacher network.

In this paper, we propose a lightweight and effective face recognition framework that leverages a hybrid knowledge distillation approach. Our method enables a compact student model to be trained under the supervision of a pre-trained teacher network using both classification loss and embedding-based distillation loss. Unlike existing distillation methods that often require complex formulations or additional modules, our approach adopts a simple yet powerful dual-loss strategy that encourages the student to simultaneously learn identity labels and replicate the teacher's rich embedding space. This ensures that the student inherits both the discriminative capability and relational structure of the teacher, achieving a balance between compactness and accuracy suitable for on-device deployment. This paper is organized as follows: Section II. dives into the methodology of the proposed knowledge distillation framework. Section III. provides interpretation and discussion of the obtained results. Finally, section IV. concludes the paper with future directions.

II. METHODOLOGY

Knowledge distillation (KD) offers a robust set of benefits, making it a pivotal technique for model compression and deployment. It enables a compact model, often termed the student, with significantly reduced computational cost, to emulate the

Manuscript received July, 2025; revised December 28, 2025.

H. Remma, C. Ouarezki, and Y. Ouadjer are with the Electronics Department, Ecole Nationale Polytechnique, 10 Rue des Frères OUDEK, El Harrach 16200, Algiers, Algeria (e-mail: hana.remma@g.enp.edu.dz; chaimaa.ouarezki@g.enp.edu.dz; youcef.ouadjer@g.enp.edu.dz).

M. Adnane is with National Higher School of Autonomous Systems Technology, and LDCCP LAB, Ecole Nationale Polytechnique, 10 Rue des Frères OUDEK, El Harrach 16200, Algiers, Algeria (e-mail: mourad.adnane@g.enp.edu.dz).

S-A. Berrani is with National School of Artificial Intelligence, Route de Mahelma, 16201 Sidi Abdellah, Algiers, Algeria (email: sidahmed.berrani@ensia.edu.dz).

Digital Object Identifier (DOI): 10.53907/enpesj.v5i2.335

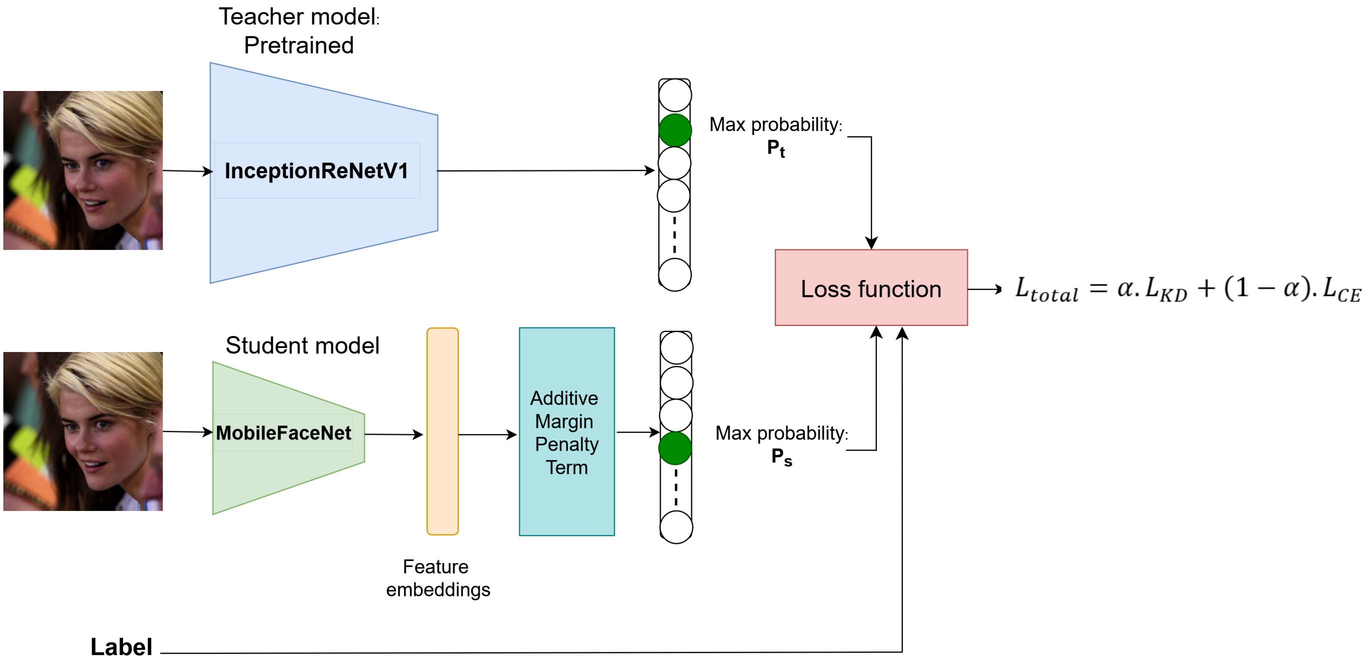

Fig. 1: Conceptual diagram of knowledge distillation, illustrating the teacher model (top) transferring soft labels to the student model (bottom), alongside ground truth labels shaping the total loss.

capabilities of a larger, high-performing teacher model, facilitating deployment on resource-constrained platforms such as mobile devices or IoT systems.

As illustrated in Figure 1, the InceptionResNetV1 [9] and MobileFaceNet [10] are used as teacher and student models respectively. The main advantage of using InceptionResnNetV1 is that it is trained on large publicly available datasets, and it encompasses general face feature representations. The MobileFaceNet on the othe hand is a compact deep neural network dedicated for facial recognition applications.

It is worth noting that the structure of InceptionResNetV1 and MobileFaceNet are different, the motivation for this difference is to enable knowledge transfer across diverse architectures, as evidenced by [11] and [12]. This flexibility allows tailoring student models to specific hardware or latency requirements while leveraging the teacher's expertise.

The proposed KD framework relies on three critical components: the teacher's soft labels, intermediate feature representations, and ground truth labels from the dataset. Drawing on foundational contributions by Hinton et al. [7] and Deng et al. [1], the following subsections detail the learning mechanisms, weaving mathematical precision with practical considerations.

A. *Soft Labels: Capturing Class Relationships*

The teacher, a deep neural network with significant capacity, produces soft labels-probability distributions over classes for each input that encode inter-class similarities. The distilled model often matches or surpasses the teacher's performance on specific tasks despite its smaller size. By learning softened probability distributions, the student can replicate nuanced patterns, offering more information than binary hard labels. The teacher's logits, $z_t = [z_{t,1}, \ldots, z_{t,C}]$, where C denotes the number of classes, are softened using a temperature parameter T:

$$P_{t,i} = \frac{\exp(z_{t,i}/T)}{\sum_{j=1}^{C} \exp(z_{t,j}/T)} \tag{1}$$

where $P_{t,i}$ is the softened probability for class i. Similarly to the teacher model, the student model produces soft-labels probability $P_{s,i}$ using its logits $z_s = [z_{s,1}, \ldots, z_{s,C}]$ to mimic teacher's output:

$$P_{s,i} = \frac{\exp(z_{s,i}/T)}{\sum_{j=1}^{C} \exp(z_{s,j}/T)} \tag{2}$$

To align these distributions, the student minimizes the Kullback-Leibler (KL) divergence, defining the distillation loss:

$$\mathcal{L}_{\text{KD}} = T^2 \sum_{i=1}^{C} P_{t,i} \log \frac{P_{t,i}}{P_{s,i}} \tag{3}$$

The T^2 scaling ensures the loss remains balanced for large T, enabling the student to internalize the teacher's generalizations, particularly for complex class boundaries [7].

By leveraging soft labels, KD enhances generalization capability of the student, and provides richer information than hard labels. These labels reveal class similarities, enabling the student to handle ambiguous inputs effectively. For example, a teacher assigning probabilities to "dog" and "wolf" guides the student toward nuanced patterns. Hinton et al. [7] showed KD-trained students outperform hard-label-trained models on complex datasets. Peng et al. [13] found that KD promotes smoother class distributions in remote sensing tasks, improving robustness to input variations.

B. Intermediate Feature Representations

Building on soft labels, and feature embeddings of the student, it is possible to learn robust intermediate representations. A method advanced by Deng et al. [1] in their ArcFace framework, proposed a highly discriminative face feature Alorithm, based on an additive angular margin penalty term m.

In this work we use the ArcFace additive angular margin penalty to enhance the discriminative power of deep features for face recognition. Given an input feature embedding vector $\mathbf{x_s} \in \mathbb{R}^d$, produced by the student model, and a weight vector $\mathbf{W}_i \in \mathbb{R}^d$ for class i, both are first normalized to compute the cosine similarity as $\cos(\theta_i) = \frac{\mathbf{x}^\top \mathbf{W}_i}{\|\mathbf{x}\|\|\mathbf{W}_i\|}$. For the ground-truth class y, an angular margin m is added in the cosine space, modifying the similarity as:

$$\cos(\theta_y + m) = \cos(\theta_y)\cos(m) - \sqrt{1 - \cos^2(\theta_y)}\sin(m) \quad (4)$$

Finally the student logits are scaled by a factor s, based on:

$$\mathrm{z}_{s,i} = \begin{cases} s \cdot \cos(\theta_y + m), & \text{if } i = y \\ s \cdot \cos(\theta_i), & \text{otherwise} \end{cases} \quad (5)$$

This formulation effectively increases the angular margin between classes in the normalized hypersphere, leading to improved inter-class separability and intra-class compactness.

C. Ground Truth Labels

To ensure task-specific accuracy, the student is trained on ground truth labels via cross-entropy loss:

$$\mathcal{L}_{\text{CE}} = -\sum_{i=1}^{C} y_i \log(P_{s,i}) \quad (6)$$

where y_i is the one-hot ground truth label, and $P_{s,i}$ is the student's probability (with $T = 1$). This loss anchors the student's predictions to the dataset, balancing the teacher's influence with direct task learning [7].

D. Combined Objective

The student's training optimizes a composite loss:

$$\mathcal{L}_{\text{total}} = \alpha \cdot \mathcal{L}_{\text{KD}} + (1 - \alpha) \cdot \mathcal{L}_{\text{CE}} \quad (7)$$

where $\alpha \in [0, 1]$ balances distillation and cross-entropy losses. Typical values include $\alpha = 0.5\text{˘}0.9$, $T = 2\text{˘}10$. This balance is often an empirical, enabling the student to synthesize teacher insights and ground truth effectively [7, 11, 12, 14]. These hyperparameters require careful tuning, often through validation, to reconcile objectives like teacher mimicry and task fidelity.

E. Experimental Setup

Our facial recognition system is based on the MobileFaceNet (student model), trained through knowledge distillation from a high-capacity InceptionResNetV1 (teacher model). Training was conducted using the Adam optimizer with a learning rate of 0.01 and weight decay of 10^{-4}.

While teacher training is resource-intensive, KD limits this cost to the student pre-training phase. The student requires minimal resources for fine-tuning or deployment, reducing production expenses.

In this work, we used the Labeled Faces in the Wild (LFW) dataset [15], to pre-train and evaluate the MobileFaceNet model. The LFW is a well established and commonly used dataset to evaluate face recognition models. It contains over 13 000 images of faces, with 5 749 identities, collected from the web, with three different splits: train, evaluation and test sets.

III. RESULTS AND DISCUSSION

This section presents the results. First, a description of the evaluation metrics is given. Then, results are presented with an in-depth discussion. Finally, a comparison of the obtained results with MobileFaceNet against state-of-the-art models is presented.

A. Evaluation Metrics

We evaluated performance using the following standard metrics:

- **Accuracy** (%): Percentage of correctly classified pairs.
- **FAR False Acceptance Rate (%):** refers to the impostor accepted as genuine.
- **FRR False Rejection Rate (%):** is the genuine rejected as impostor.
- **EER Equal Error Rate (%):** is the point where FAR = FRR.
- **AUC (%):** Area Under the Receiver Operating Characteristics (ROC) Curve.

B. Obtained Results

Table. I

EXPERIMENTAL RESULTS OF THE PROPOSED METHOD

Accuracy (%)	FAR (%)	FRR (%)	EER (%)	AUC (%)
90.40	**0.87**	**18.33**	**18.66**	**96.25**

The experimental results illustrated in Table I, highlight the effectiveness of the proposed KD approach in training a lightweight face recognition model with high performance and low computational cost. The MobileFaceNet student achieved a top-1 accuracy of 90.4%, an AUC of 96.25% (Figure 2), and a FAR of 0.87%, demonstrating its capability to inherit rich representations from the InceptionResNetV1 teacher, which enhances generalization and avoids overfitting typical of smaller models trained from scratch.

This approach is highly practical for resource-constrained devices. The low FAR underscores the robustness of the learned embeddings, critical for security applications like biometric authentication, surpassing lightweight alternatives with less discriminative features. However, the high FRR and EER (around 18%) indicate a limitation, likely due to dataset biases or insufficient feature diversity in the student model. To reduce FRR and EER it is possible to explore the hyperparameter space by tuning T, α, and the learning rate with advanced regularization like dropout, batch normalization and early stopping. Overall, this method balances performance and efficiency, offering a scalable solution for real-world face recognition.

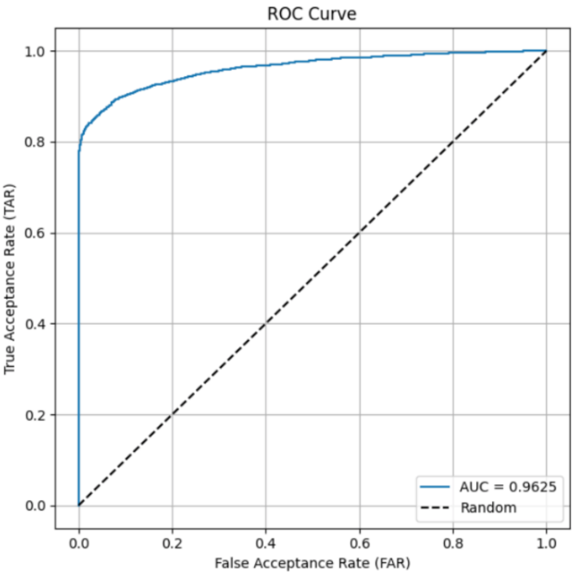

Fig. 2: ROC curve of MobileFaceNet trained via knowledge distillation.

C. *Comparison with State-of-the-Art Models*

Table. II
COMPARISON WITH LIGHTWEIGHT AND HEAVYWEIGHT SOTA MODELS

Model	Accuracy (%)	# of parameters (M)
Pyramid CNN [16]	85.5	-
DCMN [17]	90.00	0.5
ArcFace (ResNet50) [1]	98.2	23.5
CosFace (ResNet101) [2]	98.1	44.5
Ours (MobileFaceNet)	**90.4**	**0.99**

The distilled MobileFaceNet model is compared to state-of-the-art models in terms of accuracy, and number of trainable parameters in millions (M). Results are depicted in Table II. Compared to Pyramid CNN [16] and DMCN [17] models, our approach shows clear improvements in accuracy, making it suitable for embedded systems. While heavyweight models such as ArcFace [1] (23.5M) and CosFace [2] (44.5M) outperform ours in raw accuracy, they require significantly more computational resources, making them less practical for edge devices.

IV. CONCLUSION

In this work we demonstrated the efficacy of knowledge distillation (KD) in crafting efficient, high-performing models for face recognition, with broad implications for resource-constrained applications such as smartphone devices. Our hybrid KD approach, employing MobileFaceNet as the student model under an InceptionResNetV1 teacher, achieves 90.40% accuracy and 96.25% AUC, outperforming lightweight models while remaining viable for edge deployment. The methodology integrates soft labels, feature alignments, and ground truth learning, ensuring the student captures the teacher's nuanced knowledge, as evidenced by a robust False Acceptance Rate of 0.87%. Our appraoch has the advantages of computational efficiency, cross-architecture versatility, and it is tailored for real-time applications like biometric authentication and IoT systems.

The elevated False Rejection Rate suggests refinement opportunities, with future research exploring multi-teacher or self-distillation by leveraging an ensemble of teacher models that combine their knowledge into a single student, merging diverse strengths.

REFERENCES

[1] J. Deng, J. Guo, N. Xue, and S. Zafeiriou, "Arcface: Additive angular margin loss for deep face recognition," in *IEEE/CVF Conference on Computer Vision and Pattern Recognition (CVPR)*, (Long Beach, CA, USA), pp. 4685–4694, 2019.

[2] H. Wang, Y. Wang, Z. Zhou, X. Ji, D. Gong, J. Zhou, Z. Li, and W. Liu, "Cosface: Large margin cosine loss for deep face recognition," in *IEEE/CVF Conference on Computer Vision and Pattern Recognition (CVPR)*, (Salt Lake City, UT, USA), pp. 5265–5274, 2018.

[3] Q. Meng, S. Zhao, Z. Huang, and F. Zhou, "Magface: A universal representation for face recognition and quality assessment," in *IEEE/CVF Conference on Computer Vision and Pattern Recognition (CVPR)*, (Virtual Event), pp. 14220–14229, 2021.

[4] H. Cheng, M. Zhang, and J. Q. Shi, "A survey on deep neural network pruning: Taxonomy, comparison, analysis, and recommendations," *IEEE Transactions on Pattern Analysis and Machine Intelligence*, vol. 46, no. 12, pp. 10558–10578, 2024.

[5] A. Gholami, S. Kim, Z. Dong, Z. Yao, M. W. Mahoney, and K. Keutzer, "A survey of quantization methods for efficient neural network inference," 2021.

[6] Y. Martinez-Diaz, L. S. Luevano, H. Mendez-Vazquez, M. Nicolas-Diaz, L. Chang, and M. Gonzalez-Mendoza, "Shufflefacenet: A lightweight face architecture for efficient and highly-accurate face recognition," in *IEEE/CVF International Conference on Computer Vision Workshops (ICCVW)*, (Seoul, South Korea), pp. 2721–2728, 2019.

[7] G. Hinton, O. Vinyals, and J. Dean, "Distilling the knowledge in a neural network," in *Neural Information Processing Systems (NeurIPS) Deep Learning Workshop*, (Montreal, QC, Canada), 2015.

[8] L. Wang and K.-J. Yoon, "Knowledge distillation and student-teacher learning for visual intelligence: A review and new outlooks," *IEEE Transactions on Pattern Analysis and Machine Intelligence*, vol. 44, no. 6, pp. 3048–3068, 2022.

[9] C. Szegedy, S. Ioffe, V. Vanhoucke, and A. Alemi, "Inception-v4, inception-resnet and the impact of residual connections on learning," 2016.

[10] S. Chen, Y. Liu, X. Gao, and Z. Han, "Mobilefacenets: Efficient cnns for accurate real-time face verification on mobile devices," 2018.

[11] A. Romero, N. Ballas, S. Ebrahimi Kahou, A. Chassang, C. Gatta, and Y. Bengio, "Fitnets: Hints for thin deep nets," in *International Conference on Learning Representations (ICLR)*, (San Diego, CA, USA), 2015.

[12] S. Zagoruyko and N. Komodakis, "Paying more attention to attention: Improving the performance of convolutional neural networks via attention transfer," 2017.

[13] X. Peng, J. Zhou, and X. Wu, "Distillation-based cross-model transferable adversarial attack for remote sensing image classification," *Remote Sensing*, vol. 17, no. 10, 2025.

[14] F. Tung and G. Mori, "Similarity-preserving knowledge distillation," in *Proceedings of the IEEE/CVF International Conference on Computer Vision (ICCV)*, (Seoul, South Korea), 2019.

[15] G. B. Huang, M. Mattar, T. Berg, and E. Learned-Miller, "Labeled faces in the wild: A database for studying face recognition in unconstrained environments," in *ECCV Workshop on Faces in Real-Life*, (Marseille, France), 2008.

[16] H. Fan, Z. Cao, Y. Jiang, Q. Yin, and C. Doudou, "Learning deep face representation," 2014.

[17] W. Deng, J. Hu, N. Zhang, B. Chen, and J. Guo, "Fine-grained face verification: Fglfw database, baselines, and human-dcmn partnership," *Pattern Recognition*, vol. 66, pp. 63–73, 2017.

Hana Remma

She is currently pursuing a degree in Electronics as a State Engineer at the École Nationale Polytechnique in Algiers, Algeria. Her academic interests include machine learning, image processing, and embedded systems. This paper represents her first contribution to scientific research.

Chaimaa Ouarezki

She is currently a fourth-year student in electronics at the École Nationale Polytechnique in Algeria. Her academic journey is centered on developing a solid foundation in electronics. She is particularly interested in biomedical engineering, robotics, and image processing, where she seeks to apply machine learning techniques to solve real-world problems.

Youcef Ouadjer

Received the Master of science degree in Biomedical and Electrical Engineering, from University of Mouloud Mammeri, Tizi Ouzou, Algeria, in 2017. He is currently pusrsuing the Ph.D. degree with Department of Electronics, Ecole Nationale Polytechnique. His research interests include soft biometrics, data engineering, applied machine learning.

Mourad Adnane

Mourad Adnane received his Engineering degree in Electronics in 2003 from USTHB, Algiers, Algeria, and earned a Ph.D. in System Design Engineering in 2009 from Yamaguchi University, Japan. He is currently a professor at the National Higher School of Autonomous Systems Technology and leads the Embedded Systems team within the LDCCP Laboratory at École Nationale Polytechnique. His research interests include instrumentation, signal processing, pattern recognition, and machine learning, with a particular focus on applications in biomedical engineering.

Sid-Ahmed Berrani

Is a Professor in Computer Science at the National High School of Artificial Intelligence in Sidi-Abdallah, Algeria. He obtained an engineering degree in computer science from the University of Sidi Bel-Abbès (Algeria) in 2000 and a Ph.D. degree in computer science from the University of Rennes 1 in 2004. He has been a researcher at Orange Labs in France, the head the Multimedia Content Analysis and Indexing R&D unit of Orange Labs, and an associate professor at École Nationale Polytechnique (Algiers). His research activities focus on image and video indexing, machine learning, multidimensional data analysis and Artificial Intelligence. He has authored or co-authored over fifty scientific publications and has filed 13 patents

Advanced Control of Shunt Active Power Filter based on Flying Capacitor Multicellular Inverter using Backstepping and PS-PWM

Kheira Hemici and Mohand Oulhadj Mahmoudi

Abstract−This paper presents an advanced nonlinear control strategy for a Shunt Active Power Filter (SAPF) utilizing a Flying Capacitor Multicellular Inverter (FCMLI) to improve power quality in electrical distribution systems. The proposed control is based on the Backstepping technique, known for its ability to handle nonlinear system dynamics and guarantee global stability. To ensure efficient inverter operation and capacitor voltage balancing, Phase-Shifted Pulse Width Modulation (PS-PWM) is employed. The effectiveness of the proposed Backstepping controller is evaluated against a traditional Proportional-Integral (PI) controller. Simulation results demonstrate that the proposed method outperforms the conventional PI controller in terms of total harmonic distortion (THD), transient response, and capacitor voltage balance.

***Keywords*−Shunt active power filter, flying capacitor multicellular inverter, backstepping control, harmonic mitigation.**

NOMENCLATURE

SAPF	Shunt Active Power Filter
FCMLI	Flying Capacitor Multicellular Inverter
PS-PWM	Phase-Shifted Pulse Width Modulation
PI	Proportional-Integral
BC	Backstepping Controller
THD	Total Harmonic Distortion
RMS	Root Mean Square
PCC	Point of Common Coupling
SRF	Synchronous Reference Frame

I. INTRODUCTION

Power quality has become a major concern due to the proliferation of nonlinear loads in modern electrical grids. Shunt Active Power Filters (SAPFs) are widely employed to compensate for current harmonics and reactive power [1]- [3]. The integration of multilevel inverters, particularly Flying Capacitor Multicellular Inverters (FCMLIs), into SAPFs provides additional benefits such as reduced switching losses, improved voltage quality and modularity. Numerous researchers have explored and tested a variety of control methodologies tailored to FCMLI-based SAPFs [4]-[11]. These strategies aim to enhance the dynamic performance, efficiency, and reliability of the system while ensuring compliance with stringent power quality standards.

The multilevel structure of FCMLIs provides significant advantages, such as reduced harmonic distortion, improved voltage waveforms, and greater flexibility in voltage control. However, FCMIs introduce complexities in control due to the floating nature of their capacitors and the need for voltage balancing [12]-[14]. Traditional control strategies like PI controllers often fail to maintain performance under varying load conditions or dynamic disturbances. To address these limitations, this study proposes a nonlinear Backstepping control scheme integrated with PS-PWM, providing improved harmonic mitigation and capacitor voltage regulation.

Backstepping is a powerful recursive design methodology that systematically builds a robust nonlinear control law, guaranteeing global asymptotic stability for systems in strict feedback form [15]-[17]. This method is especially well-suited for complex power electronic converters because it explicitly accounts for the system's nonlinearities. Consequently, it delivers superior dynamic performance, disturbance rejection, and accurate tracking compared to conventional linear control approaches.

Our numerical simulations clearly demonstrate the effectiveness of this proposed backstepping-based control strategy in achieving the outlined control goals, ensuring stable operation, optimal performance, precise flying capacitor voltage balancing, and effective harmonic current compensation. This paper is organized as follows: Section II details the mathematical model of the SAPF-FCMLI in the d-q reference frame; Section III discusses the proposed backstepping controller synthesis; Section IV presents the simulation results and their interpretation; Section V concludes the paper II

II. MATHEMATICAL MODEL OF THE SAPF-FCMLI IN THE D-Q REFERENCE FRAME

In this section, the topology of the three-phase SAPF FCMLI is presented, along with its mathematical model in both α−β and d−q phase coordinates. The control of flying capacitor voltage is discussed, and the algorithm for generating the reference current is described.

Manuscript received September 17, 2025; revised November 2, 2025.

K. Hemici and M.O. Mahmoudi are with the Laboratory of Control Process, Ecole Nationale Polytechnique (ENP), B.P. 182 El Harrach, Algiers 16200, Algeria (e-mail: k.hemici@univ-chlef.dz, mo.mahmoudi@g.enp.edu.dz).

Digital Object Identifier (DOI): 10.53907/enpesj.v5i2.338

Fig. 1 illustrates the schematic layout of a four-level Shunt Active Power Filter utilizing a Flying Capacitor Multilevel Inverter (SAPF-FCMLI). This system is engineered to suppress harmonic currents and compensate for reactive power arising from nonlinear loads. In the presented study, the nonlinear load takes the form of a three-phase diode rectifier, which is known to generate considerable current harmonics.

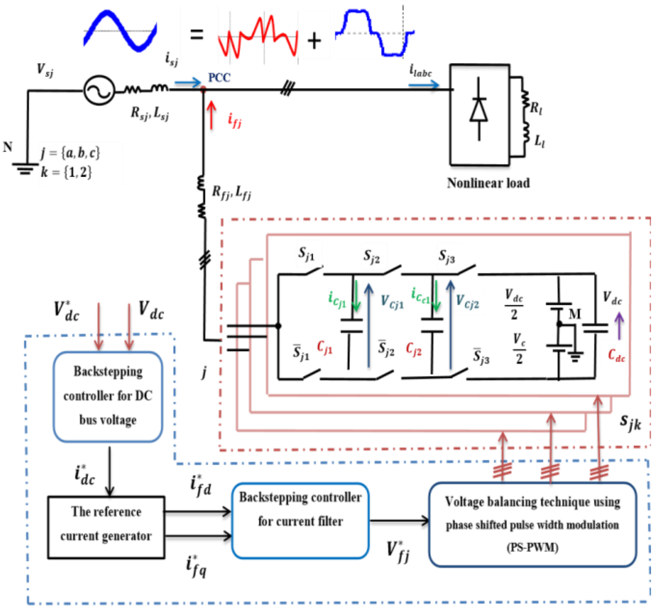

Fig. 1: Three phases SAPF based on Flying Capacitor Multicellular Inverter system.

The SAPF-FCMLI effectively addresses these power quality issues by injecting appropriate compensation currents. As a result, the mains currents remain nearly sinusoidal, even when subjected to nonlinear loading conditions, thereby improving overall power quality and ensuring stable, high-quality source currents.

The FCMLI utilizes two DC-bus capacitors to effectively stabilize the DC bus voltage. The SAPF-FCMLI is connected to the distribution system at a Point of Common Coupling (PCC) through an $(L_{f,j}, R_{f,j})$ coupling filter. The differential equations describing the dynamic model of the three-phase SAPF-FCMLI are defined in $(\alpha\beta)$ axes, as given in Eq. (1).

$$\frac{d}{dt}\begin{pmatrix} i_{f\alpha} \\ i_{f\beta} \end{pmatrix} = \frac{1}{L_f}\begin{pmatrix} v_{s\alpha} - v_{f\alpha} - R_f i_{f\alpha} \\ v_{s\beta} - v_{f\beta} - R_f i_{f\beta} \end{pmatrix} \qquad (1)$$

The dynamical model of the system in dq reference frame results in Eq. (2) as follows [18]:

$$\frac{d}{dt}\begin{pmatrix} i_{fd} \\ i_{fq} \end{pmatrix} = \frac{1}{L_f}\begin{pmatrix} v_{fd} - v_{sd} - R_f i_{fd} + \omega L_f i_{fq} \\ v_{fq} - v_{sq} - R_f i_{fq} + \omega L_f i_{fd} \end{pmatrix} \qquad (2)$$

According to the Equation (2), the mathematical model of proposed topology three-phase SAPF-FCMLI can be expressed as follows [19]

$$\dot{x} = Ax + Bu + G \qquad (3)$$

Equation (3) presents the general state-space form, where x is a state vector (i.e., $[i_{fd}, i_{fq}]^{T}$), $\dot{x}$ is the reference vector, and u is the input vector (i.e., $[v_{fd}, v_{fq}]^{T}$). Matrix A, B and G can be expressed as follows:

$$A = \begin{bmatrix} -\frac{R_f}{L_f} & -\omega \\ \omega & -\frac{R_f}{L_f} \end{bmatrix}, B = \begin{bmatrix} \frac{1}{L_f} \\ \frac{1}{L_f} \end{bmatrix}, G = \begin{bmatrix} -\frac{v_{sd}}{L_f} \\ -\frac{v_{sq}}{L_f} \end{bmatrix}$$

G represents external perturbations, such as source voltage variations.

The model presented in (2) describes the interaction between the active filter connected to the PCC and the AC power system in dq coordinates. The mathematical model helps to identify the control inputs, as well as the state and input variables. The model has two inverter currents (i_{fd}, i_{fq}), the control inputs (u_{fd}, u_{fq}) are related to the control signal s_{jk}; and the input voltages at the PCC (v_{sd}, vsq) are treated as external perturbations to the system.

The SAPF injects harmonic currents in opposition to those generated by the nonlinear load. The Synchronous Reference Frame (SRF) method transforms load currents from the $\alpha\beta$ frame to the dq frame to separate harmonic components from the fundamental [11],[20]. This method performs robustly even under non-ideal grid conditions. Fig. 2 presents the block diagram of this extraction method.

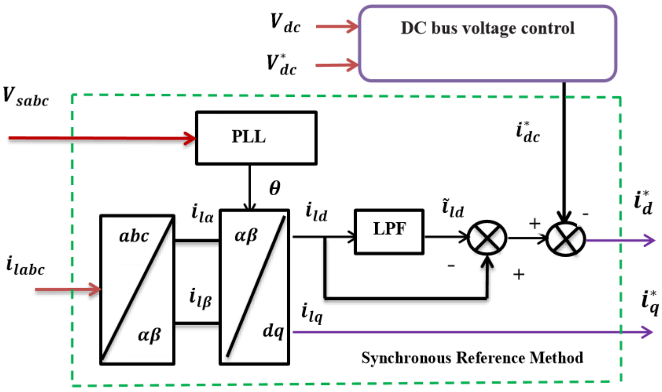

Fig. 2: Block diagram for extracting reference currents under the dq frame.

III. PROPOSED BACKSTOPPING CONTROL

The principle of the backstepping controller involves systematically constructing a control law in an iterative manner. During this process, certain components of the system's state representation are treated as "virtual controls," for which intermediate control laws are progressively developed [21]. This methodology inherently incorporates the concept of Lyapunov stability, ensuring that a chosen Lyapunov function remains positive definite while its time derivative is consistently negative definite. This rigorous approach allows the system to be decomposed into a series of nested subsystems of decreasing order. At each successive step, the order of the system is effectively increased, and the stabilization of the previously unstable parts is addressed, culminating in the derivation of the final control law in the last step. This iterative procedure always guarantees the overall asymptotic stability of the system.

A. *Control synthesis by backstepping for DC bus voltage*

The DC side of the SAPF-FCMLI can be expressed as:

$$\frac{dV_{dc}}{dt} = \frac{i_{dc}}{C_{dc}} \qquad (4)$$

To maintain the DC bus capacitor voltage at a constant desired value, a Backstepping controller is employed for its regulation. The primary objective of this control loop is to generate the power reference at the DC bus capacitor terminal.

The tracking error variable for the DC bus voltage e_{Vdc} is defined as follows:

$$e_{V_{dc}} = V_{dc}^{*} - V_{dc} \quad (5)$$

Its derivative is as follows:

$$\dot{e_{V_{dc}}} = \frac{dV_{dc}^{*}}{dt} + \frac{dV_{dc}}{dt} \quad (6)$$

Substituting $\dot{V_{dc}}$ from (4) into (6) yields:

$$\dot{e_{V_{dc}}} = \dot{V_{dc}} + \frac{i_{dc}}{C_{dc}} \quad (7)$$

To proceed with the Backstepping design, we choose a Lyapunov function V_{L1} as follows:

$$V_{L1} = \frac{1}{2}\, e_{V_{dc}}^{2} \quad (8)$$

The derivative of V_{L1} with respect to time is given by:

$$\dot{V_{L1}} = e_{V_{dc}} \dot{e_{V_{dc}}} = e_{V_{dc}} \left(\dot{V_{dc}^{*}} - \frac{i_{dc}^{*}}{C} \right) \quad (9)$$

Lyapunov function must be negative ($\dot{V_{L1}}<0$) this can be achieved by choosing the derivative of the error $eVdc$ to be:

$$\dot{e_{V_{dc}}} = -K_1\, e_{V_{dc}} \quad (10)$$

in which, K_1 is a positive gain ($K_1>0$).

From equations (7) and (10) we find:

$$i_{dc}^{*} = C_{dc}\left(\dot{V_{dc}^{*}} - K_1\, e_{V_{dc}} \right) \quad (11)$$

In this case, the reference voltage V_{dc}^{*} is chosen as a constant, so its derivative $\dot{V_{dc}^{*}}$will be zero. To guarantee the Lyapunov stability, the control law is chosen as:

$$i_{dc}^{*} = C_{dc} K_1\, e_{V_{dc}} \quad (12)$$

Therefore, the control law can be written as given by Eq. (12).

B. Control synthesis by backstepping for current filter

The dynamic equations of the system in the dq reference frame are given by system (2), while the tracking errors for the dq axis currents, e_{id} and e_{iq}, are defined as follows:

$$\begin{cases} e_{i_d} = i_{f_d}^{*} - i_{f_d} \\ e_{i_q} = i_{f_q}^{*} - i_{f_q} \end{cases} \quad (13)$$

Their derivatives are:

$$\begin{cases} \dot{e_{i_d}} = \dot{i_{f_d}^{*}} - \dot{i_{f_d}} \\ \dot{e_{i_q}} = \dot{i_{f_q}^{*}} - \dot{i_{f_q}} \end{cases} \quad (14)$$

From system (2), the derivatives of the filter currents $\dot{i_{f_d}}$ and $\dot{i_{f_q}}$ are as follows:

$$\begin{cases} \dot{i_{f_d}} = \frac{1}{L_f}\left(v_{fd} - v_{sd} - R_f i_{fd} + \omega L_f i_{fq} \right) \\ \dot{i_{f_q}} = \frac{1}{L_f}\left(v_{fq} - v_{sq} - R_f i_{fq} + \omega L_f i_{fd} \right) \end{cases} \quad (15)$$

The Lyapunov function for this subsystem is chosen as:

$$V_{L2} = \frac{1}{2}\, e_{i_d}^{2} + \frac{1}{2}\, e_{i_q}^{2} \quad (16)$$

The derivative of V_{L2} with respect to time is given by:

$$\dot{V_{L2}} = e_{i_d} \dot{e_{i_d}} + e_{i_q} \dot{e_{i_q}} \quad (17)$$

To ensure the stability of the system, the derivative of the Lyapunov function must be negative $\dot{V}\,L2$ must be negative. This can be achieved by choosing $\ddot{e}id$ and $\ddot{e}iq$ as:

$$\begin{cases} \dot{e_{i_d}} = K_2 e_{i_d} \\ \dot{e_{i_q}} = K_3 e_{i_q} \end{cases} \quad (18)$$

where, K_2 and K_3 are positive gains ($K_2>0$, $K_3>0$).

Substituting $\dot{e_{i_d}}$ and $\dot{e_{i_q}}$ from (14) into (18) and then substituting $\ddot{i}fd\ \dot{*}$ and $\ddot{i}fq\ \dot{*}$ from (15), we derive the expressions for the control inputs vfd and vfq. For example, from the first part of (18) and (14):

$$\dot{i_{f_d}} - \frac{1}{L_f}\left(v_{fd} - v_{sd} - R_f i_{fd} + \omega L_f i_{fq} \right) = -K_2 e_{i_d} \quad (19)$$

Rearranging to solve for v_{fd}, it yields:

$$v_{fd} = v_{sd} - R_f i_{fd} + \omega L_f i_{fq} + L_f\left(\dot{i_{f_d}} - K_2 e_{i_d} \right) \quad (20)$$

Similarly, for v_{fq}, it follows

$$v_{fq} = v_{sq} - R_f i_{fq} + \omega L_f i_{fd} + L_f\left(\dot{i_{f_q}} - K_3 e_{i_q} \right) \quad (21)$$

Therefore, the final control law for the filter voltages v_{fd} and v_{fq} can be written as:

$$\begin{cases} v_{fd} = v_{sd} - R_f i_{fd} + \omega L_f i_{fq} + L_f\left(\dot{i_{f_d}^{*}} - i_{f_d} \right) \\ v_{fq} = v_{sq} - R_f i_{fq} + \omega L_f i_{fd} + L_f\left(\dot{i_{f_q}^{*}} - i_{f_q} \right) \end{cases} \quad (22)$$

To ensure Lyapunov stability, the control law is given by Equation (19). Flying Capacitor Voltage Balancing using PS-PWM we propose voltage-balancing dynamic in FCMLI using phase shifted pulse width modulation (PS-PWM). We specialize in the case three-cell inverter which represents four-level FCMLI (p=3), the control law balances the flying capacitor voltages to the defined values ($v_{Cj1}^{*} = \frac{V_{dc}}{3}$; $v_{Cj2}^{*} = 2\frac{V_{dc}}{3}$) [11]. The FCMLI employs phase-shifted pulse width modulation for voltage balancing [22, 23]. The voltage balancing dynamics are governed by:

$$\begin{cases} \frac{dV_{Cj1}}{dt} = \frac{1}{C}\left(d_{j2} - d_{j1} \right) i_{f_j} \\ \frac{dV_{Cj2}}{dt} = \frac{1}{C}\left(d_{j3} - d_{j2} \right) i_{f_j} \end{cases} \quad (23)$$

There are two values for the switch control functions. s_{jk}= {0,1}, meaning "1" and "0" that the switch is on and off respectively. The switch pairs in each phase function in a complementary manner s_{j1}, $\overline{s_{j1}}$, s_{j2}, $\overline{s_{j2}}$, and s_{j3}, $\overline{s_{j3}}$,. The line-to-ground voltage V_{Mj} and the currents through the flying capacitors (i_{Cj1}, i_{Cj2}) can be written using Kirchhoff's laws as:

$$V_{Mj} = (s_{j1} - s_{j2})V_{cj1} + (s_{j2} - s_{j3})V_{cj2} + s_{j3}\frac{V_{dc}}{2} - \frac{V_{dc}}{2} \quad (24)$$

From the preceding equations, we deduce that the current flowing through a capacitor is governed by the control signals linked to two consecutive switches within a switching period. The local-average representation of the capacitor current can be expressed as:

$$\begin{cases} \overline{i_{Cj1}} = (d_{j2} - d_{j1})\overline{i_{f_j}} \\ \overline{i_{Cj2}} = (d_{j3} - d_{j2})\overline{i_{f_j}} \end{cases} \quad (25)$$

Where, $\overline{i_{Cj1}}$ and $\overline{i_{Cj2}}$ are the locally averaged currents of the capacitor d_{j3}, d_{j2} and d_{j1} are the duty cycles of the switch s_{j3}, s_{j2} and s_{j1}, respectively. The duty cycles are modified using proportional control:

$$\begin{cases} d_{j1} = V_{fj}^* + sign(i_{fj})\left(-(V_{cj1}^* - V_{cj1})\right)k_p \\ d_{j2} = V_{fj}^* + sign(i_{fj})\left((V_{cj1}^* - V_{cj1}) - (V_{cj2}^* - V_{cj2})\right)k_p \\ d_{j3} = V_{fj}^* + sign(i_{fj})\left(-(V_{cj2}^* - V_{cj2})\right)k_p \end{cases} \quad (26)$$

Figure 3 shows the diagram of the voltage balancing technique for generation of the functions of the switches s_{jk} [11].

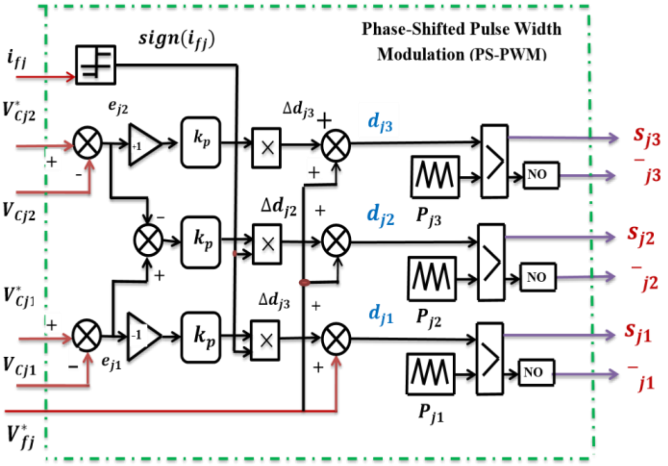

Fig. 3: Block diagram of the voltage balancing technique for four-level multicellular inverter using Phase-Shifted Pulse Width Modulation (PSPWM).

IV. RESULTS AND DISCUSSION

The SAPF-FCMLI and its backstepping controller were implemented in MATLAB using the Power Systems Toolbox. The nonlinear load is a three-phase diode rectifier. System parameters are given in Table I.

Table. I
PARAMETERS VALUES OF THE SIMULATED SYSTEM [6]

PARAMETER	VALUE
Supply voltage and frequency	220V, 50 Hz
Supply impedance	1 mΩ, 1 mH
Load impedance	10 Ω, 10 mH
Coupling Filter	1 mΩ, 1 mH
DC bus voltage	800 V
DC bus capacitance	5 mF
Switching frequency	10 kHz
Gains: K1, K2, and K3	10, 70, 70

The objective of this work is to demonstrate the effectiveness of the SAPF-FCMLI controlled by a backstepping controller in terms of harmonic current filtering, reactive power compensation, and source current balancing under unbalanced nonlinear load conditions.

To validate its efficacy and robustness, comprehensive computer simulations were performed, including a significant load change introduced at 0.6 seconds. These simulations assessed the system's dynamic response, harmonic mitigation, and power factor improvement. A key aspect of the evaluation involved a direct comparison between the proposed backstepping controller and a conventional PI controller.

Initially, before SAPF-FCMLI activation (Fig. 4), source currents were heavily distorted with high Total Harmonic Distortion (THD) and were out of phase with the voltage, leading to a low power factor and high reactive power absorption. Upon activation, the SAPF-FCMLI, under both control strategies, dramatically enhanced power quality. Source currents became remarkably sinusoidal and perfectly synchronized with the voltage (Fig. 5 for backstepping, Fig. 6 for PI), indicating significantly reduced reactive power consumption and an excellent power factor.

Quantitatively, the backstepping controller consistently exceeded the PI controller in reducing THD. As detailed in Table II, the backstepping controller achieved a remarkable THD of 0.65% (pre-variation) and 1.02% (post-variation), which was significantly lower than the PI controller's 2.57% (pre-variation) and 2.31% (post-variation). The backstepping controller also maintained RMS currents closer to desired levels across both conditions, affirming its superior harmonic mitigation capabilities and robust control in dynamic scenarios.

Table. II
COMPARISON BETWEEN BACKSTEPPING CONTROLLER BC AND PI CONTROLLER IN TERMS OF SOURCE CURRENT

	PI		BC	
	t< 0.6s	t> 0.6s	t< 0.6s	t> 0.6s
THD (%)	2.57	2.31	0.65	1.02
RMS (A)	54.8	150.4	52.54	147.04

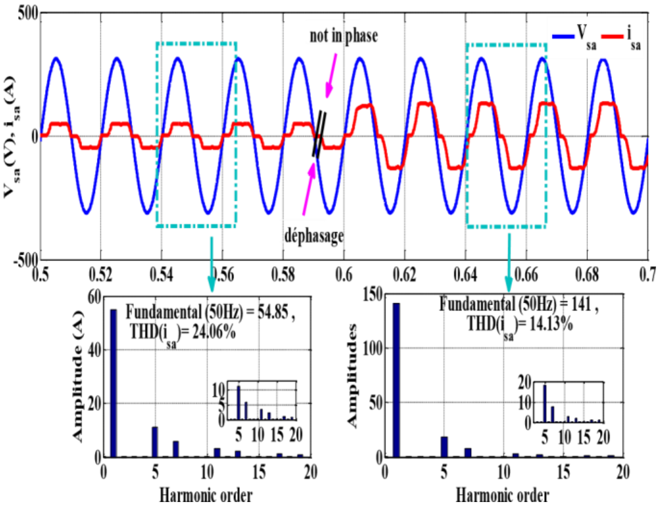

Fig. 4: Voltage and Source current (phase (a)) with THDs before SAPF-FCMLI insertion

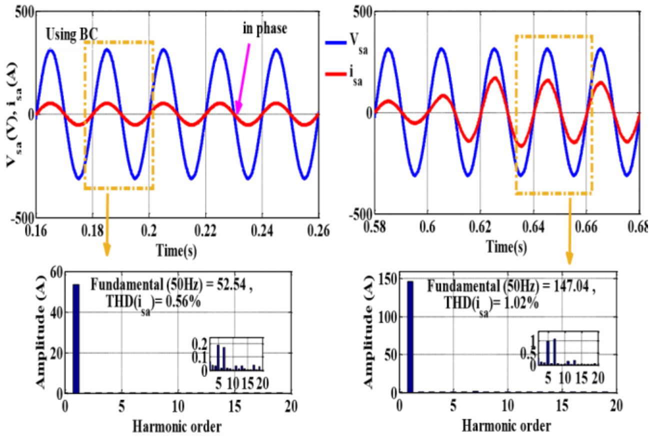

Fig. 5: Source voltage and current (phase (a)) waveforms with corresponding THDs after SAPF-FCMLI insertion using the backstepping controller.

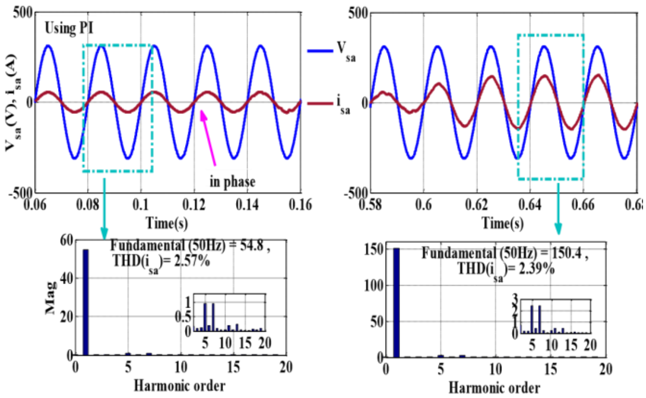

Fig. 6: Voltage and source current (phase (a)) with THDs after SAPFFCMLI insertion using PI controller.

The backstepping controller consistently demonstrates superior voltage regulation performance compared to the PI controller, especially under load disturbances. The DC bus voltage undershoot is a mere 27V with backstepping control, precisely half the 54V observed with PI control. Similarly, flying capacitor voltage (V_{Cj1}, VCj_2) undershoots are consistently half as low with Backstepping, as detailed in Table III.

Table. III

PERFORMANCE COMPARISON BETWEEN BACKSTEPPING CONTROLLER BC AND PI CONTROLLERS IN TERMS OF THE DC BUS VOLTAGE AND FLYING CAPACITOR VOLTAGES

Metric		PI	BC
Transit time		0.32 s	0.18 s
The undershoot in voltage	Vdc	54 V	27 V
	Vcj1	36 V	18 V
	Vcj2	18 V	9 V
Steady-State Error		higher	Significantly lower
Robustness		limited	Superior

Furthermore, the backstepping controller ensures a significantly faster transient response, taking just 0.18 seconds to restore voltages to their reference values, half the 0.32 seconds required by the PI controller. It also minimizes steady-state deviations and voltage ripples in the flying capacitors, crucial for maintaining high output waveform quality and overall system efficiency.

Figs. 7 and 8 visually confirm this stark contrast, with Figure 7 illustrating the backstepping controller's stable and excellent regulation, while Figure 8 highlights the larger fluctuations and slower recovery characteristic of PI control. This evidence collectively underscores the Backstepping controller's enhanced resilience and precision in maintaining critical voltage stability within the SAPF-FCMLI system.

V. CONCLUSION

This paper presented a backstepping control technique for a three-phase SAPF-FCMLI, achieving harmonic mitigation, reactive power compensation, and voltage balancing. Simulation results validate the controller's effectiveness, with THD reduced to 0.65%–1.02%, transient response time of 0.18 s, and near-zero steady-state error. Compared to the PI controller, backstepping offers faster response, lower oscillations, and better stability under nonlinear load variations. The approach enhances power quality, complies with IEEE standards, and improves grid efficiency. Future research could focus on real-time implementation, experimental validation, and integration with other advanced control techniques to further optimize performance.

REFERENCES

[1] E. Bouchaib, A. Moutabir, B. Bensassi, A. Ouchatti, Y. Zahraoui, and B. Benazza, *"Power Quality Improvement using a New DPC Switching Table for a Three-Phase SAPF", Int. J. Robot. Control Syst., vol. 3, no 3, p. 510-529, July. 2023. DOI: 10.31763/ijrcs.v3i3.1042.*

[2] X. Nie and J. Liu, *"Current Reference Control for Shunt Active Power Filters Under Unbalanced and Distorted Supply Voltage Conditions", IEEE Access, vol. 7, p. 177048-177055, 2019. DOI: 10.1109/ACCESS.2019.2957946.*

[3] C. Taghzaoui and al., *"Advanced Control of Single-Phase Shunt Active Power Filter Based on Flying Capacitor Multicell Converter", IFAC-Pap., vol. 55, no 12, p. 55-60, 2022. DOI: 10.1016/j.ifacol.2022.07.288.*

[4] A. Bouhafs, B. Rouabah, M. R. Kafi, and L. Louazene, *"Self-adaptive fault-tolerant control strategy of shunt active power filter based on multicellular converter", Diagnostyka, vol. 24, no 4, p. 1-10, Nov. 2023 DOI: 10.29354/diag/175006.*

[5] K. Djerboub, T. Allaoui, G. Champenois, M. Denai, and C. Habib, *"Particle Swarm Optimization Trained Artificial Neural Network to Control Shunt Active Power Filter Based on Multilevel Flying Capacitor Inverter", Eur. J. Electr. Eng., vol. 22, no 3, p. 199-207, June 2020. DOI: 10.18280/ejee.220301.*

[6] S. Othman, M. A. Alali, L. Sbita, J.-P. Barbot, and M. Ghanes, *"Modeling and Control Design Based on Petri Nets Tool for a Serial Three-Phase Five-Level Multicellular Inverter Used as a Shunt Active Power Filter", Energies, vol. 14, no 17, p. 5335, august 2021. DOI: 10.3390/en14175335.*

[7] B. Rouabah, H. Toubakh, and M. Sayed-Mouchaweh, *"Fault tolerant control of multicellular converter used in shunt active power filter", Electr. Power Syst. Res., vol. 188, p. 106533, Nov. 2020. DOI: 10.1016/j.epsr.2020.106533.*

[8] L. Manai, D. Hakiri, and M. Besbes, *"Performance Comparison Between Backstepping and P.I Regulators Methods for Four Level Flying Capacitor Inverter Based Active Power Filter Control", in 2020 4th International Conference on Advanced Systems and Emergent Technologies (IC_ASAND), Hammamand, Tunisia: IEEE, p. 400-405, dec. 2020. DOI: 10.1109/IC_ASAND49463.2020.9318314.*

[9] B. Rouabah, L. Rahmani, H. Toubakh, and E. Duviella, *"Adaptive and Exact Linearization Control of Multicellular Power Converter Based on Shunt Active Power Filter", J. Control Autom. Electr. Syst., vol. 30, no 6, p. 1019-1029, Dec. 2019. DOI: 10.1007/s40313-019-00510-w.*

[10] K. Antoniewicz and K. Rafal, *"Model predictive current control method for four-leg three-level converter operating as shunt active power filter and grid connected inverter", Bull. Pol. Acad. Sci. Tech. Sci., vol. 65, no 5, p. 601-607, oct. 2017. DOI: 10.1515/bpasts-2017-0065.*

[11] K. Hemici, M.O. Mahmoudi, and A. Yahdou, *"Super-twisting sliding mode control strategy applied to a three-phase shunt active filter based on flying capacitor multicellular inverter", Arch. Electr. Eng., vol. 74, n° 3, 2025. DOI: 10.24425/aee.2025.153913.*

[12] R. Premkumar, A. V. Juliet, L. Vijayaraja, *"Furtherance of Multilevel Inverter and Evolution of a Packed Inverter Unit for Dynamic Loads", Elektron. Ir Elektrotechnika, vol. 31, no 2, p. 4-14, Apr. 2025. DOI: 10.5755/j02.eie.40433.*

[13] Y. El Khlifi, A. El Magri, and R. Lajouad, *"A Lyapunov-Based Model Predictive Control Approach for Photovoltaic Microgrid Integration via Multilevel Flying Capacitor Inverter", E3S Web Conf., vol. 469, p. 00059, 2023. DOI: 10.1051/e3sconf/202346900059.*

[14] M. S. Badra, S. Barkat, and M. Bouzidi, *"Backstepping control of three-phase three-level four-leg shunt active power filter", J. Fundam. Appl. Sci., vol. 9, no 1, p. 274, Feb. 2017. DOI: 10.4314/jfas.v9i1.18.*

[15] T. Mahni, M. T. Benchouia, A. Ghamri, and A. Golea, *"Three-phase four-wire shunt active filter under unbalanced loads with backstepping*

and PI controllers", Aust. J. Electr. Electron. Eng., vol. 14, no 1-2, p. 41-47, Apr. 2017. DOI: 10.1080/1448837X.2018.1438035.

[16] P. Sarafrazi, S. Taher, and A. Akhavan, *"A Robust Backstepping Controller Based on Nonlinear Observer for Shunt Active Filters to Improve Power Quality in Four-Wire Distribution Systems", Jordan J. Electr. Eng., vol. 10, no 4, p. 1, 2024. DOI: 10.5455/jjee.204-1700421844.*

[17] H. Bey, F. Krim, and O. Gherouat, *"FPGA-Based Hardware in the Loop of Optimized Synergetic Controller for Active Power Filter", Int. Trans. Electr. Energy Syst., vol. 2023, p. 1-15, March 2023. DOI: 10.1155/2023/5810353.*

[18] J. A. Cortajarena, O. Barambones, P. Alkorta, and J. Cortajarena, *"Sliding mode control of an active power filter with photovoltaic maximum power tracking", Int. J. Electr. Power Energy Syst., vol. 110, p. 747-758, sept. 2019. DOI: 10.1016/j.ijepes.2019.03.070.*

[19] M. A. Mahboub, B. Rouabah, M. R. Kafi, and H. Toubakh, *"Health management using fault detection and fault tolerant control of multicellular converter applied in more electric aircraft system", Diagnostyka, vol. 23, no 2, p. 1-7, June 2022. DOI: 10.29354/diag/151039.*

[20] N. Madhuri and M. Surya Kalavathi, *"Fault-tolerant shunt active power filter with synchronous reference frame control and self-tuning filter", Meas. Sens., vol. 33, p. 101156, June 2024. DOI: 10.1016/j.measen.2024.101156.*

[21] J. Fei, H. Wang, and D. Cao, *"Adaptive Backstepping Fractional Fuzzy Sliding Mode Control of Active Power Filter", Appl. Sci., vol. 9, no 16, p. 3383, august 2019. DOI: 10.3390/app9163383.*

[22] A. M. Y. M. Ghias, J. Pou, M. Ciobotaru, and V. G. Agelidis, *"Voltage Balancing Method Using Phase-Shifted PWM for the Flying Capacitor Multilevel Converter", IEEE Trans. Power Electron., vol. 29, no 9, p. 4521-4531, sept. 2014. DOI: 10.1109/TPEL.2013.2285387.*

[23] G. Farivar, A. M. Y. M. Ghias, B. Hredzak, J. Pou, and V. G. Agelidis, *"Capacitor Voltages Measurement and Balancing in Flying Capacitor Multilevel Converters Utilizing a Single Voltage Sensor", IEEE Trans. Power Electron., vol. 32, no 10, p. 8115-8123, oct. 2017. DOI: 10.1109/TPEL.2016.2633278.*

Kheira Hemici received her Engineer and Magister degrees in Electrical Engineering from the University of Chlef, Algeria, in 2007 and 2011, respectively. She is currently pursuing a PhD in Automatic Control at National Polytechnic School of Algiers. In addition, she serves as an Assistant Master rank in the Department of Electrical Engineering of Hassiba Benbouali University (Algeria). Her research interests include power electronics, nonlinear and robust control, active power filters and power quality improvement.

Mohand Oulhadj Mahmoudi was born in Algiers (Algeria). He received the Engineer diploma, the Magister degree and the doctorate degree in Electrical Engineering from the National Polytechnic School of Algiers in 1982, 1986 and 1999 respectively. Since 1986, he holds teaching and research position at the Electrical Engineering department where he is currently professor. His areas of research interest are in Power Electronics, Electrical machines drives, advanced control techniques for power converters and renewable energy conversion.